2021

Studies of non-equilibrium behavior of quantum many-body systems using the adiabatic eigenstate deformations

BOSTON UNIVERSITY

GRADUATE SCHOOL OF ARTS AND SCIENCES

Dissertation

STUDIES OF NON-EQUILIBRIUM BEHAVIOR OF QUANTUM MANY-BODY SYSTEMS USING THE ADIABATIC EIGENSTATE DEFORMATIONS

by

MOHIT PANDEY

B.S.-M.S., IISER Kolkata, India 2015

Submitted in partial fulfillment of the

requirements for the degree of

Doctor of Philosophy

2021

Approved by

First Reader _____
David K. Campbell, PhD
Professor of Physics
Professor of Electrical and Computer Engineering
Professor of Materials Science and Engineering

Second Reader _____
Anatoli Polkovnikov, PhD
Professor of Physics
Professor of Materials Science and Engineering

I may not have gone where I intended to go, but I think I have ended up where I needed to be. -Douglas Adams

Physics is a subject of approximations, approximately. -Mohit Pandey

Acknowledgments

Usually, a PhD thesis's acknowledgements page is the only place where a reader gets a glimpse inside the lives of PhD candidates; they get to know about the people supporting and cheering the candidate in their PhD journey. If there were no such page, they might get away with an impression that PhD candidates accomplish their research on their own in vacuum. This is clearly not true. Like most human endeavors, progress in science is hard to achieve without supervision from advisors, collaboration from their peers and support of their friends and family members.

I would begin by acknowledging the support of my advisor Prof. David K Campbell who showed incessant faith in my abilities, was always available for helping me troubleshoot any obstacles that I faced, and gave me the freedom to find collaborators and pursue my independent research program. It is safe to say that I have had one of the best PhD advisors. I never, for once, had to second-guess if he is on my side, he always has been. Prof. Anatoli Polkovnikov, whose research on quantum-classical correspondence first brought my attention to Boston University while applying to graduate schools, has helped me grow as a physicist by challenging me to think deeply about my research; he always kept his door open for spontaneous discussions. Prof. Dries Sels, who is a professor at New York University and Flatiron Research Institute, has been an inspiring mentor, teacher and collaborator to me. Most of the central ideas of this thesis grew out of my conversations with him. He has a really strong communications skills with which he can talk about complex physics concepts to people having different background and levels of physics domain knowledge. When something wouldn't make sense to me, he would explain patiently to me in numerous ways till the central idea would stick to me; this rare skill of explaining a single concept in multiple ways he shares with one of my undergraduate college professors – Prof. Ananda Dasgupta – who taught me that physics is not just about deriving equations but the insight they bring. Without Dries, I would not have succeeded in

the one who impressed upon me about some of the core values that I follow in science such as it should be open and feel inclusive for everyone, and the importance of mentoring young scientists, writing regularly, work-life balance and unlearning the correlation between my work and my worth.

Gratefully,

Mohit

STUDIES OF NON-EQUILIBRIUM BEHAVIOR OF QUANTUM MANY-BODY SYSTEMS USING THE ADIABATIC EIGENSTATE DEFORMATIONS

MOHIT PANDEY

Boston University, Graduate School of Arts and Sciences, 2021

Major Professor: David K. Campbell, PhD
Professor of Physics
Professor of Electrical and Computer Engineering
Professor of Materials Science and Engineering

ABSTRACT

In the last few decades, the study of many-body quantum systems far from equilibrium has risen to prominence, with exciting developments on both experimental and theoretical physics fronts. In this dissertation, we will focus particularly on the adiabatic gauge potential (AGP), which is the generator of adiabatic deformations between quantum eigenstates and also related to "fidelity susceptibility", as our lens into the general phenomenon. In the first two projects, the AGP is studied in the context of counter-diabatic driving protocols which present a way of generating adiabatic dynamics at an arbitrary pace. This is quite useful as adiabatic evolution, which is a common strategy for manipulating quantum states, is inherently a slow process and is, therefore, susceptible to noise and decoherence from the environment. However, obtaining and implementing the AGP in many-body systems is a formidable task, requiring knowledge of the spectral properties of the instantaneous Hamiltonians and control of highly nonlocal multibody interactions. We show how an approximate gauge potential can be systematically built up as a series of nested com-

mutators, remaining well-defined in the thermodynamic limit. Furthermore, the resulting counter-diabatic driving protocols can be realized up to arbitrary order without leaving the available control space using tools from periodically-driven (Floquet) systems. In the first project, this driving protocol was successfully implemented on the electronic spin of a nitrogen vacancy in diamond as a proof of concept and in the second project, it was extended to many-body systems, where it was shown the resulting Floquet protocols significantly suppress dissipation and provide a drastic increase in fidelity. In the third project, the AGP is studied in the context of quantum chaos wherein it is found to be an extremely sensitive probe. We are able to detect transitions from non-ergodic to ergodic behavior at perturbation strengths orders of magnitude smaller than those required for standard measures. Using this alternative probe in two generic classes of spin chains, we show that the chaotic threshold decreases exponentially with system size and that one can immediately detect integrability-breaking (chaotic) perturbations by analyzing infinitesimal perturbations even at the integrable point. In some cases, small integrability-breaking is shown to lead to anomalously slow relaxation of the system, exponentially long in system size. This work paves the way for further studies in various areas such as quantum computation, quantum state preparation and quantum chaos.

Contents

List of Figures

List of Abbreviations

AGP	. . . .	Adiabatic gauge potential
CD	. . . .	Counter-diabatic
ETH	. . . .	Eigenstate thermalization hypothesis
eqn.	. . . .	equation
FE	. . . .	Floquet-engineered
FF	. . . .	Fast-forward
FPUT	. . . .	Fermi-Pasta-Ulam–Tsingou
Hz	. . . .	Hertz
NV	. . . .	Nitrogen-vacancy
RMT	. . . .	Random matrix theory
STA	. . . .	Shortcuts to adiabaticity
UA	. . . .	Unassisted

Chapter 1

Introduction

1.1 General statement

In the last few decades, the study of many-particle quantum systems far from equilibrium has risen to prominence, with exciting developments on both experimental and theoretical physics fronts. With the emergence of quantum simulators, such as ultracold atoms in optical lattices (Schäfer et al., 2020; Langen et al., 2015) and trapped atomic ions (Blatt and Roos, 2012), it is possible to experimentally study the coherent dynamics of quantum many-body systems for long times. These developments have stimulated considerable theoretical research (Eisert et al., 2015; Polkovnikov et al., 2010) including thermalization (or the lack thereof) in generic interacting systems (D'Alessio et al., 2016; Deutsch, 2018; Abanin and Papić, 2017; Abanin et al., 2019), and quantum information propagation (Lewis-Swan et al., 2019; Swingle, 2018).

Since it is impossible to study all potential non-equilibrium behaviors in any single thesis, we will focus particularly on the adiabatic gauge potential (AGP) (Kolodrubetz et al., 2017), which is also related to the "fidelity susceptibility", as our lens into the general phenomenon. The AGP is the generator of adiabatic deformations between quantum eigenstates. It also characterizes the distance between nearby eigenstates (also known as the Fubini-Study metric (Kolodrubetz et al., 2017; Page, 1987; Kobayashi and Nomizu, 1963; Provost and Vallee, 1980)). It has deep connections to surprising range of topics, including quantum state preparation (Torrontegui et al., 2013; Guéry-Odelin et al., 2019), quantum computing (Hartmann and Lechner, 2019; Takahashi, 2017), efficient heat engines (Vil-

lazon et al., 2019), quantum speed limits (Bukov et al., 2019), quantum chaos (Pandey et al., 2020; Villazon et al., 2020), and quantum computational complexity (Wurtz and Polkovnikov, 2020; Wurtz et al., 2020).

A partial explanation for why the AGP shows up in so many different contexts could be the ubiquitous nature of adiabatic processes in physics. For example, adiabatic processes occur in quantum annealing (Santoro and Tosatti, 2006; Santoro and Tosatti, 2008) in the transport of ultra-cold atoms (Krinner et al., 2014), in many-body state engineering (Bernien et al., 2017), and in quantum thermodynamics (Salamon et al., 2009; Rezek et al., 2009)). Also, adiabatic-related concepts are useful for model-building in theoretical physics (e.g. adiabatic continuity in Landau's Fermi-liquid theory).

1.2 Overview of the dissertation

This thesis is primarily composed of three papers (Boyers et al., 2019; Claeys et al., 2019; Pandey et al., 2020) studied in two different contexts – quantum state preparation and quantum chaos.

We start by introducing AGP in chapter II where we provide different derivations to emphasize its different defining characteristics and to present the historical development of the field.

In chapter III and IV, we study the AGP in the context of quantum state preparation. Conventionally, adiabatic processes are used for those quantum state preparation protocols which are inherently slow and therefore, susceptible to noise and decoherence from the environment. Alternatively, the AGP can be used to construct Hamiltonians that effectively speed up adiabatic evolutions; these are called "counter-diabatic (CD) Hamiltonians". However, the AGP is a highly non-local operator for complex systems which makes it experimentally infeasible to implement these CD Hamiltonians. Using tools of Floquet engineering, a non-local CD Hamiltonian can be mapped to local, periodically-

driven Hamiltonian. In chapter III, we implemented this driving protocol successfully on the electronic spin of a nitrogen vacancy in diamond as a proof of concept (Boyers et al., 2019). In chapter IV, we extended our periodic driving protocol to many-body systems (Claeys et al., 2019). Specifically, we first showed how an approximate gauge potential can be systematically built up as a series of nested commutators, remaining well-defined in the thermodynamic limit. In the second part of the chapter, we showed the resulting CD driving protocols can be realized up to arbitrary order without leaving the available control space using tools from periodically-driven (Floquet) systems.

In Chapter V, we study how the AGP norm can be used as an extremely sensitive probe of quantum chaos. Specifically, the norm of the AGP shows a remarkably different, and extremely sensitive, scaling with system size for integrable and chaotic systems: polynomial versus exponential. In two generic classes of spin chains, we found that the AGP can detect transitions from integrable to chaotic behavior at perturbation strengths orders of magnitude smaller than those required for standard measures like energy level statistics (Brody et al., 1981; Guhr et al., 1998; Mehta, 2004). Due to the AGP norm's exponential sensitivity, we found a novel regime in which the quantum system is chaotic but not ergodic, i.e. it shows exponential sensitivity to small perturbations but doesn't satisfy the eigenstate thermalization hypothesis. In a follow-up project (Villazon et al., 2020), this regime was also found in a central disordered spin chain.

In Chapter VI, we conclude with outlook for future.

Chapter 2

Introduction to Adiabatic Gauge Potential

2.1 Chapter overview

In this chapter, we present a selective historical review with the goal of introducing key ideas useful for later chapters. The idea of CD driving was first introduced independently by Demirplak and Rice in 2003 (Demirplak and Rice, 2003) and by Berry (which he called transitionless driving) in 2009 (Berry, 2009); later in 2013, Jarzynski proposed that CD driving "can be usefully framed in terms of a generator of adiabatic transport " (Jarzynski, 2013). These ideas were then synthesized in Kolodrubetz et al 's review (Kolodrubetz et al., 2017) where the the authors proposed to call the additional velocity-dependent term in CD driving the "adiabatic gauge potential" (AGP), drawing upon the similarity with gauge potentials that appear in electromagnetism.

Following this review, we present first Demirplak and Rice's derivation, wherein the AGP is introduced by performing a transformation to a moving frame defined by an instantaneous eigenbasis in which the Hamiltonian is diagonal. Secondly, we present Berry's derivation using a reverse-engineering technique starting from the standard adiabatic theorem's equation. Thirdly, we discuss Jarzynski's derivation, wherein the AGP is introduced as a generator of adiabatic transport. Finally, we introduce the expression for a "regularized AGP" in terms of long-time evolution of a local perturbation operator, which emphasizes that the AGP is in general highly non-local in operator space for generic complex systems.

For a more complete review of CD driving and other related ideas in the field, see the recent review on Shortcuts to Adiabaticity, cf. (Guéry-Odelin et al., 2019)

2.2 Derivations of the AGP

2.2.1 Demirplak and Rice's moving frame derivation

Let us consider a Hamiltonian H with an externally tuned parameter λ [1]. For a system of spins and particles in a box, the magnitude of the magnetic field and the volume, respectively, are examples of parameters λ. As we tune the parameter λ, the eigenstates and eigenvalues will vary. Specifically,

$$H(\lambda)|n(\lambda)\rangle = E_n(\lambda)|n(\lambda)\rangle, \tag{2.1}$$

where $|n(\lambda)\rangle$ is the eigenstate with corresponding eigenvalue E_n.

We introduce the AGP by doing a transformation to the moving frame characterized by the instantaneous energy basis. This is similar in spirit to the rotating frame transformation one employs for periodic time-dependent Hamiltonians. Just as the periodic Hamiltonian is static in rotating frame (Bukov et al., 2015), our time-dependent Hamiltonian is diagonal in the moving frame.

Specifically, let's go to the moving frame $|\tilde{\psi}\rangle = U^\dagger(\lambda(t))|\psi\rangle$, where U is the unitary operator that diagonalizes the Hamiltonian H. In this frame, the time evolution is given by:

$$i\hbar\partial_t|\tilde{\psi}\rangle = (\underbrace{U^\dagger H U}_{\text{diagonal}} - i\hbar\dot{\lambda}\underbrace{U^\dagger\partial_\lambda U}_{\text{off-diagonal}})|\tilde{\psi}\rangle$$

where the first and second terms are diagonal and non-diagonal, respectively, in the instantaneous eigenbasis. The second term is responsible for excitation between eigenstates depending upon how high the velocity $\dot{\lambda}$ is. Though Rice and Demirplak didn't use the term "AGP" in their paper, we recognize the second term as the AGP in the moving frame, i.e. $\tilde{A}_\lambda = i\hbar U^\dagger\partial_\lambda U$. From now on, we work in units with $\hbar = 1$ throughout this chapter.

---

[1]Note that we will be working with a single parameter λ, but our approach can be generalized easily for multiple parameters.

If we add the AGP term to the Hamiltonian H, then the new Hamiltonian will be diagonal in the moving frame; this leads to transitionless driving at an arbitrarily fast rate. Such a Hamiltonian is called the "CD Hamiltonian" [2], i.e., H_{CD} (Demirplak and Rice, 2003; Demirplak and Rice, 2005) $H_{CD} = H_0 + \dot{\lambda} A_\lambda$ where AGP in lab frame A_λ is:

$$A_\lambda = U \tilde{A}_\lambda U^\dagger = i \partial_\lambda \tag{2.2}$$

If we were interested in computing the matrix elements of the AGP in the energy eigenbasis, the above equation is not convenient to use, as we need to analytically compute derivatives of the eigenstates; we are interested in studying generic many-body systems whose spectra are not necessarily analytically known. With this goal in mind, we can derive an alternative expression of matrix elements of the AGP in the energy eigenbasis using the Hellman-Feynman theorem (Berry, 2009):

$$\langle m | A_\lambda | n \rangle = -i \frac{\langle m | \partial_\lambda H | n \rangle}{E_m - E_n}, m \neq n \tag{2.3}$$

For applying CD driving to many-body systems, we note that the eqn. (2.3) already highlights an important issue: since the gauge potential is defined in the eigenbasis of the instantaneous Hamiltonian, it requires exact diagonalization. Furthermore, for increasing system sizes, it is clear that the denominator can become exponentially small, which can lead to divergent matrix elements and as a result, gauge potential can be ill-defined in the thermodynamic limit. We will later show how to regularize the AGP to deal with this issue.

Using eqn (2.3), we can derive another equivalent expression of AGP (Jarzynski, 2013; Kolodrubetz et al., 2017):

$$[H, \partial_\lambda H + [H, A_\lambda]] = 0 \tag{2.4}$$

As the name suggests, the AGP has a gauge freedom which corresponds to the gauge free-

---

[2]Our notation differs from Rice and Demirplak who called the additional term in the Hamiltonian as the CD Hamiltonian

dom in choosing the phases of eigenstates. In the martix form of the AGP (eqn. (2.3)) , this corresponds to choosing the diagonal elements while in the operator form (eqn. (2.4)), it corresponds to the gauge transformation $A_\lambda \to A_\lambda + f$, where f is any function such that $[f, H] = 0$.

2.2.2 Berry's reverse engineering derivation

The derivation of Demirplak and Rice is quite general, depending upon the unitary transformation chosen. In discussing that derivation, we had chosen instantaneous energy eigenbasis in which Hamiltonian is diagonal, but we could derive a gauge potential for any unitary transformation. As a result, we didn't pay much attention to the adiabaticity of the wavefunction explicitly. In Berry's derivation, we correct that perspective by starting from the standard equation for the wavefunction that satisfies the adiabatic approximation and then finding the additional term in Hamiltonian (which is the AGP) that ensures the whole Hamiltonian satisfies Schrödinger equation with the adiabatic wavefunction, no matter how fast the quantum state is driven.

Setting the stage As mentioned in the previous section, let's suppose the parameter $\lambda(t)$ is changed from one value to another. We are working in the basis of instantaneous eigenstates. The Hamiltonian in this basis will be diagonal, i.e. $H_0 = \sum_n \varepsilon_n |n\rangle\langle n|$, where both eigenstates and eigenvalues will vary through parameter λ. The wavefunction will satisfy a time-dependent Schrödinger equation given by:

$$i\dot{\lambda}\frac{d}{d\lambda}|\psi(\lambda(t))\rangle = H_0(\lambda(t))|\psi(\lambda(t))\rangle \tag{2.5}$$

where time has been parametrized through $\lambda(t)$. We are interested in the dynamics when the parameter is changed slow enough [3]. Under adiabatic conditions, we can derive that the

---

[3]The adiabatic approximation is valid when rate of change of energy levels is smaller than energy gap, i.e. $\dot{\lambda}|\langle m(t)|\partial_\lambda|n(t)\rangle| \ll \omega_{mn}$. Recently it was shown that this simple quantitative condition can lead to inconsistency in certain cases and is not sufficient to ensure adiabaticity (Marzlin and Sanders, 2004; Tong

wavefunction is given as $|\psi_{ad}(\lambda(t))\rangle = \sum_n c_n e^{i\gamma_n}|n\rangle$ where c_n are characterized by initial wavefunction and γ_n is:

$$\gamma_n = -\int\limits_{\lambda(0)}^{\lambda(t)} \frac{d\lambda}{\dot{\lambda}}\varepsilon(\lambda) + i\int\limits_{\lambda(0)}^{\lambda(t)} d\lambda\langle n|\partial_\lambda n\rangle, \tag{2.6}$$

where the first term corresponds to dynamical phase and the second corresponds to geometrical/Berry phase [4].

Reverse engineering   To achieve transitionless quantum driving, Berry proposed that we can add a velocity dependent term in the Hamiltonian $\dot{\lambda}A_\lambda$ so that even though wavefunction is not adiabatic for the total Hamiltonian $H_0 + \dot{\lambda}A_\lambda$, it is adiabatic for the original Hamiltonian H_0 for all times (and not just at the end-point). In this spirit, we solve for the expression of $\dot{\lambda}A_\lambda$ which satisfies the following equation:

$$i\dot{\lambda}\frac{d}{d\lambda}|\psi_{ad}(\lambda(t))\rangle = (H_0 + \dot{\lambda}A_\lambda)|\psi_{ad}(\lambda(t))\rangle \tag{2.7}$$

After plugging the expression of adiabatic wavefunction (eqn. (2.6)) to Schrödinger equation, we get:

$$A_\lambda = i\sum_n |\partial_\lambda n(\lambda)\rangle\langle n(\lambda)| - \langle n(\lambda)|\partial_\lambda n(\lambda)\rangle|n(\lambda)\rangle\langle n(\lambda)| \tag{2.8}$$

where the sum is over n eigenstates [5].

Alternatively, one could derive the AGP for a different choice of phases of the eigenstates that corresponds to the expression in the previous subsection (Berry, 2009; Tor-

---

et al., 2005). However, despite the new additional conditions proposed in (Tong et al., 2007), it doesn't take away the fact that adiabatic conditions are slow processes.

[4]Note that $\langle n|\partial_\lambda n\rangle$ is a purely imaginary number. Otherwise, the norm of the wavefunction would not be preserved (Griffiths and Schroeter, 2018).

[5]Quantum transitionless driving for all states might not be relevant for some experiments. Instead one might be interested in avoiding a mixture of certain eigenstate, while letting other eigenstates mix among themselves. To take a concrete example of a three-level system, let's suppose we are interested in preserving the groundstate but letting the other two levels mix. In that case, instead of having to sum over all eigenstates, we would have just one term in the AGP, i.e. $A_\lambda^{GS} = i\partial_\lambda|GS(\lambda)\rangle\langle GS(\lambda)|$.

rontegui et al., 2013). If we choose eigenstates as $|\tilde{n}\rangle = e^{-\int d\lambda \langle n|\partial_\lambda n\rangle}|n\rangle$, then we can write adiabatic wavefunction as $|\tilde{\psi}_{ad}(t)\rangle = \sum_{\tilde{n}} c_{\tilde{n}} e^{-i\int_0^t dt' \varepsilon_{\tilde{n}}(t')}|\tilde{n}\rangle$. Starting with $|\tilde{\psi}_{ad}(t)\rangle$ and plugging it into (2.7), then the AGP will be:

$$\tilde{A}_\lambda = i\sum_{\tilde{n}}|\partial_\lambda \tilde{n}\rangle\langle \tilde{n}| = i\partial_\lambda \qquad (2.9)$$

where sum over all the eigenstates was done to get the second equality.

The two expressions of the AGP differ in their particular gauge chosen which corresponds to the gauge freedom we have in choosing phase of the eigenstates: the AGP in eqn. (2.8) has all of its diagonal elements to be zero while the later one in eqn. (2.9) has non-zero diagonal elements.

2.2.3 Jarzynski's generator of adiabatic transport derivation

In his 2013 paper (Jarzynski, 2013), Jarzynski showed that the AGP is the generator of the adiabatic transformations. Apart from providing a powerful geometrical interpretation of the AGP, his proposal helped formulate a classical analogue of transitionless driving which was missing in the previous two derivations we discussed.

In particular, Jarzynski showed that the AGP associates infinitesimal displacements in parameter space, $\lambda \to \lambda + \delta\lambda$ with displacements in Hilbert space $|\psi\rangle \to |\psi\rangle + |\delta\psi\rangle$ according to the following rule:

$$i|\delta\psi\rangle = \delta\lambda A_\lambda |\psi\rangle \qquad (2.10)$$

where we chose A_λ to be given by (2.8) which corresponds to a particular gauge choice. Hence, for an eigenstate $|n\rangle$ that is being displaced infinitesimally to $|n\rangle + |\delta n\rangle$, we have up to first order in $\delta\lambda$:

$$|n\rangle \to |n\rangle + |\delta n\rangle = (1 - i\delta\lambda A_\lambda)|n\rangle = e^{i\phi_n \delta\lambda}|n(\lambda + \delta\lambda)\rangle \qquad (2.11)$$

where $\phi_n = i\langle n|\partial_\lambda n\rangle$. If we start in an eigenstate $|n(\lambda_0)\rangle$ and repeatedly apply eq. (2.11) along a curve λ_s, starting from λ_0 and ending at λ_f, then the eigenstate is transported along the curve $\exp(i\int d\lambda \phi_n(\lambda))|n(\lambda_f)\rangle$. Mathematically, we have

$$\lim_{N\to\infty}\prod_{i=1}^{N}e^{-iA_\lambda\delta\lambda_i}|n(\lambda_0)\rangle = \exp(i\int_{\lambda_0}^{\lambda_f}d\lambda\phi_n(\lambda))|n(\lambda_f)\rangle, \tag{2.12}$$

where $\delta\lambda_i = (\lambda_f - \lambda_0)/N$. Thus, we see that the AGP escorts the system along the eigenstates of the Hamiltonian as the parameter λ is varied.

Two-level system example Let's consider a two-level Hamiltonian in which we rotate the spinor in x-z plane:

$$H = \cos\theta\sigma_z + \sin\theta\sigma_x. \tag{2.13}$$

It's easy to diagonalize the Hamiltonian and show that eigenvalues are $\varepsilon_\pm = \pm 1$ and eigenvectors are:

$$|e\rangle = \cos(\theta/2)|+\rangle + \sin(\theta/2)|-\rangle, \quad |g\rangle = -\sin(\theta/2)|+\rangle + \cos(\theta/2)|-\rangle, \tag{2.14}$$

where

$$|+\rangle = \begin{bmatrix}1\\0\end{bmatrix}, \quad |-\rangle = \begin{bmatrix}0\\1\end{bmatrix}. \tag{2.15}$$

We see that for $\theta = 0$, eigenvectors point in z-direction and for $\theta = \pi/2$, eigenvectors point in x-direction. Hence, as we tune θ from 0 to $\pi/2$, the eigenvectors rotate in x-z plane.

For this Hamiltonian, we can show that AGP $A_\theta = \frac{1}{2}\sigma_y$. Now let us verify eq. (2.11) by showing the effect of AGP acting on $|e(\theta)\rangle$ under infinitesimal rotation. In the first order

of $\delta\theta$, we have:

$$e^{-iA_\theta\delta\theta}|e(\theta)\rangle \;=\; e^{-i\sigma_y\delta\theta/2}|e(\theta)\rangle \tag{2.16}$$

$$=\; (1-i\sigma_y\delta\theta/2)|e(\theta)\rangle \tag{2.17}$$

$$=\; (1-i\sigma_y\delta\theta/2)[\cos(\theta/2)|+\rangle+\sin(\theta/2)|-\rangle] \tag{2.18}$$

$$=\; |e(\theta)\rangle+\delta\theta/2[\cos(\theta/2)|-\rangle-\sin(\theta/2)|+\rangle] \tag{2.19}$$

$$=\; |e(\theta)\rangle+\delta\theta\partial_\theta|e(\theta)\rangle \tag{2.20}$$

$$=\; |e(\theta+\delta\theta)\rangle. \tag{2.21}$$

In comparison to eqn. (2.11), here the phase factor of $e^{-\langle e|\partial_\theta e\rangle\delta\theta}$ is 1 as $\langle e|\partial_\theta e\rangle=0$. Now we can repeatedly apply this equation to get:

$$\lim_{N\to\infty}\prod_{i=1}^{N}e^{-iA_\theta\delta\theta_i}|e(\theta=0)\rangle = |e(\theta=\pi/2)\rangle \tag{2.22}$$

where $\delta\theta_i=\frac{\pi}{2N}$.

Thus, we see that the AGP A_θ escorts the system along the eigenstates of the Hamiltonian as the parameter θ is varied.

Equivalently, it can be shown that the AGP satisfies the following equation (Jarzynski, 2013):

$$-i[H,A_\lambda] \;=\; \partial_\lambda H-\text{diag}\left(\partial_\lambda H\right) \tag{2.23}$$

$$\langle n|A_\lambda|n\rangle \;=\; 0 \tag{2.24}$$

where the first equation is general while the second equation is a particular gauge choice in which diagonal elements of the AGP are chosen to be zero. With this gauge choice, it is easy to show (2.24) is equivalent to Berry's expression (2.8) using the identity eqn. (2.3).

2.2.4 Regularized AGP

Derivation

Let's re-write the AGP matrix elements in the energy eigenbasis:

$$\langle m|A_\lambda|n\rangle = -i\frac{\langle m|\partial_\lambda H|n\rangle}{E_m - E_n} \tag{2.25}$$

For a many-body Hamiltonian, the number of states in Hilbert space grows exponentially in system size, while the energy bandwidth grows linearly with system size. Thus, distance between any two nearby eigenvalues is exponentially small in system size, i.e., $\min(E_m - E_n) \sim e^{-S}$, where S is entropy and $S \sim \kappa L$ where κ is entropy density. If there are non-zero off-diagonal elements of $\langle m|\partial_\lambda H|n\rangle$, then the AGP is ill-defined. This is known as "the small denominator problem" (Kolodrubetz et al., 2017).

To resolve this problem, we introduce a small energy cutoff μ that regularizes our AGP:

$$\langle m|A_\lambda|n\rangle = -i\lim_{\mu\to 0}\frac{\langle m|\partial_\lambda H|n\rangle}{\omega_{mn}^2 + \mu^2}\omega_{mn} \tag{2.26}$$

where $\omega_{mn} = E_m - E_n$. This has a clear physical intuition: instead of considering transitions (matrix elements) between individual eigenstates, we now only consider transitions between energy shells of width μ. For eigenstates with $\omega_{mn} \gg \mu$, this reproduces the exact AGP, whereas in the limit $\omega_{mn} \ll \mu$, the AGP no longer diverges but reduces to a constant.

Using the Laplace transform, it can be shown that (Claeys et al., 2019; Jarzynski, 1995):

$$A_\lambda = -i\lim_{\mu\to 0}\int_0^\infty e^{-\mu t}[\partial_\lambda H(t) - \partial_\lambda H(-t)]dt \tag{2.27}$$

where $\partial_\lambda H(t) = \bar{U}^\dagger \partial_\lambda H \bar{U}$ and $\bar{U} = e^{-iHt}$ is the propagator in artificial time as we evolve $\partial_\lambda H$ while keeping λ fixed. Notably, Jarzynski in 1995 (Jarzynski, 1995) derived the above equation that solves (2.24), albeit for classical equations. Also, we note that the inverse of μ limits the growth $\partial_\lambda H(t)$ in operator space. In the chapter V, we will show that when μ is

appropriately chosen, the AGP is an extremely sensitive probe of quantum chaos.

Using Baker-Campbell-Hausdorff formula to express $\partial_\lambda H(t)$ in terms of commutators and then integrating out time, we get:

$$A_\lambda = \lim_{\mu \to 0} \frac{-i}{\mu} \sum_{n=0}^{\infty} (-1)^n \frac{C^{(2n+1)}}{\mu^{2n+1}} \tag{2.28}$$

where $C^{(n)}$ is n-commutator of H and $\partial_\lambda H$, i.e. $C^{(n)} = [H, [H, \text{ n times} \ldots, [H, \partial_\lambda H]]]]$. We define the first term as $C^{(1)} = [H, \partial_\lambda H]$, second term as $C^{(2)} = [H, [H, \partial_\lambda H]] = [H, C^{(1)}]$ and so on and forth.

The expression (2.28) is useful as it gives a powerful way to find the AGP in terms of operators, and it can be easily generalized to the classical world by replacing commutators with Poisson brackets. However, for complex systems, performing the summation over the various commutator terms is a challenging task – in contrast to simple systems in which commutator series is algebraically closed, each term in commutator series for complex systems keeps spitting out new non-local operators which might lead to divergences. This will be illustrated by taking a couple of examples in the following subsection.

Applications

We present a couple of examples to illustrate the usefulness of expressing the AGP in terms of commutators (eqn. (2.28)).

The AGP for a two-level system Let's consider a two-level quantum system, or qubit, which is modeled using Landau-Zener Hamiltonian:

$$H = \Delta \sigma_z + \lambda(t) \sigma_x \tag{2.29}$$

where the $\sigma_{x,y,z}$ are Pauli matrices. To determine the AGP using (2.28), let's compute the commutators:

$$C^{(1)} = 2i\Delta\sigma^y \tag{2.30}$$

$$C^{(2)} = -4\Delta(-\Delta\sigma^x + \lambda\sigma^z) \tag{2.31}$$

$$C^{(3)} = \alpha^2 C^{(1)} \tag{2.32}$$

where $\alpha^2 = 4(\Delta^2 + \lambda^2)$. Hence, we get:

$$\begin{aligned}
A_\lambda &= \lim_{\mu \to 0} \frac{-i}{\mu\alpha} C^{(1)} \sum_{n=0}^{\infty} (-1)^n \left(\frac{\alpha}{\mu}\right)^{2n+1} \\
&= \lim_{\mu \to 0} \frac{-i}{\mu^2 + \alpha^2} C^{(1)} \\
&= \frac{1}{2} \frac{\Delta}{\Delta^2 + \lambda^2} \sigma_y
\end{aligned}$$

We see that this is an example in which the algebra closes, as $C^{(3)}$ gives an operator proportional to $C^{(1)}$. This makes it easy to compute AGP in this case. Also, it makes sense that AGP is proportional to σ_y as that is the generator of rotation in x-z plain.

The AGP for a four-body system This is a slightly more complex problem than the previous two-level system that we considered. Here we see that the $C^{(3)}$ is composed of two additional operators (a two-body T_2 and a three-body T_3 operator) apart from $C^{(1)}$. When we track the higher-order commutators of T_2 and T_3, we find that all higher-order commutators that contribute to AGP are a mixture of these three operators $-C^{(1)}, T_2, T_3$.

$$H = -J \sum_{j=-1}^{2} \sigma_j^x \sigma_{j+1}^x - \lambda(\sigma_0^z + \sigma_1^z) \tag{2.33}$$

$$C^{(1)} = -2iJ\sigma_0^y(\sigma_{-1}^x + \sigma_1^x) - 2iJ\sigma_1^y(\sigma_0^x + \sigma_2^x)$$

$$C^{(2)} = -8J^2(\sigma_1^x\sigma_{-1}^x + 1)\sigma_0^z + 4J\lambda\sigma_0^x(\sigma_{-1}^x + \sigma_1^x)$$

$$- 8J^2(\sigma_0^x\,\sigma_2^x + 1)\sigma_1^z + 4J\lambda\sigma_1^x(\sigma_0^x + \sigma_2^x) - 8J\lambda\sigma_1^y\sigma_0^y$$

$$C^{(3)} = \alpha^2 C^{(1)} + T_2 + T_3$$

where two body operator $T_2 = -24iJ\lambda^2(\sigma_0^y\sigma_1^x + \sigma_1^y\sigma_0^x)$, the three body operator $T_3 = 32iJ^2\lambda(\sigma_{-1}^x\sigma_0^z\sigma_1^y + \sigma_0^y\sigma_1^z\sigma_2^x)$, $C_{T_2}^{(2)} = [H,[H,T_2]]$ and $C_{T_3}^{(2)} = [H,[H,T_3]]$.

On further computation, we find that:

$$C_{T_2}^{(2)} = \delta_1 C^{(1)} + \delta_2 T_2 + \delta_3 T_3 \tag{2.34}$$

$$C_{T_3}^{(2)} = \varepsilon_1 C^{(1)} + \varepsilon_2 T_2 + \varepsilon_3 T_3 \tag{2.35}$$

where $\delta_1 = 96J^2\lambda^2$, $\delta_2 = 16\lambda^2$, $\delta_3 = 9\lambda^2$, $\varepsilon_1 = 64J\lambda^3$, $\varepsilon_2 = \frac{32}{3}J\lambda$ and $\varepsilon_3 = \alpha^2$.

Let us summarize here in a more meaningful way what we have so far:

$$C^{(3)} = \alpha^2 C^{(1)} + T_2 + T_3$$

$$C_{T_2}^{(2)} = \delta_1 C^{(1)} + \delta_2 T_2 + \delta_3 T_3 \tag{2.36}$$

$$C_{T_3}^{(2)} = \varepsilon_1 C^{(1)} + \varepsilon_2 T_2 + \varepsilon_3 T_3$$

We can use the above information to write three coupled homogeneous recurrence equations, which are linear in $C^{(2n+1)}$, $C_{T_2}^{(2n)}$ and $C_{T_3}^{(2n)}$:

$$\boxed{\begin{aligned} C^{(2n+1)} &= \alpha^2 C^{(2n-1)} + C_{T_2}^{(2n-2)} + C_{T_3}^{(2n-2)} \\ C_{T_2}^{(2n)} &= \delta_1 C^{(2n-1)} + \delta_2 C_{T_2}^{(2n-2)} + \delta_3 C_{T_3}^{(2n-2)} \\ C_{T_3}^{(2n)} &= \varepsilon_1 C^{(2n-1)} + \varepsilon_2 C_{T_2}^{(2n-2)} + \varepsilon_3 C_{T_3}^{(2n-2)} \end{aligned}} \tag{2.37}$$

The advantage is that these equations have constant coefficients. Let's formulate this in matrix form:

$$
\begin{bmatrix} C^{(2n+1)} \\ C_{T_2}^{(2n)} \\ C_{T_3}^{(2n)} \end{bmatrix} = \begin{bmatrix} \alpha^2 & 1 & 1 \\ \delta_1 & \delta_2 & \delta_3 \\ \varepsilon_1 & \varepsilon_2 & \varepsilon_3 \end{bmatrix} \begin{bmatrix} C^{(2n-1)} \\ C_{T_2}^{(2n-2)} \\ C_{T_3}^{(2n-2)} \end{bmatrix} \tag{2.38}
$$

Hence, we can write $v_n = T^n v_0$ where

$$
v_n = \begin{bmatrix} C^{(2n+1)} \\ C_{T_2}^{(2n)} \\ C_{T_3}^{(2n)} \end{bmatrix}, T = \begin{bmatrix} \alpha^2 & 1 & 1 \\ \delta_1 & \delta_2 & \delta_3 \\ \varepsilon_1 & \varepsilon_2 & \varepsilon_3 \end{bmatrix}, v_0 = \begin{bmatrix} C^{(1)} \\ T_2 \\ T_3 \end{bmatrix} \tag{2.39}
$$

where $C_{T_2}^{(0)} = T_2$ and $C_{T_3}^{(0)} = T_3$.

We note that $T^n = (PDP^{-1})^n = PD^nP^{-1}$, where D is diagonal matrix and P is the similarity transformation that diagonalizes T. Finally, we can write $v_n = PD^nP^{-1}v_0$

What we are actually interested in is adiabatic gauge potential for which we need to sum over n-Commutators $C^{(2n+1)}$

$$
\begin{aligned}
A_\lambda &= \lim_{\mu \to 0} \frac{-i}{\mu} \sum_{n=0}^{\infty} (-1)^n \frac{C^{(2n+1)}}{\mu^{2n+1}} \\
&= \lim_{\mu \to 0} \frac{-1}{\mu} \sum_{n=0}^{\infty} C^{(2n+1)} \frac{i^{2n+1}}{\mu^{2n+1}} \\
&= \lim_{\mu \to 0} \frac{-1}{\mu} G\left(z = \frac{i}{\mu}\right)
\end{aligned}
$$

where $G(z) = \sum_{n=0}^{\infty} C^{(2n+1)} z^{2n+1}$ is the generating function (Wilf, 2005).

We find that:

$$
\lim_{\mu \to 0} \frac{-1}{\mu} G\left(z = \frac{i}{\mu}\right) = \alpha^* a_1 + \beta^* b_0 + \delta^* c_0 \tag{2.40}
$$

where

$$\begin{aligned}
\alpha^* &= -i\frac{(\delta_2\varepsilon_3 - \delta_3\varepsilon_2)}{\det T} \\
\beta^* &= -i\frac{(\varepsilon_2 - \varepsilon_3)}{\det T} \\
\delta^* &= -i\frac{(\delta_3 - \delta_2)}{\det T}
\end{aligned} \tag{2.41}$$

where

$$\det T = \delta_3\left(\varepsilon_1 - \alpha^2\varepsilon_2\right) + \delta_2\left(\alpha^2\varepsilon_3 - \varepsilon_1\right) + \delta_1\left(\varepsilon_2 - \varepsilon_3\right) \tag{2.42}$$

More details are given in A.

For more complex problems (e.g., the non-integrable spin chain) which I am not presenting here, every higher-order commutator produces a new operator that didn't appear in previous commutator. This can be understood through the operator spreading eqn. (5.11) where local perturbation operator $\partial_\lambda H$ gets highly non-local as it evolves in time through the higher-order commutators that shows up in $\partial_\lambda H(t)$.

2.3   Summary

In this chapter, we presented four derivations of the AGP with a goals of emphasizing the different defining characteristics of the AGP and presenting a (selective) historical development of the field. Firstly, Rice and Demirplak's derivation was presented, which is quite general for any unitary transformation; though gauge potentials can be defined for any unitary transformation, this thesis is interested in the adiabatic transformation. Secondly, Berry's derivation was presented, which is quite explicit about adiabaticity of the wavefunction as it starts from the standard adiabatic approximation equation. Thirdly, Jarzynski gave a powerful geometrical intuition to think about AGP in terms of generating adiabatic transport in Hilbert state space, which opened the door to generalize AGP for classical systems. At the end, the fourth derivation of the regularized AGP showed how the AGP for many-body systems needs a regularizer and how it leads to the AGP being expressed in

terms of operator spreading which helped us understand that the AGP is a highly non-local operator for generic complex systems. Also, we presented here some unpublished calculations that showed how computing the AGP through commutator expansion for generic complex systems is a daunting challenge.

Chapter 3

Floquet-engineered Quantum State Manipulation in a Noisy Qubit

This chapter was published in Physical Review A (Boyers et al., 2019).

3.1 Introduction

Accurate manipulation of quantum systems is a fundamental goal in many areas of quantum science, ranging from quantum information science through quantum simulation to quantum sensing. Control over the quantum state of a system is crucial as a preparatory step for a subsequent computation or simulation (Bloch et al., 2008), or as a goal in itself, as in adiabatic quantum computation (Farhi et al., 2000; Albash and Lidar, 2018). Some quantum states are "easy" to prepare, for example, by cooling the system to the ground state of its Hamiltonian. However, a number of applications require access to quantum states that are "difficult" to prepare with high fidelity. For example, quantum annealing (Santoro and Tosatti, 2006; Santoro and Tosatti, 2008) requires finding the quantum ground state of a complex many-body Hamiltonian, and entanglement-assisted quantum sensing requires preparation of entangled states of large numbers of qubits in order to achieve sensitivity beyond the standard quantum limit (Jones et al., 2009). One of the standard approaches to state preparation is to use adiabatic evolution: initialize the system in an eigenstate of a simple, easy to prepare Hamiltonian and then adiabatically change the Hamiltonian to a new one with one of the eigenstates (typically the ground state) being the desired target state. This approach has been used for transport of ultra-cold atoms (Krinner et al.,

2014), many-body state engineering (Bernien et al., 2017), and quantum thermodynamics (Salamon et al., 2009; Rezek et al., 2009).

Adiabatic evolution is a generic strategy, but the evolution rate must be much smaller than the energy gaps in the system. Therefore, this approach is slow and susceptible to decoherence due to inevitable interactions with the environment (Huang et al., 2011). Shortcuts to adiabaticity are methods of achieving faster adiabatic evolution, in order to maintain high fidelity in the presence of decoherence and noise. One technique is counter-diabatic (also known as transitionless) driving (Berry, 2009; Demirplak and Rice, 2003; Demirplak and Rice, 2005; Bason et al., 2012; Zhang et al., 2013). In this approach, transitionless evolution at arbitrary velocities is achieved by adding additional velocity-dependent counter terms to the Hamiltonian. However, for complex quantum many-body systems, these additional counter terms are, in general, highly non-local operators and, as a result, typically experimentally inaccessible. A related technique involves fast-forward driving protocols, which use only operators available in the original Hamiltonian but employ more complex time dependence to achieve high fidelity (Masuda and Nakamura, 2009). Two main strategies have been proposed for finding fast-forward protocols. The first uses methods from optimal control theory to analytically or numerically find driving protocols that achieve near-unit fidelity (Judson and Rabitz, 1992; Caneva et al., 2011; Glaser et al., 1998; Hegerfeldt, 2013; Farhi et al., 2014). Although successful in many cases, such protocols are hard to compute for generic quantum systems (Day et al., 2019). The second strategy is based on a recently-proven statement that any fast-forward drive can be obtained as a unitary transformation of a counter-diabatic drive (Bukov et al., 2019; Petiziol et al., 2018). In this approach, the problem of finding a fast-forward protocol can be decomposed into finding a counter-diabatic protocol first, and then finding the time-dependent unitary transformation that converts the counter-diabatic Hamiltonian into the original one, with modified time-dependent couplings. However, once again, there is no general method for

finding this transformation for many-body systems.

Here we use Floquet engineering to construct an approximate fast-forward protocol from a counter-diabatic protocol. By driving the system at high frequency we introduce a time-scale separation between the periodic modulation and the change of the protocol control fields. This separation allows us to construct the aforementioned transformation and results in protocols that become asymptotically exact in the limit of infinite frequency. This Floquet-engineered fast-forward driving can achieve nearly unit fidelity with a target state for short protocol duration and protects the quantum system against decoherence, as illustrated in fig. 3·1. In this work we apply this approach to a qubit, but the methodology can be generalized to more complex quantum systems by including higher harmonics of the fundamental Floquet frequency (see appendix B.1). To demonstrate the feasibility of the suggested approach, we experimentally implemented the Floquet-engineered protocol in a single qubit based on a nitrogen-vacancy (NV) center in diamond and compared its performance with the conventional fast-forward protocol in presence of external noise.

3.2 Model

Consider a two-level quantum system, or qubit, with the following Hamiltonian

$$H(t) = \Delta \sigma_z + \lambda(t) \sigma_x \tag{3.1}$$

where the $\sigma_{x,y,z}$ are Pauli matrices, and we work in units with $\hbar = 1$ throughout the paper, i.e. energies are measured in Hz. For a spin-1/2 system, Δ is proportional to the magnitude of the static magnetic field in the z-direction, and $\lambda(t)$ is proportional to the magnitude of the time-dependent magnetic field in x-direction, serving as the external control parameter. The initial state $|\psi_0\rangle = |-x\rangle$ and the target state $|\psi_t\rangle = |x\rangle$ are eigenstates of σ_x, see fig. 3·1(a). The fidelity of the protocol is defined as the overlap of the final spin state $|\psi(t)\rangle$ with the target state: $F(t) = |\langle \psi(t)|\psi_t\rangle|^2$. The initial and target states are adiabatically
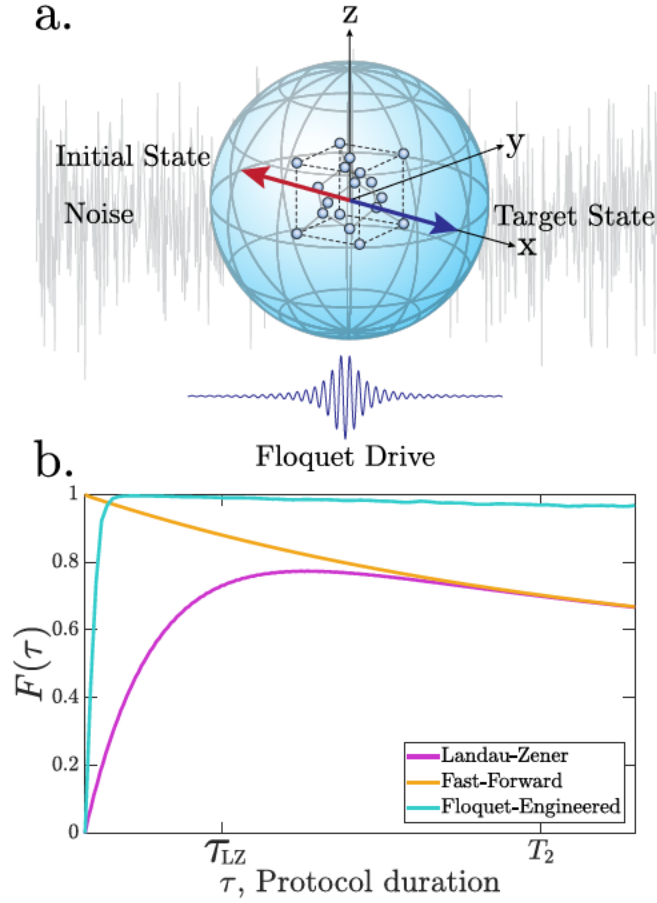
Figure 3·1: (a) Schematic for quantum state manipulation of a qubit implemented with the electronic spin of a nitrogen-vacancy center in diamond. Our protocol includes a high-frequency Floquet drive that allows faster transitionless evolution, and maintains robust performance in presence of external noise. (b) Numerical calculation of the fidelity for preparing final state $|\psi_f\rangle$ for varying protocol duration, in presence of decoherence. A linear Landau-Zener ramp (purple) has poor fidelity at short times due to transitions and at long times due to decoherence. A fast-forward drive (orange) removes Landau-Zener transitions, but is still susceptible to decoherence at long protocol durations. A Floquet-engineered fast-forward drive (blue) suppresses Landau-Zener transitions and decouples the system from decoherence, resulting in high fidelity over a broad range of protocol durations. Ticks on the x-axis indicate the minimum time to achieve adiabatic evolution according to the Landau-Zener condition: $\tau_{\mathrm{LZ}} = \lambda/\Delta^2$, and the spin coherence time T_2.

connected but separated by an avoided crossing at $\lambda = 0$. For an adiabatic protocol the relative change of the instantaneous gap has to be much smaller than the gap: $\dot{\lambda}/\Delta \ll \Delta$. This puts a strong constraint on the minimal required time to implement an adiabatic linear sweep protocol: $\tau \gg \lambda/\Delta^2$. If this time is comparable to, or longer than the decoherence time of the qubit, the adiabatic protocol never achieves high fidelity, as in fig. 3·1 (b).

A counter-diabatic protocol introduces an additional control field that keeps the system in the instantaneous ground state (Berry, 2009; Kolodrubetz et al., 2017):

$$H_{\text{CD}}(t) = \Delta\sigma_z + \lambda(t)\sigma_x + \frac{1}{2}\frac{\Delta\dot{\lambda}}{\Delta^2 + \lambda^2}\sigma_y. \tag{3.2}$$

For a qubit, the σ_y control, corresponding to a time-dependent magnetic field in y-direction for a spin-1/2, is as easy to implement as σ_x. However, for generic many-body systems the counter-diabatic Hamiltonian would require access to a large number of multi-qubit operators, that, in general, are experimentally inaccessible. Fast-forward protocols avoid this complication (Bukov et al., 2019; Masuda and Nakamura, 2009) by performing a virtual rotation around the x-axis, producing a control Hamiltonian that involves only the control fields B_z, B_x corresponding to the original operators σ_z, σ_x:

$$H_{\text{FF}} = B_z(t)\sigma_z + B_x(t)\sigma_x \tag{3.3}$$
$$= \Delta\sqrt{1 + \left(\dot{\lambda}\Gamma\right)^2}\sigma_z + \left(\lambda + \frac{1}{2}\frac{d(\arctan\dot{\lambda}\Gamma)}{dt}\right)\sigma_x,$$

where $\Gamma^{-1} = 2(\lambda^2 + \Delta^2)$. While this transformation is easy to construct for a qubit, it is a formidable task to find it in many-body systems (Bukov et al., 2019).

Our approach to constructing the fast-forward Hamiltonian exploits the idea of Floquet engineering as a way of implementing the unavailable counter-diabatic term by using

control fields with both smoothly-varying and rapidly-oscillating components:

$$H_{\text{FE}} = \Delta \left(1 - \frac{\mathcal{J}_0(2\Omega)}{2\mathcal{J}_1(2\Omega)} \frac{\dot{\lambda}\cos\omega t}{(\Delta\mathcal{J}_0(2\Omega))^2 + \lambda^2} \right) \sigma_z$$
$$+ (\lambda(t) + \omega\Omega\sin\omega t)\,\sigma_x, \tag{3.4}$$

where $\omega \gg \Delta$ is the drive frequency, $\mathcal{J}_0$ and $\mathcal{J}_1$ are zero and first-order Bessel functions, and Ω is a free parameter of the drive. By building in a large separation in the time-scales representing the period of the drive and the protocol time, the time-evolution of the system within each drive period can be described with an effective Floquet Hamiltonian, which can be computed systematically using the Magnus expansion (Bukov et al., 2015; Eckardt, 2017). The desired fast forward protocol is then obtained by matching the effective Floquet Hamiltonian with the counter-diabatic Hamiltonian (see appendix B.1). For a given protocol duration, larger drive frequency results in higher protocol fidelity, as shown in fig. 3·2.
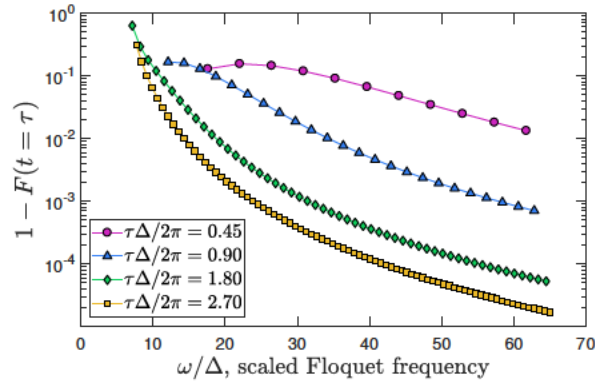
Figure 3·2: Simulation of Floquet-engineered protocol fidelity Numerically calculated scaling of the infidelity, $1 - F$, of the Floquet-engineered protocol of duration τ with the drive frequency ω for a cubic sweep $\lambda(t) = \lambda_0(4(t/\tau)^3 - 6(t/\tau)^2 + 1)$. Points are stroboscopically sampled such that $\omega\tau = n\pi$. Protocol parameters: $\lambda_0/2\pi = 1.5\,\text{MHz}, \Delta/2\pi = 0.1/\mathcal{J}_0(2\Omega)$ MHz, $\Omega = \pi$.

3.3 Experiment

We experimentally implemented the Floquet-engineered fast forward protocol in a qubit formed by the electronic spin of a nitrogen-vacancy (NV) center in diamond. The spin state of the negatively-charged NV center has a long coherence time, even at room temperature, and its electronic level structure allows robust spin polarization, manipulation, and readout (Taylor et al., 2008; Childress et al., 2014). In order to avoid hyperfine effects due to the nitrogen nuclear spin, the experiment was operated at the magnetic field corresponding to the NV excited state level anti-crossing, where optically pumping the NV center polarizes both the NV electron and nuclear spin (Jacques et al., 2009) (see appendix B.2). We manipulated the NV center spin by radio-frequency fields with carrier frequency ω_0 near its $|m_s = 0\rangle \leftrightarrow |m_s = +1\rangle$ transition, thus implementing the effective Hamiltonian in eq. (3.1) in the frame rotating at this frequency. The gap Δ was controlled by detuning ω_0 from the spin transition frequency, and the parameter λ corresponds to the amplitude of the driving field, which is swept as a function of time.

We performed quantum state manipulation protocols using the pulse sequence in fig. 3·3 (a). We initialized the NV spin into the $|-x\rangle$ eigenstate with a laser pulse followed by a $\pi/2$ pulse around the y-axis. The spin then evolved under the corresponding protocol Hamiltonian, and its final spin state $|\psi\rangle$ was detected by applying another $\pi/2$ pulse around the y-axis, followed by a measurement of spin-dependent fluorescence. To track the evolution of the system throughout the protocol, we switched off the control fields after a variable time t, halting state evolution.

To characterize the performance of our scheme, we carried out the linear Landau-Zener sweep of $\lambda(t)/2\pi$ in the range $\pm 1.5\,\mathrm{MHz}$ over time $\tau = 6\mu s$ at a fixed gap $\Delta/2\pi = 0.1\,\mathrm{MHz}$. The data points, together with a simulation, are shown in fig. 3·3. As a second benchmark, we measured the performance of the conventional fast-forward protocol by implementing the B_z and B_x control parameter sweeps given in eq. (3.3). The values of the gap and the
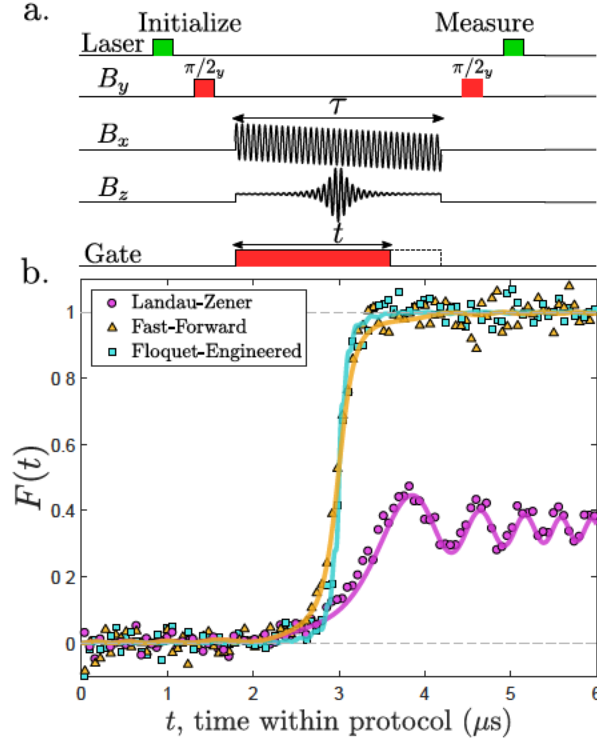
Figure 3·3: Comparison of state preparation protocols a. The experimental pulse sequence implementing the Floquet-engineered fast forward protocol. The qubit was manipulated using control fields B_x, B_y, B_z; initialization and readout was performed using laser pulses. The gate pulse was used to switch off the control fields, halting qubit state evolution after a variable protocol duration time t. b. Measurements of fidelity during each protocol for the linear Landau-Zener sweep (purple circles), the fast-forward protocol (yellow triangles), and the Floquet-engineered protocol (blue squares). Solid lines are simulations of corresponding protocol. Oscillations in the protocols, most pronounced in Landau-Zener, are due to transitions caused by the discontinuous first derivative at the start and end of the sweep and slight misalignment of the initial state (see appendix B.2). Protocol parameters: $\lambda(t) = \lambda_0(1 - 2t/\tau)$, $\Delta/2\pi = 0.1\,\mathrm{MHz}$, $\lambda_0/2\pi = 1.5\,\mathrm{MHz}$, $\omega/2\pi = 6\,\mathrm{MHz}$, $\Omega = \pi/4$ and $\tau = 6\,\mu\mathrm{s}$.

linear sweep of $\lambda(t)$ were the same as for the Landau-Zener protocol. The experimentally-measured fidelity shown in fig. 3·3 shows a dramatic improvement over the Landau-Zener protocol and approaches the value 0.990 ± 0.005 as the entire protocol is completed.

We then implemented the Floquet-engineered protocol with the time-dependence given in eq. (3.4), again using the same values of the parameters. Measurements of the Floquet-

engineered protocol fidelity, shown in fig. 3·3, demonstrate that its performance closely approximates that of the conventional fast-forward protocol and its fidelity approaches 0.994 ± 0.004 as the protocol is completed.
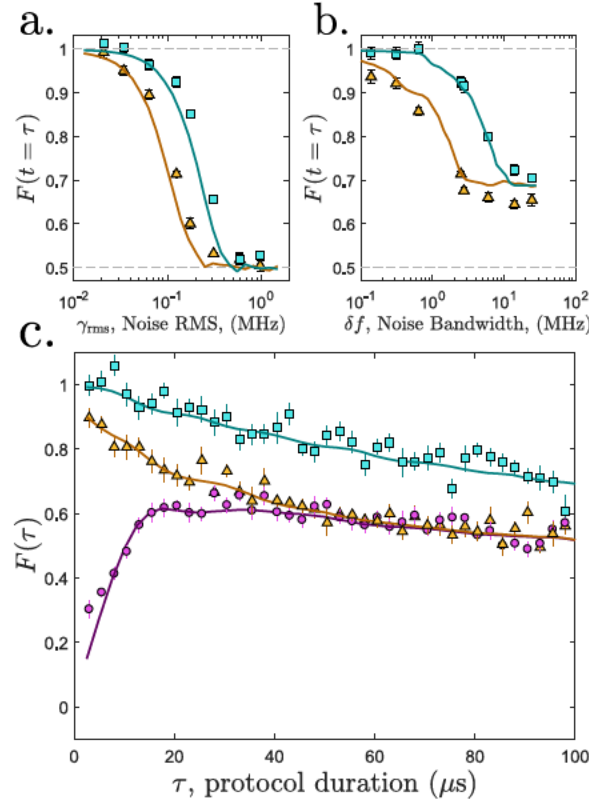
Figure 3·4: State preparation in presence of noise a. Measurements of final fidelity as a function of noise magnitude for Floquet-engineered protocol (blue squares) and conventional fast-forward protocol (yellow triangles). Noise magnitude was expressed as root-mean-square amplitude γ_{rms} at a fixed noise bandwidth of 2.5 MHz. b. Measurements of final fidelity as a function of noise bandwidth for Floquet-engineered protocol (blue squares) and conventional fast-forward protocol (yellow triangles). Noise spectral density was fixed at $0.079\ \text{MHz}/\sqrt{\text{MHz}}$. c. Final fidelity as a function of protocol duration with noise bandwidth 640 kHz and noise root-mean-square amplitude 64 kHz. In all figures, solid lines are numerical simulations. Protocol parameters are the same as in fig. 3. Error bars may be obscured by data markers.

Fidelity is an important benchmark that quantifies the performance of a protocol, but to assess its potential in real-world applications it is important to study its performance

in presence of the inevitable coupling to a noisy environment. We introduced such an interaction in our experiments by coupling the NV spin to a source of magnetic noise with controlled amplitude γ_{rms} and spectral bandwidth δf (see appendix B.2). This noise adds a stochastic term $\gamma(t)\sigma_z$ to the Hamiltonians in (3.1), (3.3), and (3.4), which induces transitions between the initial and final qubit states. Measurements of the fidelity of the fast-forward and the Floquet-engineered protocols in the presence of this noise are shown in fig. 3·4. The Floquet-engineered fast forward protocol is more robust to the environmental decoherence: it maintains its high-fidelity performance up to factor of 3 larger noise amplitude and factor of 5 greater noise bandwidth than the conventional fast-forward protocol with the same parameters. This can be understood by noting that the Floquet-engineered fast forward protocol performs counter-diabatic driving in the frame rotating at the Floquet frequency ω. Since in this frame the noise spectrum is shifted away from zero frequency, it can efficiently induce qubit transitions within a protocol of duration τ only if it has spectral overlap with the qubit. That is, the spectral bandwidth of the noise is $\delta f \gtrsim \omega - \lambda_0/(\tau\Delta)$, where the qubit spectral bandwidth is approximately $\lambda_0/(\tau\Delta)$. This sets the noise bandwidth of approximately $5\,\text{MHz}$ at which the fidelity starts to drop, as seen in fig. 3·4 (b). This mechanism of protecting a qubit against environmental noise is similar to the methods of dynamical decoupling (Viola et al., 1999; de Lange et al., 2010) and further simulations demonstrating this effect can be found in Appendix B.5. This argument breaks down if the noise amplitude is comparable to, or larger than, the magnitude of the σ_z term in the corresponding Hamiltonian since the noise can no longer be treated perturbatively.

3.4   Conclusion

Our approach demonstrates a new tool for high-fidelity quantum state manipulation in presence of environmental decoherence. The method based on Floquet engineering has the potential to be directly generalizable to high-fidelity state preparation in complex many-

body quantum systems, where the counter-diabatic and the fast-forward protocols are much harder to realize. Additional promise is demonstrated by the robustness of our scheme to external noise. Our Floquet-engineering approach may find applications in a broad range of fields that rely on high-fidelity preparation of quantum states of noisy or open quantum systems, such as adiabatic quantum computing, quantum simulation, and quantum sensing beyond the standard quantum limit with entangled and squeezed states (Albash and Lidar, 2018; Pichler et al., 2018).

In the late stages of our work we became aware of Ref. (Petiziol et al., 2018) where a similar theoretical strategy of designing fast-forward protocols is proposed.

Chapter 4

Floquet-engineering Counterdiabatic Protocols in Quantum Many-body Systems

This chapter was published in Physical Review Letters as one of the Editors' Suggestions (Claeys et al., 2019).

4.1   Introduction

Adiabaticity presents one of the fundamental tools in physics, ranging from heat engines in thermodynamics to quantum state preparation and computation (Nielsen and Chuang, 2000; Chandra et al., 2010; Vinjanampathy and Anders, 2016; Bohn et al., 2017). However, true adiabatic control can only be obtained using slow driving and asymptotically long time scales. While faster driving leads to diabatic excitations and resulting dissipative losses, the inevitable presence of decoherence and noise in realistic quantum systems limits the available timescales, preventing true adiabaticity. Various methods have been proposed in order to achieve so-called "Shortcuts to Adiabaticity" both theoretically (Chen et al., 2010; del Campo, 2013; Torrontegui et al., 2013; del Campo and Kim, 2019) and experimentally (Couvert et al., 2008; Bowler et al., 2012; Walther et al., 2012; Bason et al., 2012; An et al., 2016; Du et al., 2016; Zhou et al., 2017; Zhang et al., 2013; Kölbl et al., 2019), mimicking adiabatic dynamics without requiring slow driving.

One way of circumventing this loss of fidelity at finite driving rates is through counterdiabatic (CD) or transitionless driving – a velocity-dependent term is added to the control Hamiltonian, exactly compensating the diabatic contributions to the Hamiltonian in

the moving frame (Demirplak and Rice, 2003; Demirplak and Rice, 2005; Berry, 2009; Kolodrubetz et al., 2017). This term is known as the *adiabatic gauge potential* (or gauge connection), encoding the geometry of eigenstates (Kolodrubetz et al., 2017). However, while this potential may be exactly obtained in few-body systems, its construction in general requires diagonalization of the Hamiltonian in the full Hilbert space, prohibiting its use in general many-body systems. Furthermore, the resulting operator tends to involve highly nontrivial and nonlocal couplings not present in the control Hamiltonian, preventing its actual implementation (Zwick et al., 2014; Saberi et al., 2014; Hatomura and Mori, 2018). While various applications of STA in many-body systems have been investigated, these generally impose restrictions on the studied system (for a recent review, see (Guéry-Odelin et al., 2019))– either dynamic symmetries or scaling laws (Deffner et al., 2014; Diao et al., 2018), Born-Oppenheimer dynamics (Duncan and del Campo, 2018), underlying Lax pairs (Okuyama and Takahashi, 2016). Various effors have also been made to use STA to counteract the Kibble-Zurek mechanism in critical systems (del Campo et al., 2012; del Campo and Sengupta, 2015).

Restricting driving to available (local) couplings led to the development of fast-forward (FF) protocols (Masuda and Nakamura, 2009; Torrontegui et al., 2012; Patra and Jarzynski, 2017; Bukov et al., 2019), which only follow the adiabatic path at the beginning and end of the driving. However, there exists no general way of constructing these for complex systems. One specific class of FF protocols is those where CD driving is realized through Floquet-engineering: high-frequency oscillations are added to the control so that the resulting Floquet Hamiltonian mimics the CD Hamiltonian. In few-body systems, this has already been used for high-fidelity quantum state manipulation both theoretically in closed (Ribeiro et al., 2017; Petiziol et al., 2018; Petiziol et al., 2019) and open systems (Villazon et al., 2019), and experimentally in a noisy qubit (Boyers et al., 2019).

Here, we propose a method of (i) finding an efficient and controlled approximation to

the gauge potential, remaining well-defined in many-body systems, which can then (ii) be systematically realized through Floquet-engineering by resonantly oscillating the instantaneous Hamiltonian with the driving term. Effectively, we propose a general strategy for designing fast adiabatic protocols, applicable both in small quantum systems to achieve high fidelity for state preparation and in large systems, quantum or classical, to suppress dissipative losses. This is illustrated on few- and many-body systems.

4.2   Methods

Consider a control Hamiltonian $\mathcal{H}(\lambda)$ dependent on a control parameter λ. Our goal is to transport a stationary state or distribution, at an initial value of the control parameter λ_i, to one corresponding to a final value λ_f. In the standard approach, this is done by adiabatically changing $\lambda(t)$ from λ_i to λ_f, which is often impractical because of the necessary access to long timescales. The key idea of CD driving is to vary the parameter $\lambda(t)$ at a finite rate while simultaneously compensating the diabatic excitations by explicitly adding an auxiliary term as

$$\mathcal{H}_{CD}(t) = \mathcal{H}(\lambda) + \dot{\lambda}\mathcal{A}_\lambda. \tag{4.1}$$

Adiabatic control at arbitrary driving rates and for arbitrary initial states is realized provided the adiabatic gauge potential $\mathcal{A}_\lambda$ (Kolodrubetz et al., 2017) satisfies

$$\langle m|\mathcal{A}_\lambda|n\rangle = i\langle m|\partial_\lambda n\rangle = -i\frac{\langle m|\partial_\lambda\mathcal{H}|n\rangle}{\varepsilon_m - \varepsilon_n}, \tag{4.2}$$

where $|n\rangle$ and ε_n are the eigenstates and the energy spectrum of the instantaneous Hamiltonian, $\mathcal{H}(\lambda)|n\rangle = \varepsilon_n|n\rangle$. The CD term then exactly compensates non-adiabatic transitions between eigenstates.

   The expression (4.2) already highlights the issues with many-body CD driving: since the gauge potential is defined in the eigenbasis of the instantaneous Hamiltonian, it requires exact diagonalization. Furthermore, for increasing system sizes the denominator $(\varepsilon_m - \varepsilon_n)$

can become exponentially small, leading to divergent matrix elements and an ill-defined gauge potential in the thermodynamic limit (Jarzynski, 1995; Kolodrubetz et al., 2017). Physically, at least in chaotic systems, the exact gauge potential also cannot be local because no local operator is expected to be able to distinguish general many-body states with arbitrary small energy difference (D'Alessio et al., 2016). Considering a system with a gapped ground state, using Lieb-Robinson bounds a quasi-local operator can be obtained reproducing the action of the exact gauge potential on this ground state, since no divergences occur in this case (Bachmann et al., 2017).

In the following, we propose an approximate gauge potential defined as

$$\mathcal{A}_\lambda^{(\ell)} = i \sum_{k=1}^{\ell} \alpha_k \underbrace{[\mathcal{H}, [\mathcal{H}, \dots [\mathcal{H}, \partial_\lambda \mathcal{H}]]]}_{2k-1}, \tag{4.3}$$

fully determined by a set of coefficients $\{\alpha_1, \alpha_2, \dots, \alpha_\ell\}$, where ℓ determines the order of the expansion. The exact gauge potential can be represented in this form in the limit $\ell \to \infty$ (see Appendix C). Instead we consider a small finite value of ℓ and treat the expansion coefficients as variational parameters, which can be obtained by minimizing the action S_ℓ

$$S_\ell = \text{Tr}\left[G_\ell^2\right], \qquad G_\ell = \partial_\lambda \mathcal{H} - i[\mathcal{H}, \mathcal{A}_\lambda^{(\ell)}]. \tag{4.4}$$

The exact gauge potential is known to follow from the variational minimization of an action (Sels and Polkovnikov, 2017). However, it is not a priori clear what (local) operators should be included in the variational basis. The total number of possible operators increases exponentially with their support, limiting the brute-force minimization to highly local operators with restricted support. Furthermore, it is far from guaranteed that such operators will be experimentally realizable. The main finding of the present work is that the proposed ansatz tackles both problems simultaneously. (i) The number of variational coefficients can be kept small while still returning an accurate approximation to the exact gauge potential. As such, Eq. (4.3) can be seen as a variational ansatz including only the most important contri-

butions with the maximum range of operators set by ℓ. (ii) In addition, this gauge potential can be engineered with a simple Floquet protocol. This realization is possible because the high-frequency expansion of the Floquet Hamiltonian shares the commutator structure of Eq. (4.3). This expansion exhibits the symmetries of the exact solution, and as additional bonus we remark that this ansatz has a well-defined classical limit, where even the local-operator basis becomes infinite-dimensional. In classical systems, the commutators in Eq. (4.3) only need to be replaced by Poisson brackets.

Since the action is simply the Hilbert-Schmidt norm of G_ℓ, this method has the clear advantage that the action can be calculated without explicitly constructing the operator matrix in the full Hilbert space. There are various ways of motivating Eq. (4.3) (see Appendix C including Refs. (D'Alessio and Rigol, 2014; Abanin et al., 2015; Kuwahara et al., 2016; Mori et al., 2016).): it can be seen as an expansion in the Krylov subspace generated by the action of G_ℓ, or by noting that such commutators appear through the Baker-Campbell-Hausdorff expansion in the definition of a (properly regularized) gauge potential, or by noting that its matrix elements share the general structure of those of the exact gauge potential. Namely, evaluating Eq. (4.3) in the eigenbasis of $\mathcal{H}$ returns

$$
\begin{aligned}
\langle m|\mathcal{A}_\lambda^{(\ell)}|n\rangle &= i\sum_{k=1}^{\ell}\alpha_k\langle m|\underbrace{[\mathcal{H},[\mathcal{H},\dots[\mathcal{H},\partial_\lambda\mathcal{H}]]]}_{2k-1}|n\rangle \\
&= i\left[\sum_{k=1}^{\ell}\alpha_k(\varepsilon_m-\varepsilon_n)^{2k-1}\right]\langle m|\partial_\lambda\mathcal{H}|n\rangle.
\end{aligned}
\tag{4.5}
$$

This can be compared to the exact expression (4.2), containing a state-dependent factor $\langle m|\partial_\lambda\mathcal{H}|n\rangle$ and a prefactor only dependent on the excitation frequency $\omega_{mn}=(\varepsilon_m-\varepsilon_n)$. The variational optimization can then be seen as approximating the exact prefactor $1/\omega_{mn}$ by a power-series prefactor $a_\lambda^{(\ell)}(\omega_{mn})\equiv\sum_{k=1}^{\ell}\alpha_k\omega_{mn}^{2k-1}$ for the range of relevant excitation frequencies set by $\langle m|\partial_\lambda\mathcal{H}|n\rangle$.

While such an approximation is generally impossible due to the divergence of $1/\omega_{mn}$

near $\omega_{mn} = 0$ and the divergence of the power series for $\omega_{mn} \to \infty$, the approximation does not need to hold in these limits. First, for large ω_{mn} the matrix elements of local operators $\langle m|\partial_\lambda \mathcal{H}|n\rangle$ typically decay exponentially with ω_{mn} (D'Alessio et al., 2016), leading to a negligible contribution to the gauge potential. Second, there are physical motivations for allowing transitions for small ω_{mn}. When speeding up adiabatic driving in the presence of an energy gap Δ, only transitions with $\omega_{mn} \geq \Delta$ need to be suppressed in order to achieve unit fidelity, and in more general gapless regimes corresponding to e.g. excited states the resulting excitations will be confined to a narrow energy shell, the width of which decreases with the order ℓ of the expansion.
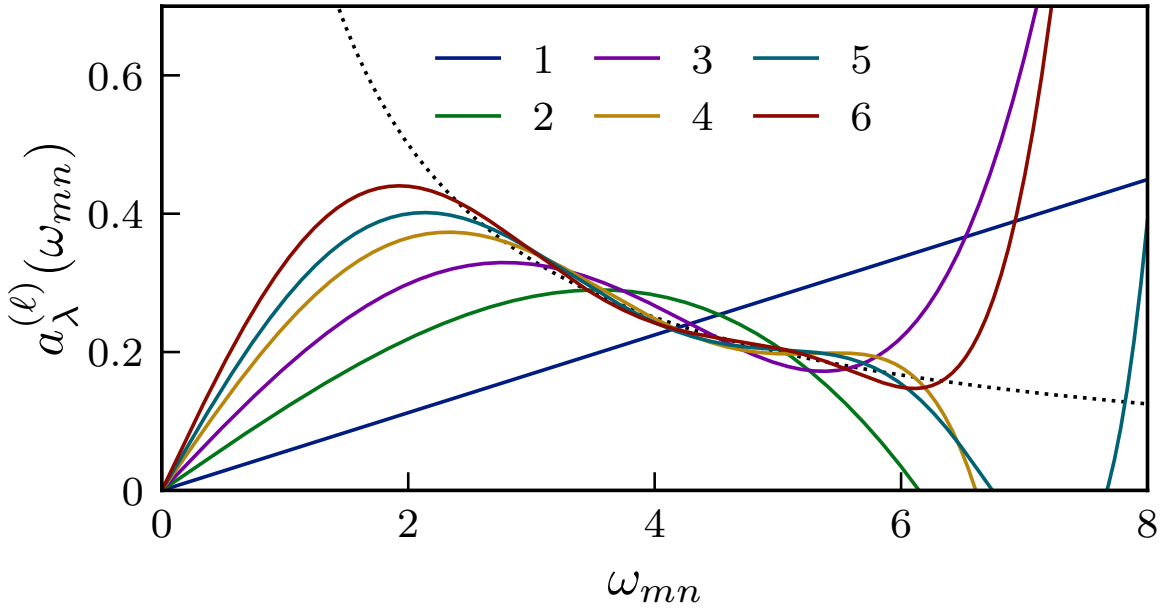
Figure 4·1: Variationally-obtained power-series prefactor $a_\lambda^{(\ell)}(\omega_{mn})$ for Eq. (4.6). Dotted line corresponds to exact prefactor $1/\omega_{mn}$. Parameters $L = 14, J = 1, h_x = h_z = 0.3, \lambda = 1$.

We illustrate how this expansion works in Fig. 4·1, for a non-integrable Ising chain with

$$\mathcal{H} = J \sum_{i=1}^{L} \sigma_i^z \sigma_{i+1}^z + \lambda \left(h_z \sum_{i=1}^{L} \sigma_i^z + h_x \sum_{i=1}^{L} \sigma_i^x \right), \tag{4.6}$$

where no exact gauge potential can be obtained in the thermodynamic limit. It is clear that

the variational optimization returns a gauge potential optimized for a relevant window of excitation frequencies, where the approximation necessarily improves with increasing ℓ.

The resulting gauge potential can immediately be used to reliably speed up adiabatic protocols taking $\mathcal{H}_{CD}^{(\ell)}(t) = \mathcal{H}(\lambda) + \dot{\lambda}\mathcal{A}_{\lambda}^{(\ell)}(\lambda)$. While this presents a guaranteed improvement in fidelity, it also requires access to interaction terms not necessarily available within the protocol, where the only interactions that are generally present are those of $\mathcal{H}(\lambda)$ and $\partial_\lambda\mathcal{H}(\lambda)$. Remarkably, this CD Hamiltonian can be realized as an effective Floquet Hamiltonian by simply oscillating these two terms at high frequency. Consider

$$
\begin{aligned}
\mathcal{H}_{FE}(t) = {} & \left[1 + \frac{\omega}{\omega_0}\cos(\omega t)\right]\mathcal{H}(\lambda) \\
& + \dot{\lambda}\left[\sum_{k=1}^{\infty}\beta_k\sin\left((2k-1)\omega t\right)\right]\partial_\lambda\mathcal{H}(\lambda),
\end{aligned}
\tag{4.7}
$$

with β_k the Fourier coefficients of the additional drive and ω_0 a reference frequency typically set by the excitation energy of the system, both of which will be determined later. Floquet theory allows for the definition of a time-independent Floquet Hamiltonian reproducing time evolution over a single driving cycle (with $T = 2\pi/\omega$)

$$
\exp\left(-i\mathcal{H}_F T\right) \equiv \mathcal{T}\exp\left(-i\int_{t}^{t+T}\mathcal{H}_{FE}(t')\,dt'\right).
\tag{4.8}
$$

The limit where the driving term scales with the frequency is known to give rise to non-trivial Floquet Hamiltonians $\mathcal{H}_F$ in various scenarios (Goldman and Dalibard, 2014; Goldman et al., 2015; Bukov et al., 2015; Mentink, 2017; Claassen et al., 2017).

More specifically, the proposed series expansion for the adiabatic gauge potential can be implemented in the infinite-frequency limit $\omega \to \infty$, realizing (stroboscopic) CD driving. This Floquet Hamiltonian can be obtained from the Magnus expansion, presenting a series expansion of $\mathcal{H}_F$ in powers of the inverse-frequency. Essentially, the $\omega \to \infty$ limit combined with the scaling of $\mathcal{H}$ with ω guarantees that only commutators of the

form $[\mathcal{H},\dots,[\mathcal{H},\partial_\lambda\mathcal{H}]]]$ survive in the Magnus expansion, which can then be found as $\mathcal{H}_F = \mathcal{H}(\lambda) + \dot{\lambda}\mathcal{A}_F$ (see Appendix C), with

$$\langle m|\mathcal{A}_F|n\rangle = i\sum_{k=1}^{\infty}\beta_k\mathcal{J}_{2k-1}\left(\frac{\omega_{mn}}{\omega_0}\right)\langle m|\partial_\lambda\mathcal{H}|n\rangle\,, \qquad (4.9)$$

where $\mathcal{J}_k$ are Bessel functions of the first kind. Again, this reproduces the correct structure of the gauge potential, where the frequency-dependent prefactor is now expressed in terms of $\mathcal{J}_k$. For small ω_{mn}/ω_0, $\mathcal{J}_k(\omega_{mn}/\omega_0) \propto \omega_{mn}^k$, which can be used to stroboscopically engineer the CD term by choosing the Fourier harmonics in such a way that the Floquet prefactor reproduces the power series (4.5) in the relevant range of excitation frequencies. In first approximation, this can be done by restricting time-evolution to ℓ harmonics and setting

$$\sum_{k=1}^{\ell}\beta_k\mathcal{J}_{2k-1}\left(\frac{\omega_{mn}}{\omega_0}\right) = \sum_{k=1}^{\ell}\alpha_k\omega_{mn}^{2k-1} + O(\omega_0^{-2}). \qquad (4.10)$$

Analytic expressions can easily be obtained for matching the harmonics to the coefficients in the gauge potential up to arbitrary order and, if necessary, higher-order harmonics can be added to compensate the $O(\omega_0^{-2})$ corrections order by order (see Appendix C). As an illustration, taking $\beta_1 = 2\alpha_1\omega_0$ and $\beta_2 = 2\omega_0(24\alpha_2\omega_0^2 + 3\alpha_1)$ for the expansion with two terms, the resulting protocol approximately reproduces the CD evolution at stroboscopic times $t = n\cdot T, n \in \mathbb{N}$. In finite systems, the exact gauge potential can always be obtained from a large enough ansatz, which can be reproduced as a Floquet Hamiltonian from a similarly large number of harmonics, such that exact counterdiabatic driving can always be realized through Floquet-engineering. However, while this protocol does not introduce new interactions in the Hamiltonian, the additional cost is that it requires high-frequency oscillations of both $\mathcal{H}$ and $\partial_\lambda\mathcal{H}$ rather than just $\partial_\lambda\mathcal{H}$.
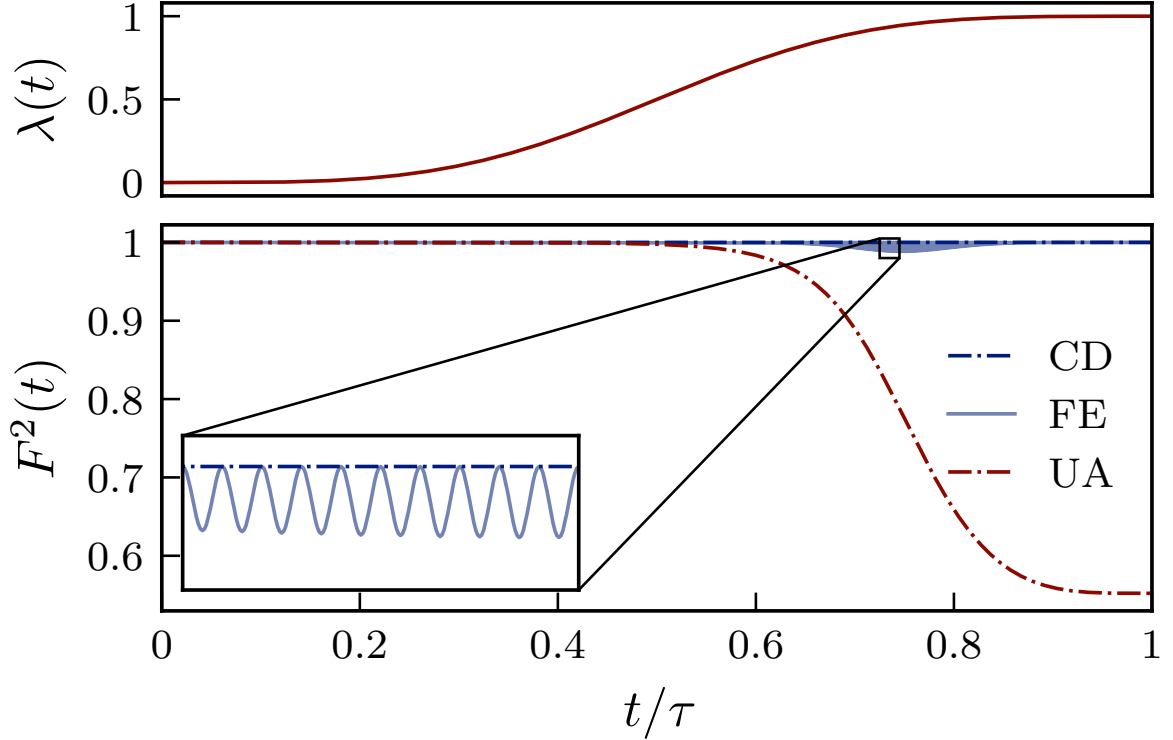
Figure 4·2: Fidelity in the 2-qubit system (4.11) for UA, CD and FE protocol. Increasing ω further suppresses the Floquet oscillations. Parameters $J = -1$, $h_z = 5$, $\tau = 0.1$, $\omega_0 = 10 \cdot 2\pi$ and $\omega = 250 \cdot \omega_0$.

4.3 Applications

This procedure can now be applied on various systems with increasing complexity. In all examples, we consider a specific driving protocol $\lambda(t) = \sin^2\left(\frac{\pi}{2} \sin^2\left(\frac{\pi t}{2\tau}\right)\right)$, ramping from $\lambda(0) = 0$ to $\lambda(\tau) = 1$ in such a way that $\dot{\lambda}$ and $\ddot{\lambda}$ vanish at the beginning and end of the protocol. λ behaves as an annealing parameter, and as first measure for the effectiveness of the protocol we initialize the system in the ground state for $\lambda = 0$ and calculate the fidelity of the time-evolved state w.r.t. the instantaneous ground state $F^2(t) = |\langle \psi(t)|\psi_0(\lambda(t))\rangle|^2$.

First consider a two-qubit system, for which all calculations can be performed analytically (see Appendix C),

$$\mathcal{H}(\lambda) = J\left(\sigma_1^x \sigma_2^x + \sigma_1^z \sigma_2^z\right) + h_z(\lambda - 1)\left(\sigma_1^z + \sigma_2^z\right). \tag{4.11}$$

The first-order expansion leads to

$$\mathcal{A}_\lambda^{(1)} = -\frac{Jh_z}{2}\frac{\left(\sigma_1^y\sigma_2^x + \sigma_1^x\sigma_2^y\right)}{J^2 + 4(\lambda-1)^2 h_z^2}. \tag{4.12}$$

Remarkably, this already returns the exact adiabatic gauge potential as presented in Ref. (Petiziol et al., 2018). This can be understood either by noting that $[\mathcal{H},[\mathcal{H},[\mathcal{H},\partial_\lambda\mathcal{H}]] \propto [\mathcal{H},\partial_\lambda\mathcal{H}]$, such that the higher-order commutators do not introduce new operators in the expansion, $\mathcal{A}_\lambda^{(\ell)} \propto \mathcal{A}_\lambda^{(1)}$, and the variational approach can be seen as a resummation of all higher-order terms exactly determining the prefactor. Second, this system behaves as a two-level system since any instantaneous Hamiltonian only couples $|\downarrow\downarrow\rangle$ and $|\uparrow\uparrow\rangle$, leading to a single excitation frequency which can be exactly cancelled by a single commutator.
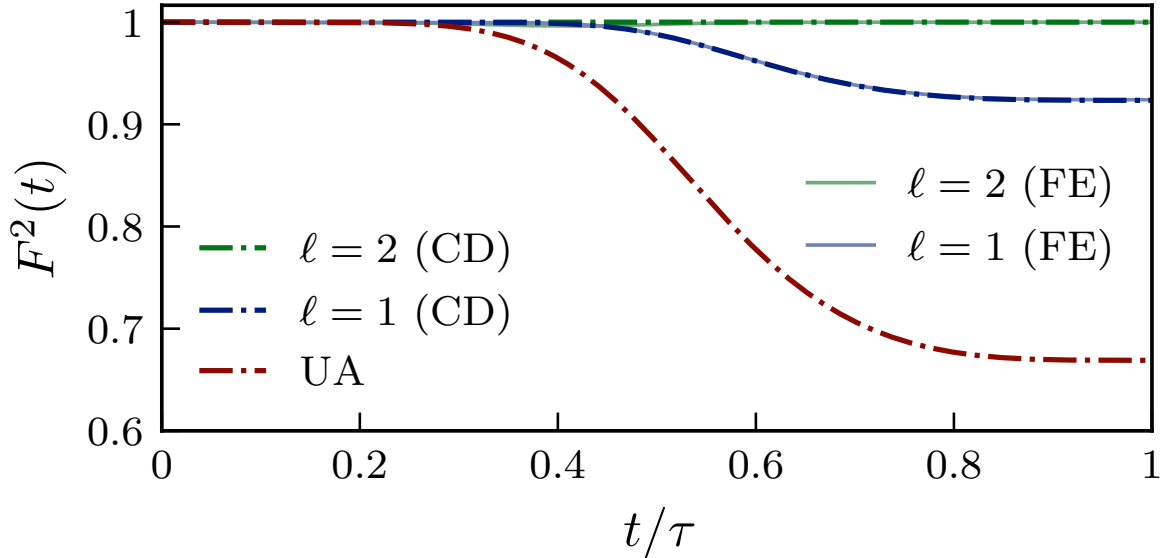
Figure 4·3: Fidelity in the 2-qubit system (4.14) for the UA, CD and FE protocol with $\ell = 1,2$. Parameters $\tau = 0.1$, $J = 1$, $h = 2$, $\omega_0 = 10 \cdot 2\pi$ and $\omega = 2.5 \cdot 10^{2\ell} \cdot \omega_0$.

The resulting CD driving can be realized up to $O(\omega_0^{-2})$ using a single harmonic as

$$\begin{aligned}
\mathcal{H}_{FE}(t) = {} & \left[1 + \frac{\omega}{\omega_0}\cos(\omega t)\right]\mathcal{H}(\lambda(t)) \\
& - \dot{\lambda}\frac{2h_z\omega_0\sin(\omega t)}{4J^2 + 16(\lambda(t)-1)^2 h_z^2}\left(\sigma_1^z + \sigma_2^z\right).
\end{aligned} \tag{4.13}$$

The results are illustrated in Fig. 4·2, where the duration of the protocol has been chosen in such a way that τ is too small for the unassisted (UA) protocol to accurately prepare the final Bell state $|\psi_0(\lambda = 1)\rangle = \frac{1}{\sqrt{2}}(|\uparrow\uparrow\rangle + |\downarrow\downarrow\rangle)$. Exact CD driving returns unit fidelity by definition, which can be well approximated (with a final error of the order 10^{-5}) using the proposed Floquet-engineered (FE) protocol.

Next, consider a two-qubit system behaving as a three-level system,

$$\mathcal{H}(\lambda) = -2J\sigma_1^z\sigma_2^z - h\left(\sigma_1^z + \sigma_2^z\right) + 2h\lambda\left(\sigma_1^x + \sigma_2^x\right), \tag{4.14}$$

where the total spin-0 state $|\uparrow\downarrow\rangle - |\downarrow\uparrow\rangle$ decouples from the rest of the Hilbert space. Transitionless protocols in three-level systems have recently attracted experimental (Vepsäläinen et al., 2019) and theoretical (Martínez-Garaot et al., 2014; Song et al., 2016; Vepsäläinen et al., 2018) interest, since exact protocols can no longer be trivially obtained. As shown in Fig. 4·3, the fidelity for the unassisted protocol is 67%, increasing to 92% for $\ell = 1$, before reaching approximate unit fidelity (up to an error 10^{-6}) for $\ell = 2$. Again, for $\ell = 2$ the variational approach returns the exact gauge potential, without any reference to exact diagonalization, since only two excitation frequencies are present. The FE protocol accurately reproduces the CD protocol.

Magnetic trap. – Moving to many-body systems, we consider the non-integrable Ising chain. Rather than simply changing the magnetic field uniformly, we will consider a more involved protocol where a local Gaussian magnetic trap is moved across the chain, similar to the 'optical tweezers' problem (Sørensen et al., 2016). In this problem, a set of initially localized spins are to be moved across the model while minimizing dissipation. The full

Hamiltonian is given by

$$\mathcal{H}(\lambda) = \mathcal{H}_0 - h_t \sum_{i=1}^{L} \exp\left[-\frac{(i - c_t(\lambda))^2}{w_t^2}\right] \sigma_i^z, \tag{4.15}$$

$$\mathcal{H}_0 = J \sum_{i=1}^{L-1} \sigma_i^z \sigma_{i+1}^z + h_z \sum_{i=1}^{L} \sigma_i^z + h_x \sum_{i=1}^{L} \sigma_i^x, \tag{4.16}$$

with $c_t(\lambda) = (1-\lambda)i_0 + \lambda i_f$. Tuning λ from 0 to 1 then drags the center of the trap $c_t(\lambda)$ with strength h_t and width w_t from site i_0 to i_f.

Rather than the fidelity, we consider the absorbed energy

$$E(t) - E_0(t) = \langle \psi(t)|\mathcal{H}(\lambda(t))|\psi(t)\rangle - \langle \psi_0(t)|\mathcal{H}(\lambda(t))|\psi_0(t)\rangle, \tag{4.17}$$

as a measure for dissipation, as shown in Fig. 4·4a for $\ell = 1, 2, 3$. It is clear that, for the given protocol duration, the UA protocol fails in reproducing the final state. This is remedied by including the CD terms with $\ell = 1, 2, 3$, reducing dissipation and absorbed energy by a factor 20 [1]. The Floquet drive succeeds in reproducing the CD results, with only minor deviations at intermediate times when $E_0(t)$ becomes extremal. The CD driving is also crucial in reproducing the final spin profile σ_i^z (Fig. 4·4b). While the proposed method seems to work particularly well for this type of model, as also observed in the optical case (Sels, 2018), this is representative for more general many-body systems. Finally, note that it was not the derivation of the gauge potential and the Floquet drive that was the computational bottleneck, but rather the time evolution as validation of the protocol. The former remain applicable for arbitrary large system sizes and should similarly lead to significant suppression of energy losses.

---

[1]This corresponds to an increase in the final fidelity from 2.8% to 90%

4.4 Conclusion and outlook

It was argued that the adiabatic gauge potential can be efficiently constructed as a series of variationally-optimized nested commutators. While constructions of the gauge potential and CD driving in complex systems generally rely on dynamical symmetries or exactly-solvable models, the proposed expansion can be constructed without having to resort to exact diagonalization and remains well-defined in general (chaotic) many-body systems. Due to the similarity between this series and the Magnus expansion in periodically-driven systems, this potential is easily realized through Floquet-engineering, such that the resulting approximate counterdiabatic/transitionless driving protocols can be realized via Floquet driving without introducing additional terms in the Hamiltonian. As illustrated on two-qubit systems and a non-integrable Ising chain, a small number of terms can already result in a drastic increase in fidelity in few- and many-body systems. This presents the usual trade-off in fast-forward protocols, where an increase in fidelity can be obtained provided precise control over the driving and access to large interaction strengths is available (Demirplak and Rice, 2008; Funo et al., 2017; Zheng et al., 2016).

In practice, this protocol is expected to mainly be useful when no efficient CD protocol can be obtained or realized, as in ergodic systems, and when a few commutators already provide a large increase in fidelity (as when e.g. the induced gap is large). The number of necessary commutators is expected to increase with a decreasing gap, with an additional drawback being the high energetic cost of the oscillations (by now common in Floquet systems), where higher orders necessitate higher driving frequencies and access to higher harmonics. The presented method requires neither the presence of dynamical invariants, scaling laws, or the closing of the commutators under some Lie algebra, common requirements for CD driving in complex systems.

Future applications and extensions are plenty. Current simulations were performed on spin systems, but this method can immediately be extended towards bosonic or fermionic

models. While the expansion of the gauge potential is particularly convenient for CD driving (where only a single state is involved), the exact potential contains information about the geometry of all quantum states, adiabatic deformations, integrability and its violations, approximate conservation laws,..., which can also be extracted from the current approximation. These methods should allow for the construction of approximately-conserved operators, and the similarity of the proposed expansion to the Magnus expansion allows for the realization of integrable gauge potentials analogous to integrable Floquet Hamiltonians (Gritsev and Polkovnikov, 2017).
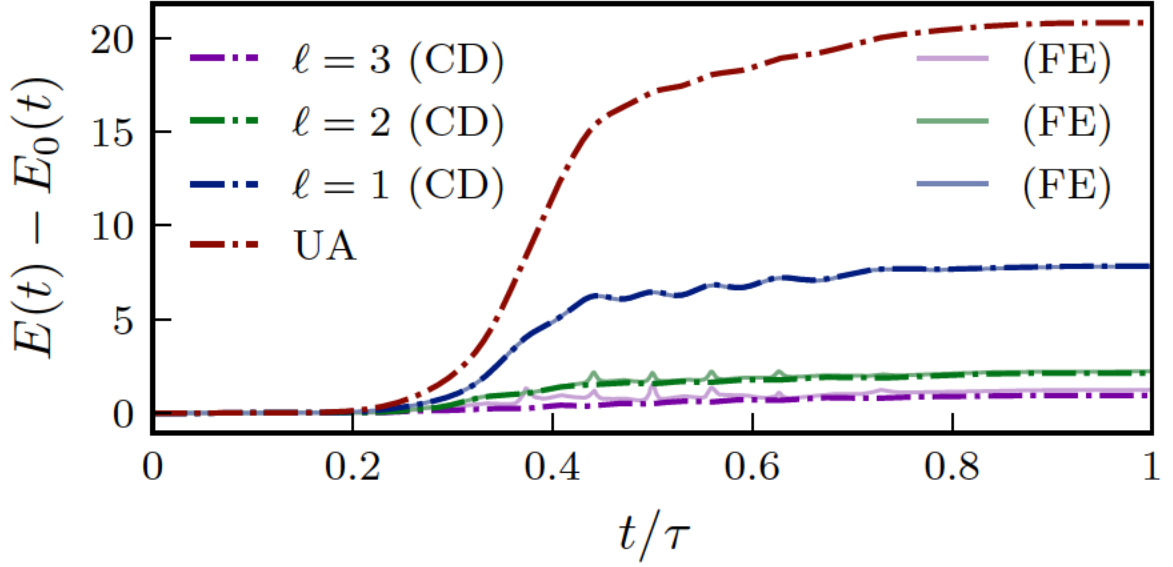
(a) Absorbed energy for the UA, CD and FE protocol with $\ell = 1, 2, 3$.
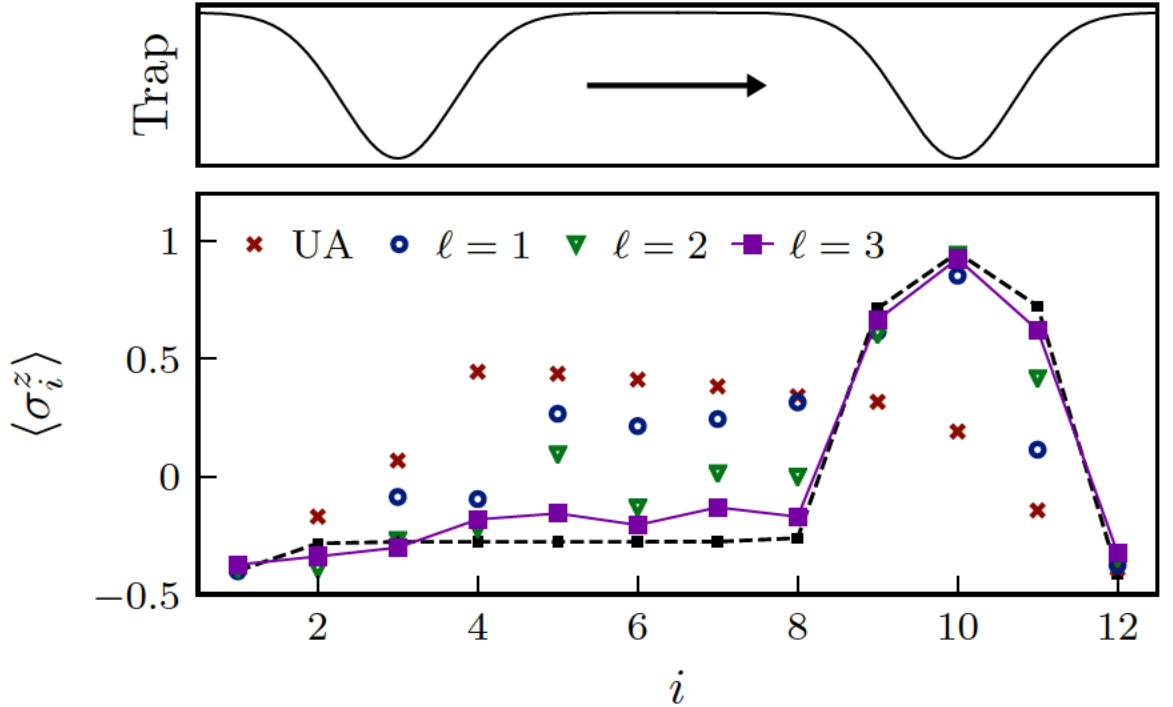
(b) Spin profile at time τ for the UA and the CD protocol with $\ell = 1, 2, 3$. Exact final profile is given in a dashed line.

Figure 4·4: Moving the magnetic trap in time $\tau = 0.5$ from site $n_0 = 3$ to site $n_f = 10$ for an Ising model with parameters $L = 12$, $J = -1$, $h_x = 0.8$, $h_z = 0.9$, $h_t = 8$, $w_t = 1$. $\omega_0 = 10 \cdot 2\pi$ and $\omega = 10^4 \cdot \omega_0$.

Chapter 5

Adiabatic Eigenstate Deformations as a Sensitive Probe for Quantum Chaos

This chapter was published in Physical Review X (Pandey et al., 2020).

5.1 Introduction

Finding signatures of chaos in the quantum world has been a long-standing puzzle (Haake et al., 2013; Stöckmann, 1999; Berry, 1989). In the last few years exciting progress has been made on characterizing the effects of chaos on dynamical properties of quantum many-body systems, see Fig. 5·1 (Shenker and Stanford, 2014; Maldacena et al., 2016; Rakovszky et al., 2018; Nahum et al., 2018; Von Keyserlingk et al., 2018; Swingle, 2018; Khemani et al., 2018; Kudler-Flam et al., 2020). Classical chaos is usually described in terms of an exponential sensitivity of trajectories to initial conditions (Cencini et al., 2010). However, the quantum world precludes any definition of chaos in terms of physical trajectories due to the Heisenberg uncertainty principle. Alternatively, chaos can be defined in terms of the absence of integrability. Classical Liouville-Arnold integrability is formulated in terms of independent Poisson-commuting integrals of motion. Again, although there have been many attempts to characterize quantum integrability in a similar way, no such unique definition exists (Caux and Mossel, 2011; Yuzbashyan and Shastry, 2013; Yuzbashyan et al., 2016; Ilievski et al., 2016).

In the last two decades, Random Matrix Theory (RMT) (Brody et al., 1981; Guhr et al., 1998; Mehta, 2004) has shown outstanding success in the understanding of quantum chaos.
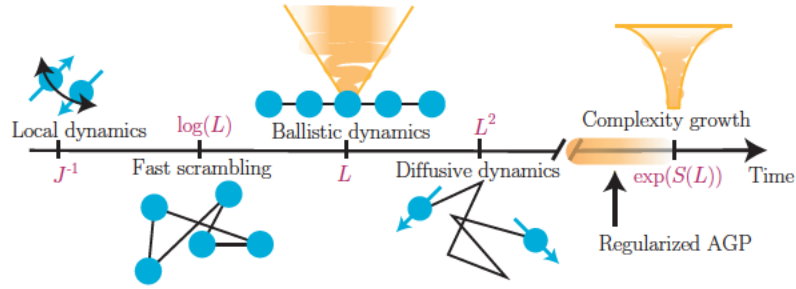
Figure 5·1: Signatures of Chaos. Quantum chaos manifests itself in a vast range of different phenomena, each relevant up to a particular system-size dependent timescale. At the earliest times, where dynamics are limited by the local bandwidth, one can see the onset of chaos. In systems without spatial locality this could lead to fast scrambling, allowing one to identify a Lyapunov exponent. Systems with spatial locality are further characterized by an additional, so-called, butterfly velocity. While this ballistic propagation ends at times $O(L)$, diffusive dynamics continues up to the Thouless time $O(L^2)$. All local dynamics has now come to a stop, nonetheless operators keep spreading over operator space, becoming increasingly more complex. This process continues for exponentially long times, only stopping at the Heisenberg time $\exp(S(L))$.

Following the work of Wigner (Wigner, 1958; Wigner, 1993), Bohigas, Giannoni, and Schmit (Bohigas et al., 1984) conjectured that the energy-level statistics of all quantum systems whose classical analogues are chaotic should show level repulsion and belong to one of three universal classes depending upon their symmetry: the Gaussian orthogonal ensemble, the Gaussian unitary ensemble, or the Gaussian symplectic ensemble. On the other hand, according to the Berry-Tabor conjecture (Berry and Tabor, 1977), integrable systems have uncorrelated energy levels and usually exhibit Poissonian level spacing statistics. These ideas were later extended to generic quantum systems and tested numerically under the general framework of the eigenstate thermalization hypothesis (ETH) (Deutsch, 1991; Srednicki, 1994; Rigol et al., 2008; Borgonovi et al., 2016; D'Alessio et al., 2016; Deutsch, 2018). By now, the emergence of the random matrix behavior of quantum eigenstates is an accepted definition of quantum chaos.

Numerically, two additional steps are required before one can accurately compare the

statistical properties (e.g. through level statistics or the spectral form factor (Müller et al., 2004; Bertini et al., 2018)) of a particular quantum system with the predictions of RMT: (1) remove any symmetries; and (2) rescale the spectrum, setting the local mean level spacing to unity (also called unfolding the spectrum). Firstly, if symmetries are not removed, energy levels in different symmetry sectors don't have any correlations, so that spectra of chaotic systems can show Poissonian distributions (Gubin and F. Santos, 2012; Kudo and Deguchi, 2003). However, finding *all* symmetries of a many-body Hamiltonian is computationally hard without any physical intuition, since this effectively involves searching for all possible (local) operators that commute with the Hamiltonian. Secondly, there are various methods to unfold the spectrum, and it is known that statistics, especially ones measuring long-range correlations, can be sensitive to the adopted unfolding procedure (Gómez et al., 2002). Moreover, the procedure can also exhibit finite-size effects. In light of these issues, it is advisable rather to use the ratio of two consecutive level spacings (Oganesyan and Huse, 2007; Atas et al., 2013) or survival probability (see Ref. (Torres-Herrera and Santos, 2017; Schiulaz et al., 2019)).

Here we propose an alternative tool to detect chaos in quantum systems, based on the rate of deformations of eigenstates under infinitesimal perturbations. Mathematically, the distance between nearby eigenstates (also known as the Fubini-Study metric (Kolodrubetz et al., 2017; Page, 1987; Kobayashi and Nomizu, 1963; Provost and Vallee, 1980)) can be expressed as the Frobenius norm of the so-called adiabatic gauge potential (AGP) (Berry, 2009; Demirplak and Rice, 2005; Demirplak and Rice, 2003; Kolodrubetz et al., 2017), which is exactly the operator that generates such deformations. It is straightforward to show that this norm should scale exponentially with the system size in chaotic systems satisfying ETH (Kolodrubetz et al., 2017). In this sense, quantum chaos manifests itself through an exponential sensitivity of the eigenstates to infinitesimal perturbations, which can be viewed as an analogue to classical chaos, reflected in the exponential sensitivity of

trajectories to such perturbations. Moreover, unlike standard probes of RMT such as the spectral form factor (see e.g. Ref. (Šuntajs et al., 2019)) or the closely related survival probability (see Ref. (Torres-Herrera and Santos, 2017; Schiulaz et al., 2019)), as well as level statistics, which only depend on the eigenvalues of the Hamiltonian, the AGP norm is sensitive to both the level spacings and the specific kind of adiabatic deformation (perturbation).

We find that the norm of the AGP shows a remarkably different, and extremely sensitive, scaling with system size for integrable and chaotic systems: polynomial versus exponential. In our method, we do not need to remove any symmetries before computing the AGP norm needed in the analysis of the level spacing distributions and do not need to average over different Hamiltonians, which is necessary to analyze the (non self-averaging) spectral form factor. We show that one can detect chaos through the sharp crossover between the polynomial and exponential scaling of the norm. The sensitivity of this norm to chaotic perturbations is orders of magnitude greater than that of the aforementioned methods. Using this approach, we find several, previously-unexpected, results for a particular but fairly generic integrable XXZ spin chain with additional small perturbations: i) The strength of the integrability-breaking perturbation scales exponentially down with the system size, much faster than in previous estimates (Modak and Mukerjee, 2014; Modak et al., 2014); ii) integrability-breaking deformations immediately lead to an exponential scaling of the norm of the AGP, showing that chaotic perturbations can be already detected in the integrable regimes; and iii) in the presence of small integrability-breaking terms, the system can exhibit exponentially slow relaxation dynamics, which is similar to the slow dynamics observed in some classical nearly-integrable systems like the Fermi-Pasta-Ulam-Tsingou (FPUT) chain (Gallavotti, 2007; Danieli et al., 2017; Pace and Campbell, 2019). We also find that such relaxation dynamics are very different for observables conjugate (see Eq. (5.2) below) to integrable and chaotic directions (perturbations) of the Hamiltonian. We

find similar results for an Ising model, where the integrability is broken by introducing a longitudinal field.

The connection with relaxation is not surprising, since one representation of the AGP is in terms of the long-time evolution of a local operator conjugate to the coupling. Hence, our results relate to recent studies of information propagation through operator growth in quantum many-body systems (Eisert et al., 2015; Swingle, 2018; Lewis-Swan et al., 2019), where chaotic and integrable systems are again expected to exhibit qualitatively different behavior (e.g. in operator entanglement (Zhou and Luitz, 2017; Alba et al., 2019) and Lanczos coefficients (Parker et al., 2019; Avdoshkin and Dymarsky, 2019)). Whereas most of the previous works focused mainly on short-time effects, here we effectively focus on dynamics and operator growth at times that are exponentially long in the system size (Fig. 5·1).

5.2   Adiabatic Gauge Potential

Before proceeding, let us define the adiabatic gauge potential (AGP) and discuss some of its key properties. Given a Hamiltonian $H(\lambda)$ depending on a parameter λ, the adiabatic evolution of its eigenstates as we vary this parameter is generated by the AGP as (in units with $\hbar = 1$):

$$\mathcal{A}_\lambda |n(\lambda)\rangle = i\partial_\lambda |n(\lambda)\rangle, \quad H(\lambda)|n(\lambda)\rangle = E_n(\lambda)|n(\lambda)\rangle. \tag{5.1}$$

Using the Hellmann-Feynman theorem, it is easy to see that the matrix elements of the AGP between such eigenstates are given by

$$\langle m|\mathcal{A}_\lambda|n\rangle = -\frac{i}{\omega_{mn}}\langle m|\partial_\lambda H|n\rangle, \tag{5.2}$$

where $\omega_{mn} = E_m(\lambda) - E_n(\lambda)$, $\partial_\lambda H$ is the operator conjugate to the coupling λ, and we have made the dependence on λ implicit. The diagonal elements of $\mathcal{A}_\lambda$ can be chosen arbitrarily due to the gauge freedom in defining the phases of eigenstates. A convenient

choice consists of setting all diagonal elements equal to zero. For simplicity we will assume there are no degeneracies in the spectrum, but as will be clear shortly, this assumption is not necessary and does not affect any of the results below. We define the L_2 (Frobenius) norm, also called Hilbert–Schmidt norm, of this operator as:

$$||\mathcal{A}_\lambda||^2 = \frac{1}{\mathcal{D}} \sum_n \sum_{m \neq n} |\langle n | \mathcal{A}_\lambda | m \rangle|^2, \tag{5.3}$$

where $\mathcal{D}$ is the dimension of the Hilbert space.

This expression should scale exponentially with the system size in chaotic systems satisfying ETH: $||\mathcal{A}_\lambda||^2 \sim \exp[S]$, where S is the entropy of the system (Kolodrubetz et al., 2017). Within ETH, the off-diagonal matrix elements of local operators, including $\partial_\lambda H$, scale as $\langle m | \partial_\lambda H | n \rangle \propto \exp[-S/2]$ (Srednicki, 1994; D'Alessio et al., 2016) while the minimum energy gap between states, ω_{mn}, scales as $\exp[-S]$. The scaling of individual matrix elements was already explored in the literature to study the crossover between chaotic and non-ergodic behavior, e.g. in the context of disordered systems (Serbyn et al., 2015; Crowley and Chandran, 2019) and integrability breaking (LeBlond et al., 2019; Mondaini and Rigol, 2017). As we will demonstrate, the exponential scaling of the norm of the AGP can be used to detect the emergence of chaotic behavior in the system with tremendous (exponential) precision.

However, Eq. (5.2) is not particularly convenient: the norm of the exact AGP can be dominated by the smallest energy difference between eigenstates, and as such it is highly unstable and difficult to analyze, especially close to the ergodicity transition. Accidental degeneracies in the spectrum that are lifted by $\partial_\lambda H$ also cause the norm to formally be infinite. To resolve this issue, it is convenient to instead define a 'regularized' AGP as follows:

$$\langle m | \mathcal{A}_\lambda(\mu) | n \rangle = -i \frac{\omega_{mn}}{\omega_{mn}^2 + \mu^2} \langle m | \partial_\lambda H | n \rangle, \tag{5.4}$$

where μ is a small energy cutoff. For the sake of brevity, we are going to drop the argument μ and unless specified otherwise $\mathcal{A}_\lambda$ refers to the regularized AGP. This has a clear physical intuition: instead of considering transitions (matrix elements) between individual eigenstates, we now only consider transitions between energy shells with width μ. For eigenstates with $|\omega_{mn}| \gg \mu$, this reproduces the exact AGP, whereas in the limit $|\omega_{mn}| \ll \mu$, the AGP no longer diverges but reduces to a constant. Alternatively, within the operator growth representation (see Eq. (5.11) below), μ^{-1} has the interpretation of a cutoff time. Numerically, this regularization has the immediate advantage that it gets rid of any problem with (near-)divergences. Note that μ does not need to be system-size independent for this. Interestingly, as long as $\mu \propto \exp[-S]$, the norm of the AGP within chaotic systems should also remain proportional to $\exp[S]$. We can use this flexibility in defining μ to our advantage, choosing it to be parametrically larger than the level spacing to eliminate any effect of accidental degeneracies, but still exponentially small to minimize the deviation from the exact AGP. We find that choosing $\mu(L) \propto L\exp[-S(L)]$, where L is the system size, is the most convenient choice (see Appendix D.1).

From Eqs. (5.3) and (5.4) the norm of the regularized AGP reads

$$||\mathcal{A}_\lambda||^2 = \frac{1}{\mathcal{D}} \sum_n \sum_{m \neq n} \frac{\omega_{mn}^2}{(\omega_{nm}^2 + \mu^2)^2} |\langle m|\partial_\lambda H|n\rangle|^2 \tag{5.5}$$

$$= \int_{-\infty}^{\infty} d\omega \frac{\omega^2}{(\omega^2 + \mu^2)^2} \overline{|f_\lambda(\omega)|^2}, \tag{5.6}$$

where in the second equation we replaced the summation with an integration over the energy difference $\omega_{mn} = E_m(\lambda) - E_n(\lambda)$ and also defined the response function

$$\overline{|f_\lambda(\omega)|^2} = \frac{1}{\mathcal{D}} \sum_n \sum_{m \neq n} |\langle n|\partial_\lambda H|m\rangle|^2 \delta(\omega_{nm} - \omega) \tag{5.7}$$

$$= \frac{1}{\mathcal{D}} \sum_n \int_{-\infty}^{\infty} \frac{dt}{4\pi} e^{i\omega t} \langle n|\{\partial_\lambda H(t), \partial_\lambda H(0)\}|n\rangle_c,$$

where $\{...\}$ stands for the anti-commutator and connected correlation function is given as:

$$\langle n|\partial_\lambda H(t)\partial_\lambda H(0)|n\rangle_c = \langle n|\partial_\lambda H(t)\partial_\lambda H(0)|n\rangle - \langle n|\partial_\lambda H(t)|n\rangle\langle n|\partial_\lambda H(0)|n\rangle. \tag{5.8}$$

Formally, this function represents an average over eigenstates n of the sum of the squares of the off-diagonal matrix elements $|\langle n|\partial_\lambda H|m\rangle|^2$ with a fixed energy difference $\omega_{mn} = \omega$, which can also be obtained as the Fourier transform of the non-equal time correlation function of $\partial_\lambda H$. Within the ETH ansatz, this function exactly coincides with the (averaged over eigenstates) square of the function $f_\lambda(\omega)$ introduced by M. Srednicki (Srednicki, 1994), according to

$$\langle m|\partial_\lambda H|n\rangle = f_\lambda(\omega, \bar{E})e^{-S(\bar{E})/2}\sigma_{mn}, \tag{5.9}$$

$$\omega = E_m - E_n, \ \bar{E} = (E_n + E_m)/2, \tag{5.10}$$

with σ_{nm} a random variable with zero mean and unit variance. Recently it was shown that the function $|f_\lambda(\omega)|^2$ remains well defined and smooth in generic integrable systems (LeBlond et al., 2019; Brenes et al., 2020b; Brenes et al., 2020a).

Alternatively, it is convenient to rewrite the regularized AGP as a time integral (Jarzynski, 1995; Claeys et al., 2019):

$$\mathcal{A}_\lambda = -\frac{1}{2} \int_{-\infty}^{\infty} dt \, \text{sgn}(t) \, e^{-\mu|t|} \left(\partial_\lambda H\right)(t), \tag{5.11}$$

where sgn(t) is the sign function and

$$(\partial_\lambda H)(t) = e^{iHt}(\partial_\lambda H)e^{-iHt} \qquad (5.12)$$

is the operator conjugate to the coupling λ in the Heisenberg representation. The exponential factor $\exp[-\mu|t|]$ can be seen as a particular choice of a filter function in the context of quasi-adiabatic continuation (Hastings, 2010; Bachmann et al., 2012; Bachmann et al., 2017). Notably, Eq. (5.11) remains valid for classical systems (Jarzynski, 1995) and therefore the scaling of the AGP norm can be used to detect classical chaos, which we leave for future work.

Further, Eq. (5.11), makes clear that the inverse of the parameter μ plays the role of a cutoff time, limiting the growth of $(\partial_\lambda H)(t)$ in the operator space. Note that this time is much longer than the time scales generally studied in literature (e.g, the time scale characterizing the ballistic propagation of information $t_{LR} = L/v_{LR}$, where v_{LR} is the Lieb-Robinson velocity and L is the system size)(Eisert et al., 2015; Swingle, 2018; Lewis-Swan et al., 2019). One of the outcomes of our work is that an exponential sensitivity to detecting the onset of chaos requires access to exponentially long time scales (Fig. 5·1).

5.3 Numerical results

We can now compare with results for the AGP in integrable/non-ergodic models. Specifically, we move to the analysis of the norm of the regularized AGP for a specific integrable XXZ model with open boundary conditions (Orbach, 1958; Yang and Yang, 1966; Sutherland, 2004; Gaudin, 2014; Franchini, 2017), whose Hamiltonian is given below:

$$H_{\text{XXZ}} = \sum_{i=1}^{L-1}(\sigma_{i+1}^x\sigma_i^x + \sigma_{i+1}^y\sigma_i^y) + \Delta\sum_{i=1}^{L-1}\sigma_{i+1}^z\sigma_i^z. \qquad (5.13)$$

We will now consider the effects of various integrability-breaking terms. Although the thermodynamics of the above model can be solved exactly using the Bethe ansatz (Orbach,

1958; Yang and Yang, 1966; Sutherland, 2004; Gaudin, 2014; Franchini, 2017), we still don't have access to matrix elements of general local operators $\langle n|\partial_\lambda H|m\rangle$ and the exact AGP remains out of reach even in the integrable limit. Consequently, there are also no results on the scaling of the AGP with increasing system size.

For reference, we also analyze an Ising model in the presence of a longitudinal field whose Hamiltonian is given below:

$$H_{\text{Ising}} = \sum_{i=1}^{L-1} \sigma_{i+1}^z \sigma_i^z + h_z \sum_{i=1}^{L} \sigma_i^z + h_x \sum_{i=1}^{L} \sigma_i^x. \tag{5.14}$$

where open boundary conditions are chosen for the chaotic Ising model. This model has a trivially-integrable limit at zero longitudinal field $h_z = 0$, which maps to a system of free fermions (Sachdev, 2007). In this non-interacting (free) limit, the AGP can be computed analytically (del Campo et al., 2012; Kolodrubetz et al., 2017) (see Appendix D.2). In the presence of the longitudinal field, this model shows a Wigner-Dyson type distribution of the energy level spacings, which is particularly pronounced at the parameters $h_x = (\sqrt{5}+5)/8$ and $h_z = (\sqrt{5}+1)/4$ (Kim and Huse, 2013). We will use these values when computing the AGP in the chaotic regime.

In Fig. 5·2, we show the AGP norm scaled by the system size $||\mathcal{A}_\lambda||^2/L$ [1] for the interacting XXZ model and the Ising model both at the chaotic and non-interacting points. Fig. 5·2 clearly shows the remarkably different scalings with system size L for chaotic, integrable and free models. For chaotic models, the scaled AGP norm shows the exponential scaling expected from ETH. For the free model, the scaled norm is system-size independent up to exponentially small corrections away from the critical point (see Appendix D.2). For the integrable XXZ model, the scaled AGP norm shows a nontrivial polynomial scaling: $||\mathcal{A}_\lambda||^2/L \propto L^\beta$. We find that the exponent β is non-universal and depends on the choice of the anisotropy Δ (see Appendix D.4). We have chosen $\lambda = h_x$ for both the integrable and

---

[1] We divide the norm of the AGP by the system size for extensive perturbations, to account for the trivial extensivity of the AGP
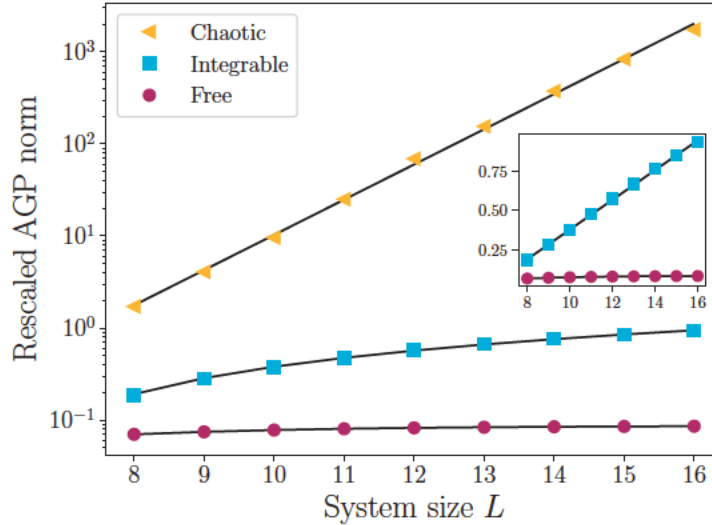
Figure 5·2: AGP scaling. The rescaled norm $||\mathcal{A}_\lambda||^2/L$ is presented as a function of system size for the chaotic Ising model (yellow triangles), the integrable interacting XXZ model (blue squares) and the integrable non-interacting Ising model (red dots). The data corresponding to the chaotic Ising and integrable XXZ models are fitted to an exponential and a linear function respectively (black lines). For the Ising models we set $\lambda = h_x$ and for the XXZ model we set $\lambda = \Delta$. *Inset:* Rescaled AGP norm for the free and interacting integrable models on a linear graph. *Parameters:* $h_x = 0.8$ for free model, $\Delta = 1.1$ for integrable model, $h_x = (\sqrt{5}+5)/8$ and $h_z = (\sqrt{5}+1)/4$ for chaotic model. $||\mathcal{A}_{\mathrm{chaotic}}||^2 \sim e^{0.9L}$, $||\mathcal{A}_{\mathrm{int}}||^2 = 0.09L - 0.56$.

non-integrable Ising models and $\lambda = \Delta$ for the XXZ model.

While the exponential scaling of the AGP norm in the chaotic regime and the constant AGP norm in the free model are expected, the polynomial scaling of this norm of the XXZ integrable model is very interesting and leads to non-trivial conclusions. Recently, LeBlond *et al.* (LeBlond et al., 2019) have shown that the matrix elements of local operators in this integrable model are not sparse (as compared to the matrix elements of non-interacting integrable models). The latter implies that Eq. (5.6) for the AGP norm still applies, where $|f_\lambda(\omega)|^2$ can also be found from the Fourier transform of the symmetric correlation function (see Appendix D.3). Since we have chosen μ to be exponentially small in the system size

and $||\mathcal{A}_\lambda||^2$ is polynomially (not exponentially) large, the function $f_\lambda(\omega)$ must vanish as $\omega \to 0$. This behavior is to be contrasted with chaotic systems where at small ω this function saturates at a constant value, in agreement with the Random Matrix Theory (D'Alessio et al., 2016).

5.4 Integrability breaking

Having established the scaling of the AGP norm in three different regimes, we will move to the analysis of integrability breaking by small perturbations and focus on a more generic XXZ model. As an integrability-breaking term, we choose a magnetic field coupled to a single spin in the middle of the chain, acting as a single-site defect,

$$V = \sigma^z_{\lceil (L+1)/2 \rceil}, \tag{5.15}$$

where $\lceil (L+1)/2 \rceil$ stands for the smallest integer greater than or equal to $(L+1)/2$. Then we analyze the AGP for the total Hamiltonian

$$H = H_{XXZ} + \varepsilon_d V, \tag{5.16}$$

as a function of the integrability-breaking parameter ε_d. Interestingly, in Ref. (Santos, 2004) it was argued based on the same model that even a single site defect is sufficient to induce chaos in the thermodynamic limit. In Appendix D.5, we analyze an extensive integrability-breaking perturbation by considering $H = H_{XXZ} + \Delta_2 V$ with $V = \sum_i \sigma^z_{i+2} \sigma^z_i$ and find the results to be consistent. The similarity between the effects of local and global perturbations on spectral properties was also found in Ref. (Torres-Herrera and Santos, 2014).

A challenging question is how quickly chaos emerges when a non-ergodic, or integrable system, is subjected to an integrability-breaking perturbation. In classical systems with few degrees of freedom, it is known from KAM theory that integrable systems are stable against
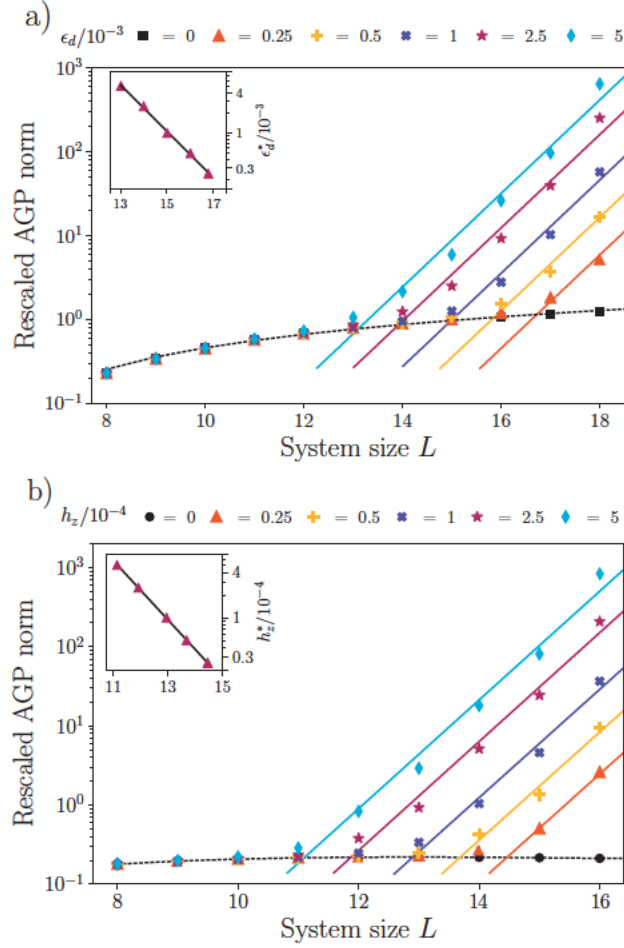
Figure 5·3: Integrability breaking. The rescaled AGP norm $||\mathcal{A}_\lambda||^2/L$ of a) the XXZ chain with $\lambda = \Delta$ and b) the Ising chain with $\lambda = h_x$. Both models show a sharp crossover from polynomial to exponential scaling with system size, even for very small integrability breaking perturbation strengths. With decreasing perturbation strength, the system size where this crossover happens increases. Straight lines are the exponential fits with $||A_\lambda||^2/L \sim e^{\beta L}$, where $\beta = 1.28$ for the XXZ and $\beta = 1.58$ for the Ising model. The insets show the scaling of the crossover point, i.e. the dependence of the integrability-breaking perturbation on system size. The critical perturbation strength scales exponentially with system size, with $\epsilon_d^* \sim e^{-0.8L}$ for the XXZ chain and $h_z^* \sim e^{-0.9L}$ for the Ising chain. *Parameters:* a) $\Delta = 1.1$, b) $h_x = 0.75$.

small perturbations (Moser, 1962; Kolmogorov, 1954; Arnold, 1963). It is widely believed that quantum chaos is generally induced by infinitesimal perturbations in the thermody-

namic limit (Rabson et al., 2004; Santos and Rigol, 2010; Modak and Mukerjee, 2014; Modak et al., 2014), with the potential exception of many-body localization (Nandkishore and Huse, 2015; Abanin and Papić, 2017), although the precise scaling of the critical perturbation strength with the system size remains an open question. A standard limitation of numerical approaches (using e.g., level statistics or spectral form factor) addressing this question is the small system sizes amenable to simulations, where it is possible to reliably extract the data.

In Fig. 5·3 a) we show the scaling of the norm of the AGP as a function of the system size for different perturbation strengths ε_d. We choose the zero magnetization subspace of the XXZ chain with number of spins up $N_\uparrow = \lfloor L/2 \rfloor$, where $\lfloor L/2 \rfloor$ stands for the largest integer less than or equal to $L/2$, and for the direction of the AGP we choose $\lambda = \Delta$, i.e. as in Fig. 5·2. For the cutoff, we choose $\mu = L\mathcal{D}_0^{-1}$, where $\mathcal{D}_0$ is the dimension of zero magnetization sector. From the figure, we clearly see a sharp crossover in the scaling of the norm of the AGP as a function of system size from the integrable power law behavior to the chaotic exponential behavior. The straight lines are obtained by a least squares fit, with the slope extracted for the largest ε_d and then used for other perturbations. After the best fitting parameters were found, the critical system sizes were obtained for a particular defect energy at which the integrable (polynomial) and chaotic (exponential) curves intersect. These values are shown in the inset of Fig. 5·3 a), showing a clear exponential scaling of the critical perturbation strength with the system size. Interestingly, the slope of the exponential scaling $\beta \approx 1.28$ is almost twice the slope predicted by ETH, $\beta = \log(2) \approx 0.69$. Notably, the slope of $2\log(2)$ is the largest possible growth rate of the AGP norm (see Appendix D.3). In the next section we will return to this point and relate it to the emergence of relaxation times that are exponentially long in system size.

Consistent results are obtained for the Ising model (5.14), where one can consider breaking the integrability of the transverse field Ising model ($h_z = 0$) by introducing a small

non-zero h_z-field, while probing the integrable direction $\lambda = h_x$. The results are shown in Fig. 5·3 b). As in the XXZ case, we observe a sharp crossover from the the unperturbed scaling of the AGP norm (see Fig. 5·2) to exponential scaling with an exponent that exceeds the ETH expectation, once again having implications on the long time relaxation of the system.
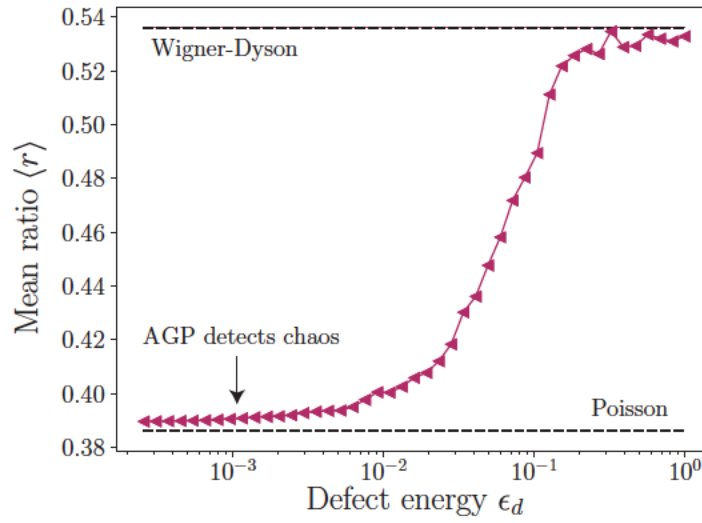
Figure 5·4: Energy level statistics. Mean ratio of energy level spacings $\langle r \rangle$ as a function of defect energy ϵ_d for an XXZ chain of length $L = 16$ at anisotropy $\Delta = 1.1$. The arrow indicates the value of the defect energy where chaos can be detected (for $L = 16$) using the exponential scaling of AGP norm.

To contrast the scaling of the AGP norm with more traditional approaches in Fig. 5·4, we show the mean ratio of energy level statistics as a function of defect energy for system size $L = 16$. Given subsequent energy level spacings $s_n = E_{n+1} - E_n$, this ratio is defined as

$$r_n = \frac{\min(s_n, s_{n+1})}{\max(s_n, s_{n+1})}. \tag{5.17}$$

For non-ergodic systems and Poissonian level statistics, $\langle r \rangle \approx 0.386$, whereas for chaotic systems and Wigner-Dyson statistics $\langle r \rangle \approx 0.536$. In this model, the average ratio $\langle r \rangle$ shows

the crossover from non-ergodic to ergodic behavior at $\varepsilon_d^* \sim 0.1$ (Chavda et al., 2014). This crossover value of ε_d has a very weak dependence on the system size. In comparison, for the same system size $L = 16$ the AGP norm shows a clear crossover to chaos for a much smaller $\varepsilon_d^* \sim 10^{-3}$ (see Fig. 5·3 a)). For larger system sizes, the gap between the chaos thresholds extracted by these two methods becomes even larger. Moreover, we also estimated the critical perturbation strength using the spectral form factor for the same system size $L = 16$. Since this generally doesn't self-average (Prange, 1997; Braun and Haake, 2015), we added disorder to the *zz*-coupling in the Hamiltonian (Eq. (5.16)) which reduces the sensitivity of this probe to detect chaos. From the spectral form factor we find $\varepsilon_d^* \sim 0.1$, a value where the level statistics is roughly half way between Poisson and Wigner-Dyson (see Fig. 5·4). Such a correspondence was also observed for disordered models in Ref. (Šuntajs et al., 2019).

We believe that the reason that the AGP norm is so much more sensitive is that it effectively detects the change in the differential of the norm with the system size. The absolute value of the AGP norm at the threshold is still much closer to the integrable value than to the chaotic one. Such a differential is much harder to detect using other measures, e.g. the level spacing ratio, because this crossover is much smoother, and it is harder to define a sharp threshold.

In Fig. 5·5 we show similar results, now choosing to deform the Hamiltonian in the direction of the integrability-breaking operator itself, i.e. $\lambda = \varepsilon_d$ for the XXZ chain and $\lambda = h_z$ for the Ising chain. We choose to work in the full Hilbert space with dimension $\mathcal{D} = 2^L$. We find that the AGP norm shows exponential scaling even when $\varepsilon_d = 0$, i.e. when the Hamiltonian is integrable. We find a good fit to the exponential scaling $||\mathcal{A}_\lambda||^2 \sim e^{\beta L}$, with now $\beta \approx \log(2)$. Again we confirm that the results remain the same if we use an extensive integrability-breaking term instead (see Appendix D.6).
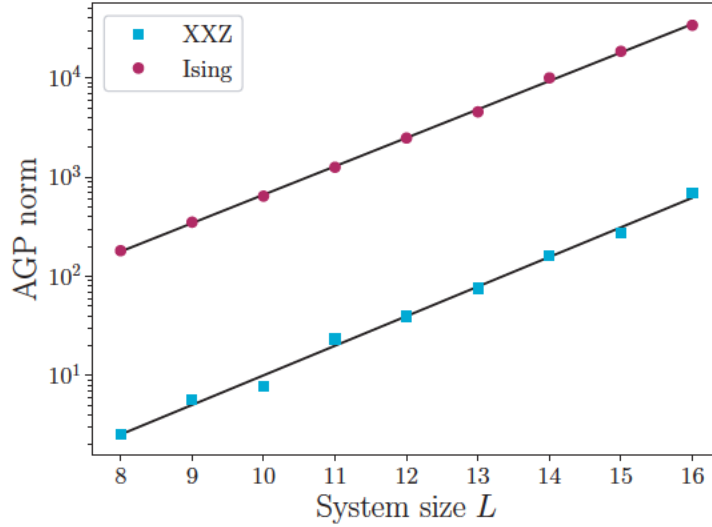
Figure 5·5: Integrability-breaking deformation at the integrable point. The AGP norm $||\mathcal{A}_\lambda||^2$ shows an exponential scaling at the integrable point for the XXZ chain (squares) with $\lambda = \varepsilon_d$ and the Ising chain (circles) with $\lambda = h_z$. The black lines correspond to exponential fits, i.e. $||\mathcal{A}_\lambda||^2 \sim e^{\beta L}$, where $\beta \approx \log(2)$. *XXZ Parameters:* $\Delta = 1.1, \varepsilon_d = 0$, *Ising Parameters:* $h_x = 0.75, h_z = 0$.

5.5 Long relaxation times

We already mentioned a very peculiar fact following from Fig. 5·3: namely, instead of the perhaps expected crossover of the integrable polynomial scaling of the AGP norm to the ETH exponential scaling with the slope $\log(2)$ the AGP crosses over to the exponential scaling regime with the slope $\beta = 1.28$, which is almost twice as large as the slope predicted by ETH, $\beta = \log(2) \approx 0.69$. Combining this result with Eq. (5.6), which we highlight works in both integrable and nonintegrable regimes, we conclude that at small ω the function $|f_\lambda(\omega)|^2$ should scale exponentially with the system size. This implies that the system must have exponentially long relaxation times, which are known to exist in classical chaotic systems like the FPUT chain (Gallavotti, 2007; Danieli et al., 2017; Pace and Campbell, 2019). Although we cannot rule out the eventual relaxation to the ETH value for system sizes greater than those we have studied, our results here suggest that, while

an exponentially small perturbation is sufficient to induce chaos in the system, it takes an exponentially long time for the system to relax to the steady state. In Appendix D.5, we show that a similar behavior persists if we break the integrability by a small extensive perturbation, here chosen as the second nearest-neighbor Ising interactions. We found the same slope of $\beta \approx 1.28$, ruling out that this scaling is induced by the ultra-local nature of the perturbation in Fig. 5·3 a). As the defect energy is increased further to large values (in particular, $\varepsilon_d \sim 1$), we find that the slope of AGP norm's exponential growth reduces again to the ETH value of $\beta \approx \log(2)$ (see Appendix D.6).

To make the connection between the AGP norm and the relaxation time more explicit let us observe that from Eq. (5.6) for sufficiently small μ one can make the following estimate:

$$||\mathcal{A}_\lambda||^2 \sim \frac{|f_\lambda(\mu)|^2}{\mu}. \tag{5.18}$$

For integrable directions λ (e.g. $\lambda = \Delta$ for the XXZ model) and $L > L^*$, where the AGP norm has exponential scaling, the norm becomes

$$||\mathcal{A}_\lambda||^2 \sim Ce^{\beta(L-L^*)}, \tag{5.19}$$

where C roughly is the value of the unperturbed AGP norm at L^*. Recall that we observed a scaling of the critical perturbation strength like $\varepsilon_d \sim e^{-\alpha L^*}$, such that one finds

$$|f_\lambda(\mu)|^2 \sim C\mu e^{\beta(L-L^*)} \sim C\varepsilon_d^\eta e^{\kappa L}, \tag{5.20}$$

where $\eta = \beta/\alpha$, and $\kappa = \beta - \log(2)$, and we have neglected all polynomial factors in system size. For the XXZ model, the exponents are $\eta \approx 1.6$ and $\kappa \approx 0.85 \log(2)$ (see caption of Fig. 5·3). Because $|f_\lambda(\omega)|^2$ is the Fourier transform of the two-point correlation function of $\partial_\lambda H$ (see (5.8)), as $\omega \to 0$ it is proportional to the relaxation time of the system. Combining

these considerations, we see that for the XXZ model we have

$$\tau \sim \varepsilon_d^{\eta} e^{\kappa L}, \tag{5.21}$$

with both κ and η of $O(1)$. Similarly, for the Ising model, $\tau \sim h_z^{\eta} e^{\kappa L}$ where $\eta \approx 1.8$ and $\kappa \approx 1.28 \log(2)$ (see caption of Fig. 5·3). We see that the relaxation time increases exponentially with the system size. For large system sizes it can saturate at some L-independent value, which should diverge as $\varepsilon_d \to 0$. This would reflect the crossover of the scaling of the AGP norm to the ETH result: $||A_\lambda||^2 \propto \exp[S(L)] = \exp[\log(2)L]$. While this scenario seems likely, we do not see any signatures for such a crossover within our numerics and thus cannot rule out more exotic scenarios for the behavior of the relaxation time with the system size. Moreover, at intermediate system sizes accessible to our numerics, we see an extremely stable exponential scaling of the AGP norm (and hence of the relaxation time), with the exponent β independent of the strength of the integrability-breaking perturbation as long as it is sufficiently small. Interestingly, in a follow up work (Villazon et al., 2020) a similar exponential scaling of the AGP norm with $\beta \approx 2 \log(2)$ was observed in a disordered central spin model even in the absence of any small parameters, i.e. at large integrability-breaking perturbations. We note that in all the systems analyzed so far in this regime, β saturates near the maximum allowed value $2 \log(2)$, within numerical precision. From the point of view of operator spreading, this value is very reminiscent to the $2 \log(2)$ scaling of the operator entanglement entropy in maximally chaotic dual-unitary models (Bertini et al., 2020). Whether it is a simple coincidence or there is a deeper connection remains to be understood.

To illustrate these general considerations about the relaxation times we extracted the function $|f_\lambda(\omega)|^2$ directly. Usually it is very difficult to do so at exponentially small frequencies of interest, since there are very few eigenstates involved, hence leading to large fluctuations. Here we computed $|f_\lambda(\omega)|^2$ by replacing all the delta-functions in Eq. (5.8)

with Lorentzians of width μ. In all the figures $\mu = L2^{-L}$, consistent with the AGP regularization. The total spectral weight was subsequently computed on a logarithmically spaced grid. All the figures show the average spectral weight in each bin.
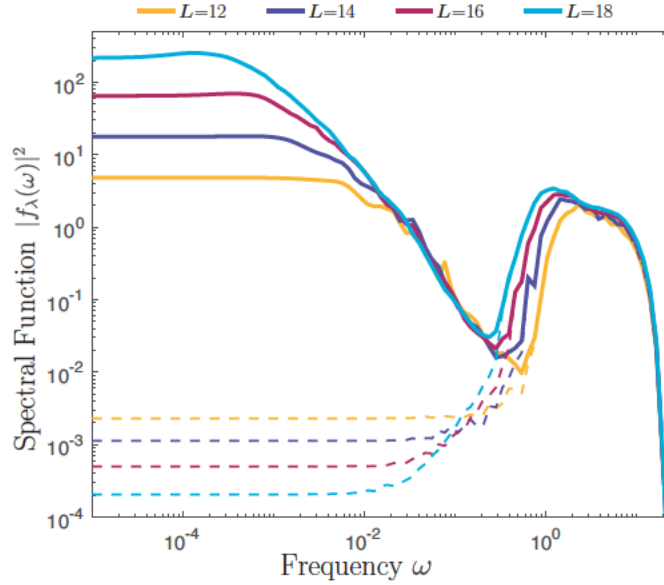
Figure 5·6: The spectral weight for the integrable perturbation. The spectral weight $|f_\lambda(\omega)|^2$ for the integrable perturbation $\lambda = \Delta$ in the XXZ model at small integrability breaking perturbation $\varepsilon_d = 0.05$ (solid lines) and at the integrable point $\varepsilon_d = 0$ (dashed lines). The remaining parameters are the same as in Fig. 5·3.

In Fig. 5·6 we show the extracted spectral weight $|f_\lambda(\omega)|^2$ for the XXZ model with $\lambda = \Delta$ for a small integrability breaking perturbation $\varepsilon_d = 0.05$ (solid lines) and exactly at the integrable point $\varepsilon_d = 0$ for four different system sizes $L = 12, 14, 16, 18$. As predicted from the AGP scaling, there is a clear exponentially growing spectral weight at small frequencies with an exponentially shrinking frequency range, where it plateaus. In the integrable regime, conversely $|f_\lambda(\omega)|^2$ is exponentially decreasing with the system size, approaching zero in the thermodynamic limit.

To contrast this behavior of the spectral function with the other two regimes where the AGP norm shows exponential scaling with $\beta = \log(2)$, in Fig. 5·7 we show $|f_\lambda(\omega)|^2$ in
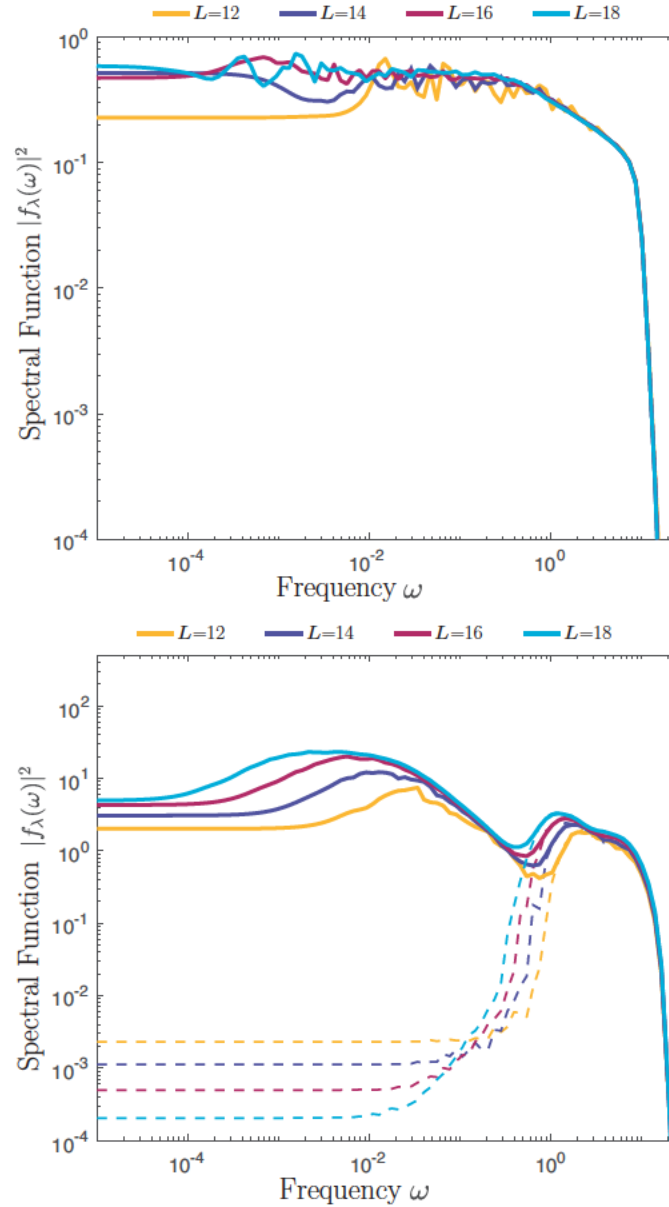
Figure 5·7: The spectral weights for the non-integrable perturbation. The spectral weight $|f_\lambda(\omega)|^2$ for the non-integrable perturbation $\lambda = \varepsilon_d$ in the XXZ model at the integrable point $\varepsilon_d = 0$ (top) and for the perturbation $\lambda = \Delta$ at the strongly non-integrable point, i.e. in the ETH regime, $\varepsilon_d = 0.5$ (bottom). The dashed lines in the bottom plot are the result at the integrable point $\varepsilon_d = 0$, showing the high frequency behavior remains unmodified even at these large petrubation strengths. The remaining parameters are the same as in Fig. 5·6.

such regimes. The top plot shows the $|f_\lambda(\omega)|^2$ for the nonintegrable perturbation $\lambda = \varepsilon_d$ at the integrable point of the XXZ model $\varepsilon_d = 0$. While the bottom plot corresponds to the perturbation $\lambda = \Delta$ at the strongly nonintegrable point $\varepsilon_d = 0.5$ where the system satisfies ETH (Gubin and F. Santos, 2012; Brenes et al., 2020b).

5.6 Distinguishing between integrable and ETH regimes

The AGP clearly depends on both the Hamiltonian H and the direction along which it is deformed, i.e. $\partial_\lambda H$. In the previous sections, we argued that generic perturbations in chaotic systems lead to an AGP norm scaling exponentially with system size, whereas in integrable models integrability-preserving perturbations lead to an AGP norm scaling polynomially. This scaling is directly reflected in the relaxation times of $\partial_\lambda H$ through its probing of the zero-frequency limit of $|f_\lambda(\omega)|^2$. However, in specific cases, polynomial scaling of the gauge potential can also be observed in chaotic systems.

In particular, there is a special class of operators which can be represented as $K = i[H, B]$, where B is a local operator or a sum of local operators. A current can, e.g., be represented in this way as $B = \sum_i i n_i$, where n_i is the conserved charge; $n_i = \sigma_z^i$ for the XXZ model. For such operators $\mathcal{A}_\lambda = B$ by construction, and the AGP will have a polynomial norm irrespective of whether the system is integrable or chaotic. For such operators $|f_\lambda(\omega)|^2$ must also vanish at $\omega \to 0$, consistent with recent numerical results (Brenes et al., 2020b). On a related note, see (Dymarsky and Liu, 2019). Physically, this non-divergence of the AGP, even in the chaotic systems satisfying ETH, simply follows from the fact that deforming the Hamiltonian with the operator K is a symmetry transformation, which does not change the spectrum of the Hamiltonian, but simply transforms the eigenstates with the unitary operator $U = \exp(-i\lambda B)$. When checking for quantum chaos, such deformations can be explicitly excluded when probing the scaling of the gauge potential.

While the existence of nontrivial deformations with polynomial scaling of the AGP

norm is an indicator of integrability, generic integrability-breaking perturbations give rise to exponential scaling, in which case the specific dependence on μ offers further information. Note that this also implies the existence of a family of integrable models, excluding more exotic 'isolated' integrable systems where every possible perturbation breaks integrability.

In the previous section, the scaling of the AGP norm was the same as one would expect from ETH, even though at $\varepsilon_d = 0$ the system is integrable and ETH is clearly violated. The non ETH-behavior can be seen,e.g., in large eigenstate-to-eigenstate fluctuations of the expectation value of $\sigma^z_{\lceil (L+1)/2 \rceil}$ (Brenes et al., 2020a). For this perturbation the scaling of the AGP with the system size simply tells us that $|f_\lambda(\omega)|^2$, which remains well-defined in such models, saturates to a nonzero constant at small ω, as confirmed directly in the previous section. Similar to the usual matrix elements of observables, the information about the integrability of the system is now contained in the statistical properties of the AGP norm.

More specifically, for random matrix ensembles the statistical properties of the fidelity susceptibility (equivalent to the contributions to the AGP norm for individual eigenstates) were analyzed in Ref. (Sierant et al., 2019), where the distribution for different eigenstates is considered. The fidelity susceptibility $z_{n,\lambda}$ of an eigenstate $|n(\lambda)\rangle$ is equivalent to

$$z_{n,\lambda} \equiv \frac{1}{\mathcal{D}} \langle n|\mathcal{A}_\lambda^2|n\rangle_c \equiv \frac{1}{\mathcal{D}} \sum_{m\neq n} |\langle n|\mathcal{A}_\lambda|m\rangle|^2, \tag{5.22}$$

such that $||\mathcal{A}_\lambda||^2 = \sum_n z_{n,\lambda}$.

Let us briefly present a simple derivation of the tail of this distribution and then contrast the AGP distribution for integrable and ETH regimes. The tail of this distribution for typical (random) perturbations will be dominated by contributions from neighbouring energy levels, such that its distribution will be inheriting its properties from the level spacing distribution.

Recall that the exact AGP norm with $\mu = 0$ is given by Eqs. (5.2) and (5.3). For a

typical perturbation we can replace the numerator of Eq. (5.2) with a random matrix such that typical matrix elements are of order $1/\sqrt{\mathcal{D}}$ (see (5.9)). The tail of the distribution for large $z_{n,\lambda}$ is dominated by nearby energy levels and we can approximate

$$z_{n,\lambda} \approx \frac{C}{s_n^2}, \tag{5.23}$$

where s_n is the level spacing $E_{n+1} - E_n$ now normalized by the Hilbert space dimension (such that the mean value of s is unity) and C is an unimportant constant, which we can set to one. The scaling of the probability distribution at large z_λ follows as

$$\Pr(z_\lambda = x) \sim \frac{1}{x^{3/2}} P\left(\frac{1}{\sqrt{x}}\right), \tag{5.24}$$

where $P(s)$ is the normalized nearest-neighbour level spacing distribution.

For integrable systems there is no level repulsion, $P(s \to 0) \neq 0$, and we have (to dominant order)

$$\Pr(z_\lambda = x) \propto x^{-3/2}, \tag{5.25}$$

for $x \gg 1$. Note that, as a consequence of this fat tail, the mean AGP diverges without regularization. The regularization with μ in the norm of the AGP effectively introduces a cutoff to the energy denominator at the rescaled cutoff $\bar{\mu} = \mu \mathcal{D}$. Assuming that the AGP norm is dominated by the contributions $z_{n,\lambda}$ for which the derived scaling holds, we can say that the average fidelity susceptibility is given by $\langle z_\lambda \rangle \propto 1/\bar{\mu}$, and hence $||\mathcal{A}_\lambda||^2 = \mathcal{D}\langle z_\lambda \rangle \sim \mathcal{D}/\bar{\mu}$. This agrees with the observed scaling shown in Fig. 5·5. On the other hand, chaotic systems satisfying ETH exhibit level repulsion and $P(s) \approx s^\beta$, resulting in $\Pr(z_\lambda = x) \propto x^{-(3+\beta)/2}$ at large values of x. For the considered Ising and XXZ model, the relevant random matrix ensemble is Gaussian orthogonal ensemble (GOE), for which $\beta = 1$ and

$$\Pr(z_\lambda = x) \propto x^{-2}. \tag{5.26}$$

In contrast to the integrable model, the mean $\langle z_\lambda \rangle \sim -\log(\bar{\mu}^2)$ diverges only logarithmically with the cutoff. These simple scaling arguments agree very well with numerical observations shown in Fig. 5·8.
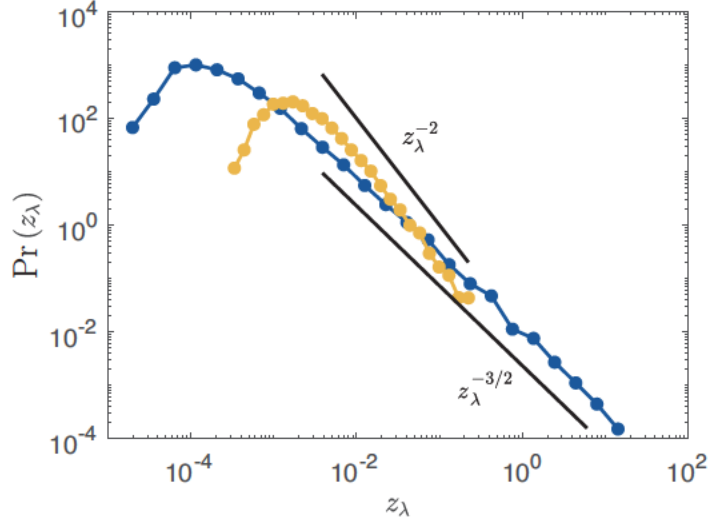
Figure 5·8: AGP norm distribution. Distribution of the eigenstate contributions z_λ to the rescaled AGP norm (see Eq. (5.23)) for the XXZ model with $L = 16$ spins. The two curves describe the results for the non-integrable perturbation $\lambda = \varepsilon_d$ at the integrable point $\varepsilon_d = 0$ (blue) and for the perturbation $\lambda = \Delta$ at the strongly non-integrable point $\varepsilon_d = 0.5$ (yellow). Black lines show the expected scalings $z_\lambda^{-3/2}$ and z_λ^{-2} for the integrable and non-integrable model respectively.

From this analysis, we can conclude that choosing a fixed $\mu \sim 1/\mathcal{D}$ leads to the same scaling of the AGP norm with the Hilbert space dimension for the integrable model with a chaotic deformation λ and for the ergodic ETH model. However, these two limits can still be distinguished by either the different scaling of the AGP norm with the cutoff μ or, equivalently, by the presence of an exponential-in-system-size difference between the typical and the average contributions of individual states to the AGP norm in the former (integrable) regime and the lack of such exponential difference in the latter (ETH) regime.

5.7 Conclusions

We found that the properly-regularized norm of the adiabatic gauge potential, the generator of adiabatic deformations, can serve as an extremely sensitive probe of quantum chaotic behavior. Within chaotic systems, this norm scales exponentially with system size, whereas it scales polynomially in interacting integrable systems and is approximately system-size independent in non-interacting systems for adiabatic deformations preserving integrability. For adiabatic deformations breaking integrability, exponential scaling is generally observed.

Using the present method to investigate the effects of an integrability-breaking perturbation on the XXZ and Ising chains, we found that perturbations that are exponentially small in system size suffice to induce chaotic behavior. We also found that such a small integrability-breaking term leads to anomalously slow dynamics along the integrable directions, with the relaxation time scaling exponentially with system size. Such integrability-breaking perturbations can also be detected at the integrable point, where no anomalous dynamics occur. Even though typical perturbations show exponential scaling of the regularized norm of the adiabatic gauge potential, regardless of whether the system is integrable or not, one can distinguish the two cases by their dependence on the regularization parameter or by their fluctuations.

This motivates the use of the adiabatic gauge potential, which is connected with both deformations of eigenstates and operator dynamics, as a sensitive probe into either chaotic or integrable behavior of quantum many-body systems.

Acknowledgements

Chapter 6

Conclusions

6.1 Summary of the thesis

Non-equilibrium physics encompasses such a wide array of phenomena that it covers almost everything under the sun. We chose the specific lens of adiabatic eigenstate deformations to study the non-equilibrium behavior of quantum many-body systems. In Chapter I, we began by discussing how the AGP is an interesting physical object to study due to its connections with a large range of topics, including quantum state preparation, quantum computing, and quantum chaos. In Chapter II, we derived the expression of the AGP in four different ways to emphasize the different defining characteristics of AGP and to present a (selective) historical development of the field. In Chapters III and IV, we studied the AGP in the context of shortcuts-to-adiabaticity, which is useful for reducing dissipation when the quantum transport is achieved at a fast rate. In Chapter III, we implemented a Floquet-engineered driving protocol successfully on the electronic spin of a nitrogen vacancy in diamond. In Chapter IV, we extended these driving protocols to more complex systems, such as many-body systems. Chapter V contained two main messages: i) we found a novel probe of quantum chaos that is considerably more sensitive than traditional measures such as energy level statistics and ii) using it, we uncovered a novel dynamical regime close to integrable regime which we call "maximal chaos". This dynamical regime is interesting because when the system is in this regime, the eigenstates show the maximum allowed sensitivity to perturbations and the system takes an exponentially long time to relax.

6.2 Future Work

Compared to other scientific fields such as cognitive science and social sciences, I feel it is rare to find published physics papers spending considerable time in discussing the limitations of their studies and how future work can overcome these limitations. In my experience, Physics papers often pretend to be flawless and claim they are "the greatest thing since the sliced bread". If I were to speculate on the reasons behind this phenomenon, the pressure to publish might contribute to it – we tend to publish only positive results in science, and if authors write about certain limitations, they might be worried about referees shooting down their work by suggesting that they should take additional time to fix their results before publishing them. Another factor that might contribute is the fear of being scooped by other researchers. Scientists spend a lot of time coming up with new results, and usually after they publish a paper, they have a bunch of follow-up papers lined up. Probably it's understandable that they want to protect their ideas. Lastly, it's possible that the "shut up and calculate" philosophy that a lot of physicists follow might contribute to it too. If a physicist has a good idea, traditionally no value is seen in writing about it at a conceptual level (though they do discuss it with their collaborators). Instead, they are encouraged to start doing calculations to see whether the idea holds for simple models first before taking it too seriously.

Taking a slight break from this tradition, let me discuss a few project ideas with the hope that they might be useful for a young physicist who might be looking for new ideas to explore. These ideas were not pursued further due to either lack of time or technical difficulties that I ran into.

Operator spreading of AGP In collaboration with Dries and Anatoli, we were trying to get some insight into the operator growth picture of the AGP. Inspired by operator growth works (e.g. (Khemani et al., 2018)), we expanded the AGP in terms of Pauli k-string

operators where k is the size of operators. To characterize the coefficients of the AGP's expansion, we used the Shannon entropy and the inverse participation ratio. We found that Shannon entropy is extensive in the ergodic phase, while it showed peeling off behavior when the system was in the maximal chaos regime. The project didn't give us significantly new information beyond that which was available through the AGP norm scaling. Another obstacle was that the basis chosen was implicitly non-local. For example, both $\sigma_1^y \sigma_2^x$ and $\sigma_{L-1}^y \sigma_L^x$, where L is the system size, were considered two-body operators in the basis we chose. However, if perturbation starts off at one corner and the Hamiltonian is composed of piece-wise local operators, these two operators might show up at different times in the expansion of the AGP though they are being classified as two-body operators. As a result, when we studied the spectral function of cross-correlations, we found Pauli strings of all sizes being "activated" together rather than low k-Pauli operators showing up in expansion of the AGP before high k-Pauli operators, which is what we originally expected. In other words, this project didn't succeed because we couldn't figure out a right basis into which to expand the AGP.

At the end of Chapter II, we presented the commutator expansion of the AGP. If we use the commutator expansion to compute the AGP for a non-integrable system, then we find each new commutator term produces new operators that have not been seen in lower-order commutators until it saturates all the available operators in the Hilbert space. If we could come up with a visualization technique (e.g. we could probably create a network where each node is an operator and study how various nodes get "activated" as the local perturbation operator evolves), then we might track the operator growth as local perturbation $\partial_\lambda H$ evolves in time leading to a non-local AGP operator.

AGP as a probe of chaos   In Chapter V, we studied quantum chaos in spin chains using the regularized AGP with the cutoff being exponentially small in system size. These systems have bounded Hilbert spaces. For an unbounded Hilbert space (e.g. Boson sys-

tems), our chosen cutoff will be zero and therefore, we need to study them carefully to figure out appropriate cutoff. Similarly, detecting chaos in classical systems using the AGP needs to be studied carefully as it's unclear what should be the appropriate cutoff. Also, the AGP can be studied for detecting chaos in classical systems through the expression of operator spreading (5.11) and it could be interesting to study its relationship to the classical Lyapunov exponent.

Appendix A

Appendix for Introduction to Adiabatic Gauge Potential

A.1 Linear recurrence coupled equations

We have a set of three coupled linear recurrence difference equations:

$$\begin{aligned}
a_{2n+1} &= \alpha^2 a_{2n-1} + b_{2n-2} + c_{2n-2} \\
b_{2n} &= \delta_1 a_{2n-1} + \delta_2 b_{2n-2} + \delta_3 c_{2n-2} \\
c_{2n} &= \varepsilon_1 a_{2n-1} + \varepsilon_2 b_{2n-2} + \varepsilon_3 c_{2n-2}
\end{aligned} \qquad , \forall n > 0 \tag{A.1}$$

where $a_n = \{a_1, a_3, \ldots\}$, $b_n = \{b_0, b_2, \ldots\}$ and $c_n = \{c_0, c_2, \ldots\}$.

We will solve this using generating function approach. We define three functions:

$$A(z) = \sum_{n=0}^{\infty} a_{2n+1} z^{2n+1} \tag{A.2}$$

$$B(z) = \sum_{n=0}^{\infty} b_{2n} z^{2n} \tag{A.3}$$

$$C(z) = \sum_{n=0}^{\infty} c_{2n} z^{2n} \tag{A.4}$$

Importantly, we note that:

$$A_\lambda = \lim_{\mu \to 0} \frac{-i\hbar}{\mu} \sum_{n=0}^{\infty} (-1)^n \frac{a_{2n+1}}{\mu^{2n+1}}$$

$$= \lim_{\mu \to 0} \frac{-\hbar}{\mu} \sum_{n=0}^{\infty} a_{2n+1} \frac{i^{2n+1}}{\mu^{2n+1}}$$

$$= \lim_{\mu \to 0} \frac{-\hbar}{\mu} A\left(z = \frac{i}{\mu}\right)$$

Now we expect $A\left(z = \frac{i}{\mu}\right) = \mu f(z = \frac{i}{\mu})$ such that $\lim_{\mu \to 0} f(z = \frac{i}{\mu})$ is finite and non-zero.

Using this, we get from one equation:

$$a_{2n+1} z^{2n+1} = \alpha^2 a_{2n-1} z^{2n+1} + b_{2n-2} z^{2n+1} + c_{2n-2} z^{2n+1} \tag{A.5}$$

$$\sum_{n=1}^{\infty} a_{2n+1} z^{2n+1} = \alpha^2 \sum_{n=1}^{\infty} a_{2n-1} z^{2n+1} + \sum_{n=1}^{\infty} b_{2n-2} z^{2n+1} + \sum_{n=1}^{\infty} c_{2n-2} z^{2n+1} \tag{A.6}$$

$$A(z) - a_1 z = \alpha^2 z^2 A(z) + z^3 B(z) + z^3 C(z) \tag{A.7}$$

$$A(z)(1 - \alpha^2 z^2) = a_1 z + z^3 B(z) + z^3 C(z) \tag{A.8}$$

Hence, we get :

$$\boxed{A(z) = \beta(z)(a_1 + z^2 B(z) + z^2 C(z))} \tag{A.9}$$

where $\beta(z) = z/(1 - \alpha^2 z^2)$

Similarly, from the second equation we get:

$$b_{2n} z^{2n} = \delta_1 a_{2n-1} z^{2n} + \delta_2 b_{2n-2} z^{2n} + \delta_3 c_{2n-2} z^{2n} \tag{A.10}$$

$$\sum_{n=1}^{\infty} b_{2n} z^{2n} = \delta_1 \sum_{n=1}^{\infty} a_{2n-1} z^{2n} + \delta_2 \sum_{n=1}^{\infty} b_{2n-2} z^{2n} + \delta_3 \sum_{n=1}^{\infty} c_{2n-2} z^{2n} \tag{A.11}$$

$$B(z) - b_0 = \delta_1 z A(z) + \delta_2 z^2 B(z) + \delta_3 z^2 C(z) \tag{A.12}$$

$$B(z)(1 - \delta_2 z^2) = b_0 + \delta_1 z A(z) + \delta_3 z^2 C(z) \tag{A.13}$$

Finally, we find from third equation:

$$C(z)(1 - \varepsilon_3 z^2) = c_0 + \varepsilon_1 z A(z) + \varepsilon_2 z^2 B(z) \tag{A.14}$$

Using the value of $A(z)$ we get:

$$B(z)(1 - \delta_2 z^2) = b_0 + \delta_3 z^2 C(z) + \delta_1 z \beta(z)(a_1 + z^2 B(z) + z^2 C(z))$$

$$B(z)(1 - \delta_2 z^2 - \delta_1 z^3 \beta(z)) = b_0 + \delta_3 z^2 C(z) + \delta_1 z \beta(z)(a_1 + z^2 C(z))$$

$$B(z)(1 - \delta_2 z^2 - \delta_1 z^3 \beta(z)) = b_0 + \delta_1 z \beta(z) a_1 + \delta_3 z^2 C(z) + \delta_1 \beta(z) z^3 C(z)$$

$$B(z)(1 - \delta_2 z^2 - \delta_1 z^3 \beta(z)) = b_0 + \delta_1 z \beta(z) a_1 + (\delta_3 + \delta_1 z \beta(z)) z^2 C(z)$$

$$B(z) = \tau(z)(\omega_0 + \omega_1 z^2 C(z))$$

where $\tau(z) = 1/(1 - \delta_2 z^2 - \delta_1 z^3 \beta(z))$, $\omega_0 = b_0 + \delta_1 z \beta(z) a_1$ and $\omega_1 = \delta_3 + \delta_1 z \beta(z)$.

Similarly, we get for $C(z)$:

$$C(z)(1 - \varepsilon_3 z^2) = c_0 + \varepsilon_2 z^3 B(z) + \varepsilon_1 z A(z)$$

$$C(z)(1 - \varepsilon_3 z^2) = c_0 + \varepsilon_2 z^3 B(z) + \varepsilon_1 z \beta(z)(a_1 + z^2 B(z) + z^2 C(z))$$

$$C(z)(1 - \varepsilon_3 z^2 - \varepsilon_1 z^3 \beta(z)) = c_0 + \varepsilon_1 z \beta(z) a_1 + \varepsilon_2 z^3 B(z) + \varepsilon_1 \beta(z) z^3 B(z)$$

$$C(z)(1 - \varepsilon_3 z^2 - \varepsilon_1 z^3 \beta(z)) = c_0 + \varepsilon_1 z \beta(z) a_1 + (\varepsilon_2 + \varepsilon_1 z \beta(z)) z^2 B(z)$$

$$C(z)(1 - \varepsilon_3 z^2 - \varepsilon_1 z^3 \beta(z)) = \theta_0 + \theta_1 z^2 B(z)$$

where $\theta_0 = c_0 + \varepsilon_1 z \beta(z) a_1$ and $\theta_1 = \varepsilon_2 + \varepsilon_1 z \beta(z)$

Now, we will use the fact that $B(z) = \tau(z)(\omega_0 + \omega_1 z^2 C(z))$ to find out value of $C(z)$:

$$C(z)(1 - \varepsilon_3 z^2 - \varepsilon_1 z^3 \beta(z)) = \theta_0 + \theta_1 z^2 B(z)$$

$$C(z)(1 - \varepsilon_3 z^2 - \varepsilon_1 z^3 \beta(z)) = \theta_0 + \theta_1 z^2 \tau(z)(\omega_0 + \omega_1 z^2 C(z))$$

$$C(z)(1 - \varepsilon_3 z^2 - \varepsilon_1 z^3 \beta(z)) = \theta_0 + \theta_1 \omega_0 z^2 \tau(z) + \theta_1 \omega_1 z^4 \tau(z) C(z)$$

$$C(z)(1 - \varepsilon_3 z^2 - \varepsilon_1 z^3 \beta(z) - \theta_1 \omega_1 z^4 \tau(z)) = \theta_0 + \theta_1 \omega_0 z^2 \tau(z)$$

$$C(z) = \eta(z)(\theta_0 + \theta_1 \omega_0 z^2 \tau(z))$$

where $\eta(z) = 1/(1 - \varepsilon_3 z^2 - \varepsilon_1 z^3 \beta(z) - \theta_1 \omega_1 z^4 \tau(z))$.

Hence,

$$\boxed{C(z) = \eta(z)(\theta_0 + \omega_0 \theta_1 z^2 \tau(z))} \tag{A.15}$$

Hence, the value of $B(z)$ is :

$$B(z) = \tau(z)(\omega_0 + \omega_1 z^2 C(z))$$

$$= \omega_0 \tau(z) + \omega_1 z^2 \tau(z) \eta(z)(\theta_0 + \theta_1 z^2 \tau(z) \omega_0)$$

Hence,

$$\boxed{B(z) = \omega_0 \tau(z) + \theta_0 \omega_1 z^2 \tau(z) \eta(z) + \omega_0 \omega_1 \theta_1 z^4 \eta(z) \tau(z)^2} \tag{A.16}$$

For $\lim z \to \infty$, we get

$$\beta(z) = z/(1 - \alpha^2 z^2) \simeq -\frac{1}{\alpha^2 z}$$

$$\omega_0 = b_0 + \delta_1 z \beta(z) a_1 \simeq b_0 - \frac{\delta_1 a_1}{\alpha^2}$$

$$\omega_1 = \delta_3 + \delta_1 z \beta(z) \simeq \delta_3 - \frac{\delta_1}{\alpha^2}$$

$$\theta_0 = c_0 + \varepsilon_1 z \beta(z) a_1 \simeq \left(c_0 - \frac{\varepsilon_1 a_1}{\alpha^2} \right)$$

$$\theta_1 = \varepsilon_2 + \varepsilon_1 z \beta(z) \simeq \varepsilon_2 - \frac{\varepsilon_1}{\alpha^2}$$

We note that ω_0 depend on b_0 and θ_0 depend on c_0.

Now, I will figure out $\tau(z)$:

$$\tau(z) = 1/(1 - \delta_2 z^2 - \delta_1 z^3 \beta(z))$$

$$\simeq \frac{1}{1 - \delta_2 z^2 + \delta_1 z^2/\alpha^2}$$

$$\simeq \frac{1}{(\delta_1/\alpha^2 - \delta_2) z^2}$$

$$\simeq \frac{\alpha^2}{(\delta_1 - \alpha^2 \delta_2) z^2} = \frac{\theta_2}{z^2}$$

where $\theta_2 = \dfrac{\alpha^2}{\delta_1 - \alpha^2 \delta_2}$ Now, I will figure out $\eta(z)$:

$$\eta(z) = \frac{1}{1 - \varepsilon_3 z^2 - \varepsilon_1 z^3 \beta(z) - \theta_1 \omega_1 z^4 \tau(z)}$$

$$\simeq \frac{1}{1 - \varepsilon_3 z^2 + \varepsilon_1 z^2/\alpha^2 - \theta_1 \omega_1 z^4 \tau(z)}$$

$$\simeq \frac{1}{1 - \varepsilon_3 z^2 + \varepsilon_1 z^2/\alpha^2 - \frac{\theta_1 \omega_1 \alpha^2}{\delta_1 - \alpha^2 \delta_2} z^2}$$

$$\simeq \frac{1}{-\varepsilon_3 + \varepsilon_1/\alpha^2 - \frac{\theta_1 \omega_1 \alpha^2}{\delta_1 - \alpha^2 \delta_2}} \frac{1}{z^2} = \frac{\theta_3}{z^2}$$

where $\theta_3 = \dfrac{1}{-\varepsilon_3 + \varepsilon_1/\alpha^2 - \frac{\theta_1 \omega_1 \alpha^2}{\delta_1 - \alpha^2 \delta_2}}$.

Hence, we get for $C(z)$:

$$\begin{aligned}
C(z) &= \eta(z)(\theta_0 + \omega_0\theta_1 z^2\tau(z)) \\
&= \theta_0\eta(z) + \omega_0\theta_1 z^2\tau(z)\eta(z) \\
&= \theta_0\frac{\theta_3}{z^2} + \omega_0\theta_1 z^2\frac{\theta_2}{z^2}\frac{\theta_3}{z^2} \\
&= (\theta_0\theta_3 + \omega_0\theta_1\theta_2\theta_3)\frac{1}{z^2}
\end{aligned}$$

Hence, we get for $B(z)$:

$$\begin{aligned}
B(z) &= \omega_0\tau(z) + \theta_0\omega_1 z^2\tau(z)\eta(z) + \omega_0\omega_1\theta_1 z^4\eta(z)\tau(z)^2 \\
&= \omega_0\frac{\theta_2}{z^2} + \theta_0\omega_1 z^2\frac{\theta_2}{z^2}\eta(z) + \omega_0\omega_1\theta_1 z^4\eta(z)\frac{\theta_2^2}{z^4} \\
&= \omega_0\frac{\theta_2}{z^2} + \omega_1\theta_0\theta_2\eta(z) + \omega_0\omega_1\theta_1\theta_2^2\eta(z) \\
&= (\omega_0\theta_2 + \omega_1\theta_0\theta_2\theta_3 + \omega_0\omega_1\theta_1\theta_2^2\theta_3)\frac{1}{z^2}
\end{aligned}$$

Finally, we get for $A(z)$:

$$\begin{aligned}
A(z) &= \beta(z)(a_1 + z^2 B(z) + z^2 C(z)) \\
&\simeq -\frac{1}{\alpha^2 z}(a_1 + z^2 B(z) + z^2 C(z)) \\
&\simeq -\frac{1}{\alpha^2 z}(a_1 + \omega_0\theta_2 + \omega_1\theta_0\theta_2\theta_3 + \omega_0\omega_1\theta_1\theta_2^2\theta_3 + \theta_0\theta_3 + \omega_0\theta_1\theta_2\theta_3) \\
&= -\frac{1}{\alpha^2 z}(a_1 + \omega_0\theta_2 + \theta_0\theta_3 + (\omega_1\theta_0 + \omega_0\theta_1)\theta_2\theta_3 + \omega_0\omega_1\theta_1\theta_2^2\theta_3) \\
&= -\frac{1}{\alpha^2 z}\left(a_1 + \theta_2 b_0 - \frac{\delta_1\theta_2}{\alpha^2}a_1 + \theta_3 c_0 - \frac{\varepsilon_1\theta_3}{\alpha^2}a_1 + \omega_1\theta_2\theta_3 c_0 - \frac{\varepsilon_1\omega_1\theta_2\theta_3}{\alpha^2}a_1 \right. \\
&\quad \left. + \left(b_0 - \frac{\delta_1 a_1}{\alpha^2}\right)(\theta_1\theta_2\theta_3 + \omega_1\theta_1\theta_2^2\theta_3)\right)
\end{aligned}$$

We are getting closer to final expression by clubbing together coefficients of a_1, b_0, c_0:

$$
\begin{aligned}
A(z) &= -\frac{1}{\alpha^2 z}\left(a_1 - \frac{\delta_1\theta_2}{\alpha^2}a_1 - \frac{\varepsilon_1\theta_3}{\alpha^2}a_1 - \frac{\varepsilon_1\omega_1\theta_2\theta_3}{\alpha^2}a_1 + \theta_2 b_0 \right. \\
&\quad \left. + \left(b_0 - \frac{\delta_1 a_1}{\alpha^2}\right)(\theta_1\theta_2\theta_3 + \omega_1\theta_1\theta_2^2\theta_3) + \theta_3 c_0 + \omega_1\theta_2\theta_3 c_0\right) \\
&= -\frac{1}{\alpha^2 z}\left(\left(1 - \frac{\delta_1\theta_2}{\alpha^2} - \frac{\varepsilon_1\theta_3}{\alpha^2} - \frac{\varepsilon_1\omega_1\theta_2\theta_3}{\alpha^2} - \frac{\delta_1}{\alpha^2}(\theta_1\theta_2\theta_3 + \omega_1\theta_1\theta_2^2\theta_3)\right)a_1\right. \\
&\quad + (1 + \theta_1\theta_3(1 + \omega_1\theta_2))\theta_2 b_0 \\
&\quad \left. + (1 + \omega_1\theta_2)\theta_3 c_0\right) \\
&= -\frac{1}{\alpha^2 z}f(z)
\end{aligned}
$$

where

$$
\begin{aligned}
f(z) &= (1 - \frac{\delta_1\theta_2}{\alpha^2} - \frac{\varepsilon_1\theta_3}{\alpha^2} - \frac{\varepsilon_1\omega_1\theta_2\theta_3}{\alpha^2} \\
&\quad - \frac{\delta_1}{\alpha^2}(\theta_1\theta_2\theta_3 + \omega_1\theta_1\theta_2^2\theta_3))a_1 \\
&\quad + (1 + \theta_1\theta_3(1 + \omega_1\theta_2))\theta_2 b_0 + (1 + \omega_1\theta_2)\theta_3 c_0.
\end{aligned}
$$

We note that $f(z)$ is a constant function in z and therefore, this is the required function f we were looking for.

At the end, we note that:

$$
\begin{aligned}
A_\lambda &= \lim_{\mu \to 0} \frac{-\hbar}{\mu}A\left(z = \frac{1}{-i\mu}\right) \\
&= \lim_{\mu \to 0} \frac{-\hbar}{\mu}A\big|_{z^{-1}=-i\mu} \\
&= \lim_{\mu \to 0} \frac{\hbar}{\mu}\frac{1}{\alpha^2 z}f(z)\big|_{z^{-1}=-i\mu} \\
&= \frac{-i\hbar}{\alpha^2}f(z)
\end{aligned}
$$

We summarize here that

$$\frac{-i\hbar}{\alpha^2} f(z) = \alpha^* a_1 + \beta^* b_0 + \delta^* c_0 \tag{A.17}$$

where

$$\alpha^* = \frac{-i\hbar}{\alpha^2} \left(1 - \frac{\delta_1 \theta_2}{\alpha^2} - \frac{1}{\alpha^2} \theta_3 (1 + \omega_1 \theta_2)(\epsilon_1 + \delta_1 \theta_1 \theta_2) \right) \tag{A.18}$$

$$\beta^* = \frac{-i\hbar}{\alpha^2} (1 + \theta_1 \theta_3 (1 + \omega_1 \theta_2)) \theta_2 \tag{A.19}$$

$$\delta^* = \frac{-i\hbar}{\alpha^2} (1 + \omega_1 \theta_2) \theta_3 \tag{A.20}$$

We find that:

$$(1 + \omega_1 \theta_2) \theta_3 = \alpha^2 \frac{\delta_3 - \delta_2}{\det M} \tag{A.21}$$

where

$$\det M = \delta_3 \left(\epsilon_1 - \alpha^2 \epsilon_2 \right) + \delta_2 \left(\alpha^2 \epsilon_3 - \epsilon_1 \right) + \delta_1 \left(\epsilon_2 - \epsilon_3 \right) \tag{A.22}$$

Hence, after all of this, we get:

$$\boxed{\begin{aligned} \alpha^* &= -i\hbar \frac{(\delta_2 \epsilon_3 - \delta_3 \epsilon_2)}{\det M} \\ \beta^* &= -i\hbar \frac{(\epsilon_2 - \epsilon_3)}{\det M} \\ \delta^* &= -i\hbar \frac{(\delta_3 - \delta_2)}{\det M} \end{aligned}} \tag{A.23}$$

A.2 Properties of n-commutators

In this section, we would be proving some results of n-commutators $C^{(n)}$.

Theorem 1. $C^{(n)} = [H, C^{(n-1)}], \forall n > 0$ where $C^{(0)} = \partial_\lambda H$ and $C^{(1)} = [H, \partial_\lambda H]$

Proof. We define the first two terms as $C^{(0)} = \partial_\lambda H$ and $C^{(1)} = [H, \partial_\lambda H]$.

Now, $C^{(2)} = [H, [H, \partial_\lambda H]] = [H, C^{(1)}]$. Similarly, $C^{(3)} = [H, C^{(2)}]$. Hence, we can claim using induction argument:

$$C^{(n)} = [H, C^{(n-1)}] \tag{A.24}$$

$\square$

Theorem 2. *If* $C^{(3)} = \alpha^2 C^{(1)} + T$ *, then* $C^{(2n+1)} = \alpha^{2n} C^{(1)} + \alpha^{2n-2} \sum_{q=0}^{n-1} \alpha^{-2q} C_T^{(2q)}, \ \forall n > 0,$ *where* T *is an operator,* $C_T^{(0)} = T$ *,* $C_T^{(2)} = [H, [H, T]]$ *and so on.*

Proof.

$$C^{(5)} = [H, [H, C^{(3)}]] \tag{A.25}$$
$$= [H, [H, \alpha^2 C^{(1)} + T]] \tag{A.26}$$
$$= \alpha^2 C^{(3)} + [H, [H, T]] \tag{A.27}$$
$$= \alpha^4 C^{(1)} + \alpha^2 T + C_T^{(2)} \tag{A.28}$$

$$C^{(7)} = [H, [H, C^{(5)}]] \tag{A.29}$$
$$= [H, [H, \alpha^4 C^{(1)} + \alpha^2 T + C_T^{(2)}]] \tag{A.30}$$
$$= \alpha^6 C^{(1)} + \alpha^4 T + \alpha^2 C_T^{(2)} + C_T^{(4)} \tag{A.31}$$

Hence, in general, we can claim that

$$C^{(2n+1)} = \alpha^{2n} C^{(1)} + \alpha^{2n-2} T + \alpha^{2n-4} C_T^{(2)} + \ldots + C_T^{(2n-2)}$$
$$= \alpha^{2n} C^{(1)} + \sum_{q=0}^{n-1} \alpha^{2n-2-2q} C_T^{(2q)}$$
$$= \alpha^{2n} C^{(1)} + \alpha^{2n-2} \sum_{q=0}^{n-1} \alpha^{-2q} C_T^{(2q)}$$

$\square$

If $C_T^{(2)} = \beta^2 T$, then we have a corollary result given below.

Theorem 3. *If* $C^{(3)} = \alpha^2 C^{(1)} + T$ *and* $C_T^{(2)} = \beta^2 T$ *, then* $C^{(2n+1)} = \alpha^{2n} C^{(1)} + \left(\dfrac{\alpha^{2n} - \beta^{2n}}{\alpha^2 - \beta^2} \right) T, \ \forall n > 0,$ *where* T *is a term involving some operators and* $C_T^{(2)} = [H, [H, T]]$

Proof. Since $C_T^{(2)} = \beta^2 T$, we have $C_T^{(2n)} = \beta^{2n}T$, $n > 0$. Using this, we get:

$$C^{(2n+1)} = \alpha^{2n}C^{(1)} + \alpha^{2n-2}\sum_{q=0}^{n-1}\alpha^{-2q}C_T^{(2q)}$$

$$= \alpha^{2n}C^{(1)} + \alpha^{2n-2}T\sum_{q=0}^{n-1}\left(\frac{\beta^2}{\alpha^2}\right)^q$$

$$= \alpha^{2n}C^{(1)} + \left(\frac{\alpha^{2n} - \beta^{2n}}{\alpha^2 - \beta^2}\right)T$$

$\square$

Theorem 4. *If* $C_T^{(2)} = \delta T + O$ *, then* $C_T^{(2n)} = \delta^n T + \delta^{n-1}\sum_{q=0}^{n-1}\delta^{-q}C_O^{(2q)}$*,* $\forall n > 0$*, where O is an operator,* $C_T^{(0)} = T$ *,* $C_T^{(2)} = [H,[H,T]]$ *and so on. Similarly,* $C_O^{(0)} = O$ *,* $C_O^{(2)} = [H,[H,O]]$ *and so on*

Proof.

$$C_T^{(4)} = [H,[H,C_T^{(2)}]] \tag{A.32}$$

$$= [H,[H,\delta T + O]] \tag{A.33}$$

$$= \delta C_T^{(2)} + C_O^{(2)} \tag{A.34}$$

$$= \delta^2 T + \delta O + C_O^{(2)} \tag{A.35}$$

$$C_T^{(6)} = [H,[H,C_T^{(4)}]] \tag{A.36}$$

$$= [H,[H,\delta^2 T + \delta O + C_O^{(2)}]] \tag{A.37}$$

$$= \delta^2 C_T^{(2)} + \delta C_O^{(2)} + C_O^{(4)} \tag{A.38}$$

$$= \delta^3 T + \delta^2 O + \delta C_O^{(2)} + C_O^{(4)} \tag{A.39}$$

Hence, in general, we can claim that

$$C_T^{(2n)} = \delta^n T + \delta^{n-1} O + \delta^{n-2} C_O^{(2)} + \ldots + C_O^{(2n-2)}$$

$$= \delta^n T + \sum_{q=0}^{n-1} \delta^{n-1-q} C_O^{(2q)}$$

$$= \delta^n T + \delta^{n-1} \sum_{q=0}^{n-1} \delta^{-q} C_O^{(2q)}$$

$\square$

Theorem 5. *If* $C^{(3)} = \alpha^2 C^{(1)} + T$ *, then* $C^{(2n+1)} = \alpha^2 C^{(2n-1)} + C_T^{(2n-2)}$, $\forall n > 0$, *where* T *is an operator,* $C_T^{(0)} = T$ *,* $C_T^{(2)} = [H, [H, T]]$ *and so on.*

Proof. For $n = 2$, we have

$$C^{(5)} = [H, [H, C^{(3)}]] \tag{A.40}$$

$$= [H, [H, \alpha^2 C^{(1)} + T]] \tag{A.41}$$

$$= \alpha^2 C^{(3)} + C_T^{(2)} \tag{A.42}$$

For $n = 3$, we have

$$C^{(7)} = [H, [H, C^{(5)}]] \tag{A.43}$$

$$= [H, [H, \alpha^2 C^{(3)} + C_T^{(2)}]] \tag{A.44}$$

$$= \alpha^2 C^{(5)} + C_T^{(4)} \tag{A.45}$$

Hence, in general, we can claim that

$$C^{(2n+1)} = \alpha^2 C^{(2n-1)} + C_T^{(2n-2)}$$

$\square$

Theorem 6. *If* $C_T^{(2)} = \delta T + O$ *, then* $C_T^{(2n)} = \delta C_T^{(2n-2)} + C_O^{(2n-2)}$, $\forall n > 0$, *where* O *is an operator,* $C_T^{(0)} = T$ *,* $C_T^{(2)} = [H, [H, T]]$ *and so on. Similarly,* $C_O^{(0)} = O$ *,* $C_O^{(2)} = [H, [H, O]]$ *and so on*

Proof.

$$C_T^{(4)} = [H, [H, C_T^{(2)}]] \tag{A.46}$$

$$= [H, [H, \delta T + O]] \tag{A.47}$$

$$= \delta C_T^{(2)} + C_O^{(2)} \tag{A.48}$$

$$C_T^{(6)} = [H, [H, C_T^{(4)}]] \tag{A.49}$$

$$= [H, [H, \delta C_T^{(2)} + C_O^{(2)}]] \tag{A.50}$$

$$= \delta C_T^{(4)} + C_O^{(4)} \tag{A.51}$$

Hence, in general, we can claim that

$$C_T^{(2n)} = \delta C_T^{(2n-2)} + C_O^{(2n-2)}$$

$\square$

A.3 Infinite summation method

Using theorem proved in appendix, we get

$$C^{(2n+1)} = \alpha^{2n} C^{(1)} + \alpha^{2n-2} \sum_{q=0}^{n-1} \alpha^{-2q} (C_{T_2}^{(2q)} + C_{T_3}^{(2q)})$$

This shows that for any subsequent $C^{(2n+1)}$, we won't have any *new* term apart from $C^{(1)}, T_2$ and T_3.

In previous section, we have proved that if $C_T^{(2)} = \delta T + O$, then $C_T^{(2n)} = \delta^n T + \delta^{n-1} \sum_{q=0}^{n-1} \delta^{-q} C_O^{(2q)}$. In our case, $C_{T_2}^{(2)} = \delta_2 T_2 + O$ where $O = \delta_1 C^{(1)} + \delta_3 T_3$. Now, let's compute $C_O^{(2q)}$:

$$C_O^{(2)} = \delta_1 C^{(3)} + \delta_3 C_{T_3}^{(2)}$$

$$Similarly, C_O^{(2q)} = \delta_1 C^{(2q+1)} + \delta_3 C_{T_3}^{(2q)}$$

Hence, we see that $C_{T_2}^{(2n)} = \delta_2^n T_2 + \delta_2^{n-1} \sum_{q=0}^{n-1} \delta^{-q}(\delta_1 C^{(2q+1)} + \delta_3 C_{T_3}^{(2q)})$. Similarly, $C_{T_3}^{(2n)} = \varepsilon_3^n T_3 + \varepsilon_3^{n-1} \sum_{q=0}^{n-1} \varepsilon_3^{-q}(\varepsilon_1 C^{(2q+1)} + \varepsilon_2 C_{T_2}^{(2q)})$.

We are left with a set of three coupled recurrence equations given by:

$$
\boxed{
\begin{aligned}
C^{(2n+1)} &= \alpha^{2n} C^{(1)} + \alpha^{2n-2} \sum_{q=0}^{n-1} \alpha^{-2q}(C_{T_2}^{(2q)} + C_{T_3}^{(2q)}) \\
C_{T_2}^{(2q)} &= \delta_2^q T_2 + \delta_2^{q-1} \sum_{p=0}^{q-1} \delta_2^{-p}(\delta_1 C^{(2p+1)} + \delta_3 C_{T_3}^{(2p)}) \\
C_{T_3}^{(2q)} &= \varepsilon_3^q T_3 + \varepsilon_3^{q-1} \sum_{p=0}^{q-1} \varepsilon_3^{-p}(\varepsilon_1 C^{(2p+1)} + \varepsilon_2 C_{T_2}^{(2p)})
\end{aligned}
}
\tag{A.52}
$$

Now let's concentrate on $C_{T_2}^{(2q)}$ here:

$$C_{T_2}^{(2q)} = \delta_2^q T_2 + \delta_2^{q-1} \sum_{p=0}^{q-1} \delta_2^{-p}(\delta_1 C^{(2p+1)} + \delta_3 C_{T_3}^{(2p)}) \tag{A.53}$$

$$= \delta_2^q T_2 + \delta_2^{q-1} \sum_{p=0}^{q-1} \delta_2^{-p} \delta_1 C^{(2p+1)} + \delta_2^{q-1} \sum_{p=0}^{q-1} \delta_2^{-p} \delta_3 C_{T_3}^{(2p)} \tag{A.54}$$

$$= \delta_2^q T_2 + \delta_2^{q-1} \sum_{p=0}^{q-1} \delta_2^{-p} \delta_1 C^{(2p+1)} + O \tag{A.55}$$

$$= \delta_2^q T_2 + \delta_2^{q-1} \sum_{p=0}^{q-1} \delta_2^{-p} \delta_1 (\alpha^{2p} C^{(1)} + \alpha^{2p-2} \sum_{l=0}^{p-1} \alpha^{-2l}(C_{T_2}^{(2l)} + C_{T_3}^{(2l)})) + O \tag{A.56}$$

Hence, we see that we get infinite summation expression, which seems intractable to me.

Appendix B

Appendix for FE Quantum State Manipulation in a Noisy Qubit

B.1 Derivation of FE protocol for a qubit and its generalization

We present here the derivation of the Floquet engineered driving protocol (equation (3.4)) for a qubit. It has the same form as that of the Fast-Forward Hamiltonian (equation (3.3)):

$$H_{\text{FE}} = B_z(t)\sigma_z + B_x(t)\sigma_x \tag{B.1}$$

where both B_z and B_x consist of smooth and rapidly oscillating parts.

Informed by the standard prescription of Floquet engineering, we take $B_x(t) = \lambda(t) + \omega\Omega\sin(\omega t)$, where Ω is a free parameter (Bukov et al., 2015). Next, we consider a rotating frame defined by the unitary $V = \exp(-i\sigma_x\theta(t))$ where $\theta(t) = -\Omega\cos(\omega t)$, which effectively performs a re-summation of the Magnus expansion of equation (B.1). In the rotating frame, the Hamiltonian becomes:

$$\tilde{H} = V^\dagger H V - iV^\dagger \dot{V} \tag{B.2}$$

$$= B_z(t)(\cos 2\theta\sigma_z + \sin 2\theta\sigma_y) + \lambda(t)\sigma_x, \tag{B.3}$$

This rotating frame Hamiltonian includes σ_y, allowing us to implement the counter-diabatic (CD) Hamiltonian of equation (3.2) by choosing the appropriate time dependence for $B_z(t)$.

To find an approximate form for $B_z(t)$, we average $\tilde{H}$ over a single time period $T = 2\pi/\omega$ to compute the first term of its Magnus expansion. Since the σ_y term is required

for implementing CD driving, we choose $B_z(t) = \alpha - \beta(t)\cos(\omega t)$, where α, and β are free parameters of the Floquet engineered driving protocol, so that we get non-zero contribution from the average over $B_z(t)\sin 2\theta\sigma_y$. This gives us:

$$\tilde{H}^{(0)} = \alpha\mathcal{J}_0(2\Omega)\sigma_z + \beta(t)\mathcal{J}_1(2\Omega)\sigma_y + \lambda(t)\sigma_x$$

where $\mathcal{J}_0$ and $\mathcal{J}_1$ are zero and first-order Bessel functions, and we have assumed that $\tau \gg T$ so that $\beta(t), \lambda(t)$ are approximately constant over a single period of the drive, T. This Hamiltonian is exactly the CD Hamiltonian (3.2) as long as the coefficients satisfy the constraint:

$$\beta\mathcal{J}_1(2\Omega) = \frac{1}{2}\frac{\alpha\mathcal{J}_0(2\Omega)\dot{\lambda}}{(\alpha\mathcal{J}_0(2\Omega))^2 + \lambda^2}, \tag{B.4}$$

where the gap of the effective qubit in the rotating frame is $\Delta' = \alpha\mathcal{J}_0(2\Omega)$. Note that the latter is completely arbitrary and we get a CD Hamiltonian irrespective of the value of this gap. Transforming back to the lab frame, and choosing $\alpha = \Delta$ such that the gap in lab frame remains unchanged, we arrive at our Floquet engineered driving protocol (equation (3.4)).

Additionally, to ensure that wavefunctions in both lab and rotating frames at the initial time $t = 0$ and final time $t = \tau$ are identical up to a constant phase, we require that $\Omega = m\pi$ and $\tau = nT = n/2\pi\omega$ for integers m and n. If the ground state of the Hamiltonian H_{FE} is in the x-direction at the initial and final times, then we have more freedom in our choice of Ω because the unitary $V = \exp(-i\sigma_x\theta(t))$ can only add an overall phase to the wavefunction (see appendix B.3). We exploited this in experiment to drive our fields at high frequency ω by taking a smaller Ω, which helped us by reducing the amplitude of the required fields below the saturation level of our hardware.

The previous discussion can directly be generalized to many body systems. First we note that an optimal variational single-spin counter-diabatic protocol, which can be easily

computed (Sels and Polkovnikov, 2017), can already be very efficient even in complex interacting systems (Hartmann and Lechner, 2019) . Such variational protocols can be implemented through the Floquet fast forward driving proposed here. In a more general situation one can extend our strategy in several different ways. Here we present the most direct one. Consider a generic system subject to a time-dependent Hamiltonian:

$$H(t) = H_0 + \lambda(t)H_1, \tag{B.5}$$

then a Floquet engineered fast-forward Hamiltonian has the general form

$$H_{\text{FE}} = \Omega\omega\sin\omega t H + g(t)H_1. \tag{B.6}$$

In the rotating frame defined by the unitary $V = \exp(-i\Omega H\cos\omega t)$, the Hamiltonian becomes

$$\tilde{H} = V^\dagger H_{\text{FE}} V - iV^\dagger \dot{V} = g(t)V^\dagger H_1 V. \tag{B.7}$$

Consequently, the first term in the Magnus expansion reads:

$$\tilde{H}^{(0)} = \sum_l i^l g_l \sum_{n,m} \mathcal{J}_l(\Omega(\varepsilon_n - \varepsilon_m)) \langle n|H_1|m\rangle |n\rangle \langle m|, \tag{B.8}$$

where ε_n is the eigenvalue of H associated with eigenvector $|n\rangle$, g_l is the lth component of the Fourier series of $g(t)$ and $\mathcal{J}_l$ is the lth order Bessel function of the first kind. The system remains adiabatic in the rotating frame as long as $H^{(0)}$ implements the adiabatic gauge potential, given by (Kolodrubetz et al., 2017):

$$A_\lambda = \sum_{n,m} i\frac{\langle n|H_1|m\rangle}{\varepsilon_m - \varepsilon_n} |n\rangle \langle m|. \tag{B.9}$$

In practice the number of Fourier components in $g(t)$ will be limited and the best approximation of (B.8) to the adiabatic gauge potential (B.9) can be found by considering g_l and Ω as variational parameters and using the idea developed in (Sels and Polkovnikov, 2017).

Further details on the implementation and performance of these protocols will be presented elsewhere.

B.2 Experimental design
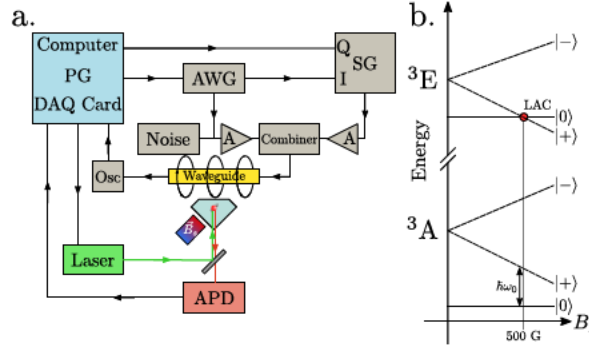
Figure B·1: Hardware and NV energy levels a. Schematic diagram of hardware setup. PG: Pulse Generator; DAQ Card: Data Acquisition card; AWG: Arbitrary Waveform Generator; SG: Signal Generator; A: Amplifier; Osc: Oscilloscope; APD: Avalanche Photodiode. Laser module includes a double pass acoustic-optic modulator (AOM). b. Energy levels of the NV center under a static magnetic field along the NV symmetry axis, taken to be the z-axis.

The diamond used in our experiments was grown by C^{12} enriched carbon vapor deposition and bombarded with N^{15} ions to produce spin-1 NV centers coupled to spin-1/2 N^{15} nuclei by the hyperfine interaction $A\vec{S}\cdot\vec{I}$. Figure B·1.a shows a schematic diagram of the hardware setup used to probe and manipulate individual NV centers. The setup is controlled by a computer which communicates with the hardware and has a pulse generator card (PG) for creating TTL trigger pulses and a data acquisition card (DAQ card) for receiving photon detection events from the avalanche photodiode (APD). We probe individual NV centers using a 532nm laser in a scanning confocal microscope setup using the APD to detect fluorescence and with an acoustic-optic modulator (AOM) to create laser pulses of 100ns and longer. A bar magnet ($\vec{B}_s$) mounted on a 5 axis translation/rotation stage is aligned with the NV center axis and the distance from the NV center is tuned to

produce the desired static field along the NV center z-axis.

To create an effective qubit, we tuned the static field $\vec{B}_s$ to the NV center excited state level anti-crossing (LAC) at approximately 500G, as shown in the energy level diagram in Figure B·1.b. At the LAC, optically pumping the NV center will polarize both the NV spin and the nuclear spin (Jacques et al., 2009). Since the nuclear spin has a much longer relaxation time than the electronic spin and we do not drive at the nuclear spin transition frequency, the nuclear spin remains in the ground state throughout the protocol and the hyperfine term becomes $-A/2S_z$, merely shifting the NV electronic spin transition frequency. Additionally, at the LAC, the NV spin states $|+1\rangle$ and $|-1\rangle$ are split by $\sim$3 GHz, allowing us to drive on resonance with the $|0\rangle \leftrightarrow |+1\rangle$ transition at $\omega_0 \approx 1.46$ GHz without driving any transitions to the $|-1\rangle$ state. Thus, we have an effective qubit consisting of the NV spin states $|0\rangle$ and $|+1\rangle$.
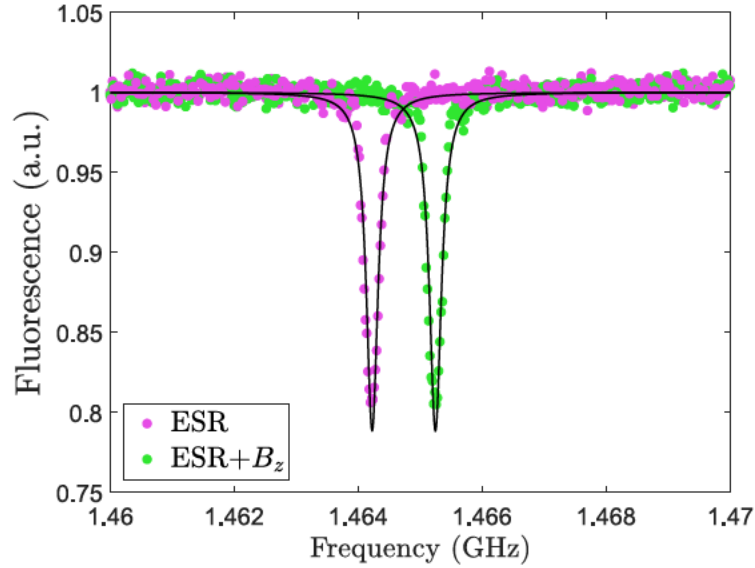
Figure B·2: ESR spectrum Measured ESR spectrum of the NV center at the LAC with an applied $B_z = 1$MHz (green data) and without B_z (purple data). Solid lines are fits to a Lorentzian line shape, $A(\omega) = 1 - \frac{c}{(\omega - \omega_0)^2 + (b/2)^2}$

We manipulate the qubit using time-dependent external magnetic fields $B_{x,y,z}$ generated

by current in a waveguide near the NV center. To generate $B_x(t)$ and $B_y(t)$, we generate voltage signals using an arbitrary waveform generator (AWG) and use them to perform I/Q modulation of a carrier signal at frequency ω_0 created by the signal generator (SG). $B_z(t)$ is also generated by an AWG, but is not modulated, and the signals are then amplified, combined, and sent to a waveguide where they generate a magnetic field at the NV center. The magnetic field generated by each of these signals has components along both the x- and z-axes of the NV center, but $B_z(t)$ has frequency components up to only $\sim 100\,\text{MHz} \ll \omega_0$, so it cannot drive transitions and has negligible effect on the x- and y-axes. Conversely, since $B_x(t)$ and $B_y(t)$ are modulated at ω_0, much faster than any other scale in the system, in the rotating frame the z-axis field they contribute rapidly averages to zero, giving the experimentally accessible Hamiltonian for the effective qubit:

$$H_{\text{lab}} = (\omega_0/2 + B_z)\sigma_z + 2(B_x \cos\omega_0 t + B_y \sin\omega_0 t)\sigma_x \qquad \text{(B.10)}$$

Since the drive amplitude and detuning are much smaller than the carrier frequency, we transform to the rotating frame defined by $\omega_0/2\sigma_z$ and invoke the rotating wave approximation to give the following Hamiltonian:

$$H_{\text{rot}} = B_z(t)\sigma_z + B_x(t)\sigma_x + B_y(t)\sigma_y \qquad \text{(B.11)}$$

This allows us to implement each protocol by choosing $B_{x,y,z}$ appropriately.

To calibrate the amplitudes of $B_{x,y}$, we set them to be constants to drive Rabi oscillations and tune the power to give the desired Rabi frequency. To calibrate B_z, we set it to be constant and perform electron spin resonance (ESR) to observe the shift in the transition frequency. In Figure B·2 we show electron spin resonance (ESR) spectra of the NV center with the static magnet $\vec{B}_s$ tuned near the LAC (purple data). In another set of data (green), we additionally apply a constant field $B_z = 1\text{MHz}$ using the electronics described above for the duration of the ESR RF pulse (4μs). The ESR spectra confirm that the N^{15} nuclear spin

is polarized because each spectra has a single peak while the spectrum for an unpolarized spin would have two peaks separated by the hyperfine interaction $A \approx 3\text{MHz}$. Additionally, we see that applying B_z results in an effective σ_z term, shifting the ESR frequency.

The experiment is then carried out by the pulse sequence in figure 3·3.a, as described in the main text. When reporting the final fidelity for each protocol, $F(\tau)$, we average the fidelity over the final 40ns of the protocol in order to account for jitter in signal generation.

B.3 Protocol imperfections

In this section we discuss potential errors in the Floquet-engineered protocol that might arise from simplifying approximations and limitations in the hardware. We show that these errors do not significantly affect the experimentally achievable protocol fidelities.
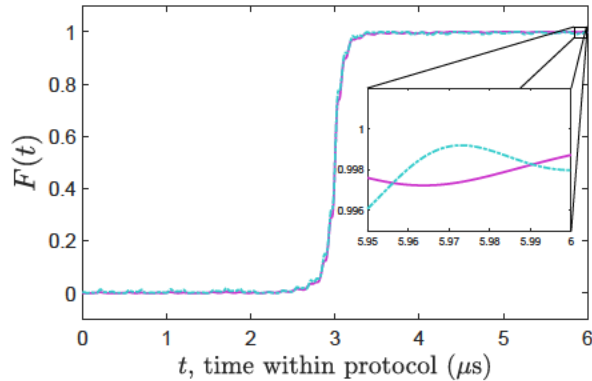
Figure B·3: Simulation comparing fidelity for different initial states
Numerically calculate fidelity within the FE protocol with the state starting along the x-axis (solid purple line) and along the true ground state of the original LZ Hamiltonian (dashed blue line). Note that on this scale the curves nearly lie on top of each other. Protocol parameters: $\Delta/2\pi = 0.1\,\text{MHz}$, $\lambda_0/2\pi = 1.5\,\text{MHz}$, $\omega/2\pi = 6\,\text{MHz}$, $\Omega = \pi/4$ and $\tau = 6\,\mu s$

As illustrated in the main text, the aim of each protocol is to bring the system from the initial state, $|-x\rangle$ to the target state, $|+x\rangle$. The Landau-Zener protocol achieves this by sweeping B_x with a constant B_z so that the ground state rotates with the net magnetic field around the y-axis from -x to +x. Since B_z is finite, this would require $B_x \to \infty$, which is

experimentally inaccessible. To approximate this, we consider protocols where $B_z/B_x \ll 1$ so that the spin pointing along -x is nearly in the initial ground state. Our experiments use $B_z/B_x = 0.1/1.5$, which gives an initial overlap of $|\langle \psi(0)|\psi_{GS}(0)\rangle| = 0.9978$. In figure B·3, we show simulations of the FE protocol with the same parameters as in Figure 3.b of the main text with the system starting in the exact ground state and along the -x-axis. The curves nearly overlap for the entire protocol and the final fidelities agree at the level of precision available in experiments (± 0.004). The oscillations in both protocols are caused by the finite Floquet driving frequency and deviations from starting in the initial ground state; these small fluctuations will be slightly different for the different initial states.
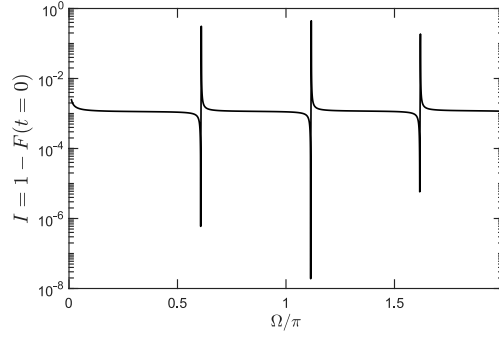
Figure B·4: Infidelity as a function of Ω Numerically calculated infidelity $(1 - F)$ of the initial ground state of the FE Hamiltonian with the initial state, $|+x\rangle$, as a function of the parameter Ω.

Another point mentioned in the main text is the choice of the parameter Ω in the FE Hamiltonian. This parameter appears in the rotating frame transformation operator $V = \exp(i\sigma_x \Omega \cos \omega t)$, and hence in the lab frame FE Hamiltonian. As mentioned in the appendix B.1, for the initial states in the lab and rotating frames to agree at time $t = 0$, we require that $\Omega = n\pi$, for an integer n. However, if the initial ground state is along the x-axis, this operator does not rotate the state and merely adds an overall phase, meaning there is no restriction on Ω. Freedom in choosing Ω is useful from an experimental point of view because the Floquet driving term, $\omega \Omega \sin \omega t$, is easier to implement if the amplitude can be made smaller by taking a smaller value of Ω. As explained above, the initial ground state

is not exactly along the x-axis, but instead slightly above it in the x-z plane. Thus, taking $\Omega \neq n\pi$ could result in errors in the initial state being different from the initial ground state.
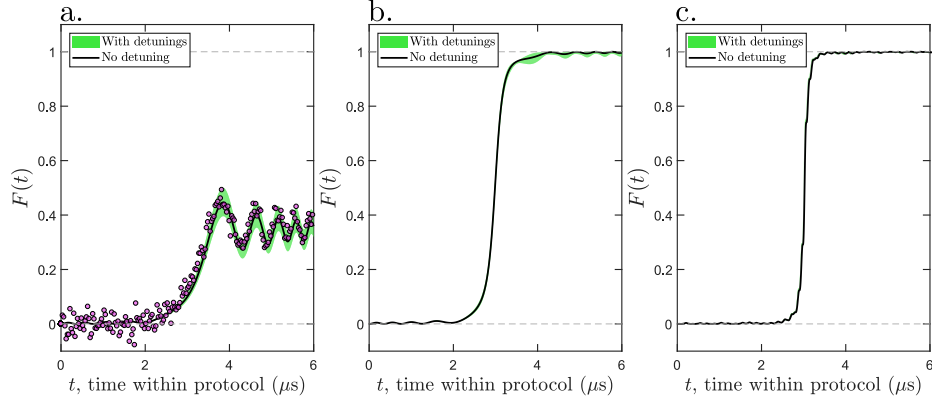
Figure B·5: Protocol performance with detuning a. Simulation of Landau-Zener protocol with detunings $\delta\sigma_z$ drawn from a Gaussian distribution $\delta \sim N(\mu = 0, \sigma = 8kHz)$. The simulation is repeated many times and the results averaged together with the green band capturing the mean fidelity ± 1 standard deviation at each point in time. Black curve is the simulation with no detuning. Data is plotted as well to show it falls within the green band. Plots b. and c. are the same as a. for the FF and FE protocols, respectively. Note that the uncertainty band for the FE protocol is not visible at this scale. Data points are omitted since the spread in the data is larger than the bands. Parameters are the same as for Figure B·3.

To show that we can still choose Ω freely without introducing significant infidelities, we computed the infidelity of the initial state, $|-x\rangle$, with the initial ground state of the Floquet-engineered Hamiltonian as a function of Ω, shown in Figure B·4. We see that for almost all values of Ω, the states have infidelities of $I = 1 - |\langle -x|\psi_{GS}(t = 0, \Omega)\rangle|^2 \leq 0.002$, consistent with the infidelities we expect based only on the fact that $\Delta/\lambda_0 \neq 0$, as discussed above. The isolated points where the infidelity changes rapidly occurs when Ω approaches points such that $J_1(2\Omega) = 0$. Near these points, we can approximate $B_z \sim \Delta - c/J_1(2\Omega)$, for a constant $c \ll \Delta$. As Ω increases from below, it approaches $\Delta \approx c/J_1(2\Omega)$, so that $B_z = 0$ and the ground state points along the x-axis, matching the initial state. Increasing Ω slightly more results in a large B_z and the ground state points nearly along the -z-axis, giving large

infidelities. As long we avoid these points when choosing Ω, the initial infidelity will be small and we can expect the final infidelity to be comparably small, as in Figure B·3 where we examined the effect of small infidelities from the initial state.

A final imperfection we consider is detuning from the transition frequency ω_0. As shown above, we perform electron spin resonance (ESR) to determine ω_0 and then set the signal generator to this frequency. If the applied fields $B_{x,y}$ are detuned from resonance by a small amount δ, then in the rotating frame there is an additional term $\delta\sigma_z$. In our experiment, detunings result from two main sources. First, changes in the temperature or humidity of the laboratory cause drift in the distance of the NV center from the static magnet B_s, shifting the ESR frequency. We observe drift in ω_0 of no more than 50-100kHz on the timescale of a day. To avoid detuning resulting from this drift, we perform ESR measurements at regular intervals of 20-60 minutes during experiments and retune the frequency.

The second source of detuning is the uncertainty in the measured frequency ω_0. After performing ESR, we fit the normalized data to Lorentzian lineshapes, which results in some numerical uncertainty in the fit parameters. Defining the uncertainty as half the width of the 66% confidence interval of the fit parameters, we find typical uncertainties in ω_0 of ±6-10kHz. We investigate how this might affect each proctol by running a simulation with an additional term $\delta\sigma_z$ where δ is drawn from a Gaussian distribution of mean zero and standard deviation 8kHz, and then averaging together the fidelities as a function of time for many iterations with independent values of δ. The results in Figure B·5 show that the Landau-Zener protocol is most sensitive as the uncertainty band is largest and that detunings might explain some of the deviation of the data from the simulation without detunings. We also see that the FE protocol is more robust against detunings than the FF protocol and is unaffected at this scale.

B.4 Noise

B.4.1 Experimental details

To generate classical magnetic field noise, we applied several amplification stages to the Johnson noise of a resistor at room temperature to produce white noise band-limited by the amplifiers. Because the bandwidth of the amplifiers was 300MHz, much less than the transition frequency ω_0, the noise cannot drive $|0\rangle \leftrightarrow |+1\rangle$ transitions and is well described by pure dephasing: $H_{\text{noise}} = \gamma(t)\sigma_z$. The noise signal was combined with $B_z(t)$ to deliver it to the waveguide where it creates a magnetic field.

We characterized the noise by its amplitude spectral density, which we varied by adding attenuators, and its bandwidth, which we varied by adding low pass filters. We used commercially available 5th order elliptic filters which have fast rolloff of >20dB/octave, allowing us to approximate them as ideal low pass filters with constant spectral density and a hard cutoff which we define as the -3dB point. We measure the RMS of the noise generator using a digital oscilloscope and then apply the calibration to determine the magnitude of B_z as explained above.

To check this calibration and characterize the noise, we performed a detuned Ramsey experiment with the external noise and fit the envelope of the Ramsey fringes to an exponential decay to measure T_2^*. The data, reported as the dephasing rate $\Gamma = 1/T_2^*$ is reported in fig. B·6, for the RMS and bandwidths used in fig. 4. of the main text. Fig. B·6 (a) shows that as the RMS increases, the coherence time decreases. The coherence time approaches a constant value as the added noise becomes weak and is dominated by electronic noise independent of the added noise and the dephasing resulting from the spin environment of the NV center. We find that with no added noise, $\Gamma = 0.125 \pm 0.003$ MHz, consistent with the value the data is approaching. In fig. B·6 (b), plotted on the same scale as fig. B·6 (a), we see that T_2^* is nearly independent of frequency. This is expected since T_2^* is most sensitive to low frequency noise, so increasingly higher frequencies get averaged out and

do not affect the dynamics.
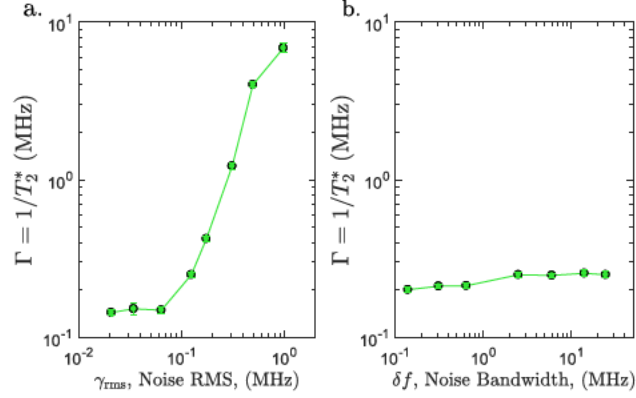
Figure B·6: Decoherence rate with external noise a. Decoherence rate as a function of the amplitude of added noise at a fixed bandwidth of 2.5MHz. At small amplitudes, the dominant contribution to decoherence is from sources intrinsic to this NV center, and hence independent from the external noise. b. Decoherence rate as a function of the added noise bandwidth at fixed spectral density. T_2^* is most sensitive to low frequency noise and is hence almost independent from the large bandwidths we consider.

We then simulated the Ramsey experiment using the same bandwidth and adjusted the noise amplitude spectral density (ASD) until the simulated T_2^* agreed with the experimental value. For a particular filter with bandwidth 2.5MHz, used in fig. 4 (a) of the main text, we find that the value of the simulated ASD required to match the T_2^* is approximately 28% larger than that estimated using the oscilloscope measurement, represented as a factor $\alpha = 1.28$. This factor can be understood as a correction to the measured RMS to account for the fact that the actual filters used do not have ideal filter shapes, meaning the model ignores noise above the -3dB point and slightly underestimates the power in the bandpass region at frequencies below the -3dB point. As a result, this correction factor will differ for different filters.

We applied this correction factor to the simulations in fig. 4 (a, c) of the main text because they use a single filter and hence are described by a single value of alpha. In fig. 4 (b), however, we use only the ASD measured by the oscilloscope since each point is

taken using a different filter. As shown in fig. B·6 (b), T_2^* has a weak dependence on the bandwidth at the frequencies used, so we can not reliably extract α for each point since T_2^* gives minimal information.

B.4.2   Numerical simulation details

In the experiment, noise was characterized by spectral bandwidth ω_c and RMS. Keeping this in mind, for numerical simulations we define the noise as:

$$\gamma(t) = \sqrt{\frac{2\omega_c \Gamma}{N}} \sum_{j=1}^{N} \cos(\omega_j t + \phi_j) \tag{B.12}$$

where Γ is the noise spectral density and ω_j represents different allowed frequencies within a certain bandwidth ω_c. ϕ_j and ω_j are chosen from random uniform distribution with $\phi_j \in [0, 2\pi)$ and $\omega_j \in [0, \omega_c)$. We note that the RMS amplitude is $\gamma_{RMS} = \sqrt{\omega_c \Gamma}$.

B.5   Dynamical decoupling effect in FE driving protocol

As mentioned in the main text, the FE protocol protects the qubit from environmental noise as long as the noise spectral bandwidth is well separated from the spectral bandwidth of the driving protocol, which is simply given by its Fourier transform. In Fourier space, the noise spectrum is centered around zero with a bandwidth ω_c, while the B_z term of H_{FE} (equation (4) in the main paper) is centered around the Floquet frequency. Its spectrum is given by the Fourier transform of:

$$(\Theta(t) - \Theta(t - \tau)) \cos \omega t \frac{\dot{\lambda}}{\Delta^2 + \lambda(t)^2} \tag{B.13}$$

where $\Theta(t)$ is Heaviside step function and ω is the Floquet frequency. The box function $\Theta(t) - \Theta(t - \tau)$ arises because our protocol is applied for the time $t \in [0, \tau]$. For linear ramps, we have $\lambda(t) = \lambda_0(1 - 2t/\tau)$.

The total spectral function is a convolution of the Fourier transforms of the box function,

cosine, and the factor $\frac{\dot{\lambda}}{\Delta^2 + \lambda(t)^2}$, which for a linear ramp is a Lorentzian. Their Fourier transforms are a *sinc* function, Dirac delta function peaked at the Floquet frequency ω, and an exponential, respectively. The characteristic width of the *sinc* scales inversely proportional to the protocol duration as $1/\tau$, while the Fourier transform of the Lorentzian decays in Fourier space over a typical scale $\frac{\lambda_0}{\tau\Delta}$. Here we are interested in the limit where $\lambda_0 \gg \Delta$, so the convolution with the *sinc* is irrelevant and the protocol spectrum is approximately an exponential centered around ω with a characteristic decay rate $\frac{\lambda_0}{\tau\Delta}$. FE protocols are thus protected from noise as long as $\omega_c \ll \omega - \frac{\lambda_0}{\tau\Delta}$.

To demonstrate this, we performed simulations of the Floquet-engineered protocol where we apply the noise function described above and repeat the simulation for many realizations of the noise, averaging the fidelities together. The results in fig. B·7 show that for large enough Floquet frequency, the Floquet-engineered protocol (data markers and solid lines) gives lower infidelity than the conventional FF protocol (horizontal dashed lines). The infidelity decreases with increasing Floquet frequency until the Floquet frequency reaches $\omega \approx \omega_c + \lambda_0/(\tau\Delta)$, and the Floquet driving can no longer further decouple the system from the noise and the infidelity saturates.

In fig. B·7 a), as we increase the noise bandwidth ω_c while keeping the spectral density Γ constant, we find that with a large enough Floquet frequency, the Floquet-engineered protocol can give the same infidelity when the noise bandwidth is increased. This shows that, like dynamical decoupling, the Floquet-engineered protocol protects the qubit from noise as long the Floquet frequency is larger than ω_c. In fig. B·7 b), as we increase the noise bandwidth ω_c while keeping γ_{RMS} constant, we see that the infidelity of the FF protocol decreases because it is more sensitive to lower frequencies and the spectral density must decrease to give constant γ_{RMS}. However, by increasing the Floquet frequency, the Floquet-engineered protocol can achieve smaller infidelities and saturates approximately when $\omega \approx \omega_c + \lambda_0/(\tau\Delta)$, consistent with the data for constant noise spectral density. Thus,
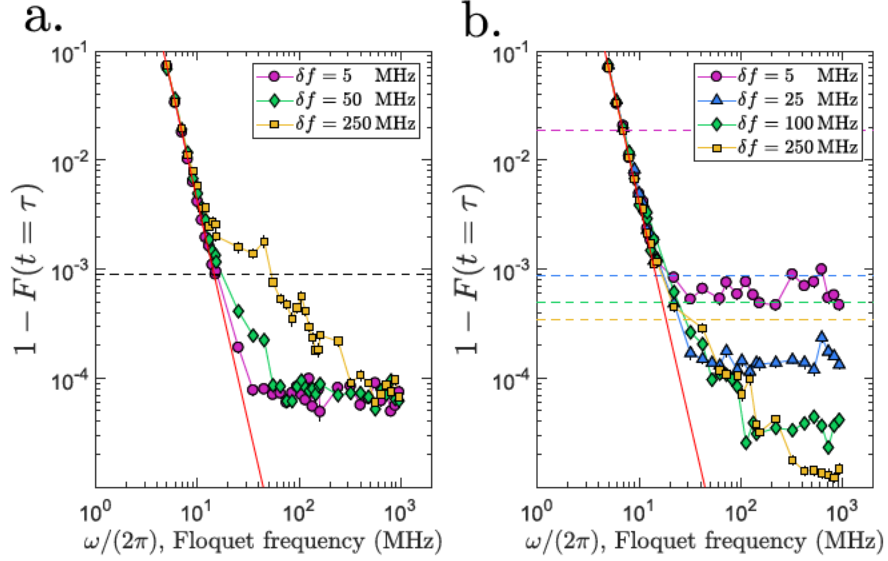
Figure B·7: Simulations of dynamical decoupling effect a. Numerically computed infidelity for Floquet-engineered driving with a cubic protocol as a function of stroboscopically sampled Floquet frequency, $\omega = 2\pi n/\tau$, where n is a positive integer. Each curve corresponds to a noise spectra with different bandwidths but equal spectral density. The black, horizontal dashed line is the fidelity for the conventional FF protocol, which was approximately independent of the noise bandwidth in the regime studied. The red line is the infidelity for a Floquet-engineered protocol with no noise. b. The same simulations as part a., but with constant RMS amplitude. Horizontal lines are the fidelity of the conventional FF protocol for the noise spectrum with the corresponding color. Protocol parameters: $\lambda(t) = \lambda_0(4(t/\tau)^3 - 6(t/\tau)^2 + 1), \Delta/2\pi = 0.1/\mathcal{J}_0(2\Omega)\,\mathrm{MHz}, \Omega = \pi$, $\lambda_0/2\pi = 1.5\,\mathrm{MHz}$ and $\tau = 4\mu s$

the Floquet-engineered protocol can protect the system from noise by driving at high frequency.

Appendix C

Appendix for Floquet-engineering Counterdiabatic Protocols in Quantum Many-body Systems

C.1   Regularized gauge potentials

As one way of motivating the variational ansatz, the adiabatic gauge potential (for fixed λ) can be rewritten as

$$\mathcal{A}_\lambda = \lim_{\varepsilon \to 0^+} \int_0^\infty dt \ e^{-\varepsilon t} \left(e^{-i\mathcal{H}(\lambda)t} \partial_\lambda \mathcal{H}(\lambda) e^{i\mathcal{H}(\lambda)t} - \mathcal{M}_\lambda \right) \tag{C.1}$$

with $\mathcal{M}_\lambda = \overline{\partial_\lambda \mathcal{H}} = \sum_n |n\rangle \langle n|\partial_\lambda \mathcal{H}|n\rangle \langle n|$ cancelling the diagonal elements by construction, similar to the integral expression for the classical gauge potential (Jarzynski, 1995). This immediately follows from the evaluation of the off-diagonal elements

$$\begin{aligned}
\langle m|\mathcal{A}_\lambda|n\rangle &= \lim_{\varepsilon \to 0^+} \int_0^\infty dt \ e^{-\varepsilon t} e^{-i(\varepsilon_m - \varepsilon_n)t} \langle m|\partial_\lambda \mathcal{H}|n\rangle \\
&= \lim_{\varepsilon \to 0^+} \frac{\langle m|\partial_\lambda \mathcal{H}|n\rangle}{\varepsilon + i(\varepsilon_m - \varepsilon_n)}.
\end{aligned} \tag{C.2}$$

From the Baker-Campbell-Hausdorff expansion, we can write

$$e^{-i\mathcal{H}t} \partial_\lambda \mathcal{H} e^{i\mathcal{H}t} = \sum_{k=0}^\infty \frac{(-it)^k}{k!} \underbrace{[\mathcal{H}, [\mathcal{H}, \ldots [\mathcal{H}, \partial_\lambda \mathcal{H}]],}_{k} \tag{C.3}$$

where the (real for real Hamiltonians) even-order commutators will contribute to $\mathcal{M}_\lambda$ and the odd-order commutators constitute $\mathcal{A}_\lambda$. While the resulting geometric series is not convergent for small ε, this hints at the use of the nested commutators to reconstruct the gauge potential.

A 'gapped' gauge potential $\mathcal{A}_\lambda^\Delta$ can alternatively be defined as

$$\mathcal{A}_\lambda^\Delta \equiv i \sum_{k=1}^\infty \frac{(-1)^k}{k!} \Delta^{-2k} \underbrace{[\mathcal{H}, [\mathcal{H}, \ldots [\mathcal{H}, \partial_\lambda \mathcal{H}]]}_{2k-1}, \tag{C.4}$$

satisfying

$$\begin{aligned} \langle m|\mathcal{A}_\lambda^\Delta|n \rangle &= i \sum_{k=1}^\infty \frac{(-1)^k}{k!} \Delta^{-2k} (\varepsilon_m - \varepsilon_n)^{2k-1} \langle m|\partial_\lambda \mathcal{H}|n \rangle \\ &= -i \frac{1 - e^{-(\varepsilon_m - \varepsilon_n)^2/\Delta^2}}{\varepsilon_m - \varepsilon_n} \langle m|\partial_\lambda \mathcal{H}|n \rangle, \end{aligned} \tag{C.5}$$

acting as the exact gauge potential for all excitation frequencies $(\varepsilon_m - \varepsilon_n)$ above a gap Δ, and vanishing for excitation frequencies $(\varepsilon_m - \varepsilon_n)$ below Δ. Through the introduction of a finite gap, a regularized gauge potential can be expressed in terms of nested commutators, remaining well-defined in the thermodynamic limit, which can then be used to strongly suppress excitations above this gap, similar in spirit to Ref. (Bachmann et al., 2017). In practice, this series summation will be truncated, where the variational minimization is guaranteed to return the optimal series coefficients.

Note that, for a finite number of excitation frequencies, as in e.g. few-body systems, the exact gauge potential term can always be obtained taking a large enough commutator ansatz. If the number of terms in the ansatz equals the number of relevant excitation frequencies, there are enough degrees of freedom to make the frequency-dependent prefactor reproduce the exact prefactor $1/\omega_{mn}$ at all excitation frequencies ω_{mn}, such that the proposed expansion becomes exact (as illustrated by the two-qubit examples in the main text).

Alternatively, the variational optimization can be avoided if we only wish to approximate the prefactor $1/\omega_{mn}$ for a given range of excitation frequencies $\omega_{mn} \in [\Delta_{min}, \Delta_{max}]$ for a given Δ_{min} and Δ_{max}. This could occur in systems with a known gap or a given excitation spectrum, where the counterdiabatic driving only needs to suppress excitations in a known frequency window. In this case, the fitting implicit in the variational procedure can be replaced by a straightforward fitting of $1/\omega_{mn}$ to a power series of a given order (see also the main text). This can be done in various efficient ways, and has the advantage that the gauge potential depends only on the system through the given Δ_{min} and Δ_{max}, which might outperform the variational gauge potential if the action for the adiabatic gauge potential is dominated by excited states, resulting in a potential that is not expected to perform well for CD driving w.r.t. the ground state.

C.2   Variational minimization

The exact gauge potential can be found by minimizing the action (Sels and Polkovnikov, 2017)

$$S(\chi) = \mathrm{Tr}\left[G^\dagger(\chi)G(\chi)\right], \; G(\chi) = \partial_\lambda \mathcal{H} - i[\mathcal{H}, \chi], \tag{C.6}$$

which is minimal precisely when $\chi = \mathcal{A}_\lambda$. This allows for the construction of approximate local gauge potentials by minimizing $S(\chi)$ in a restricted basis for χ, including e.g. all local operators with a given support.

The results for the Figure in the main text are given in Fig. C·1, as compared with the variational results when constructing the gauge potential in a local basis as

$$\mathcal{A}_\lambda \approx \sum_{i=1}^{L} \alpha_{i,i+1,\dots,i+d}^{a_1 a_2 \dots a_d} \, \sigma_i^{a_1} \sigma_{i+1}^{a_{i+1}} \dots \sigma_{i+d}^{a_{i+d}}, \tag{C.7}$$

with $\alpha_{i,i+1,\dots,i+d}^{a_1 a_2 \dots a_d}$ the variational parameters and $a_i = x, y, z, 0$. While the variational procedure minimizes $S_\ell = \mathrm{Tr}\left[G_\ell^2\right]$, the variational minimum is obtained when $[\mathcal{H}, G_\ell] = 0$, such that the latter can also be used as a measure for the resulting error. Despite only having a
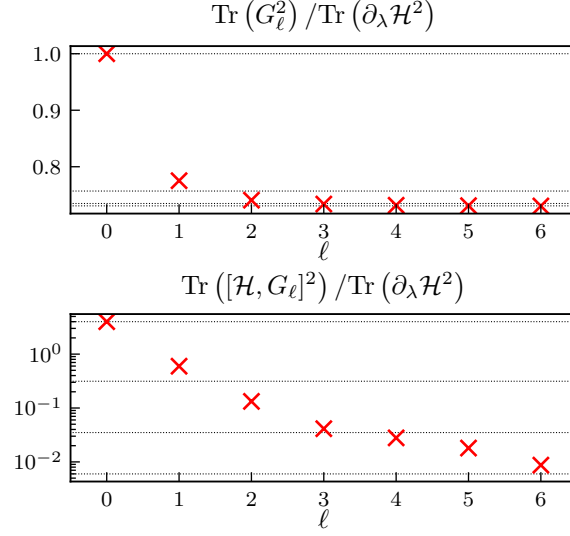
Figure C·1: Variational minimum for $S_\ell = \text{Tr}\left[G_\ell^2\right]$ and resulting error in $[\mathcal{H}, G_\ell]$ for Fig. 1 in the main text. Everything is normalized by $\text{Tr}\left[\partial_\lambda \mathcal{H}^2\right]$ in order to be system-size independent. The dotted lines denote the results when constructing the gauge potential in a local basis with support $d = 1, 2, 3, 4$.

fraction of the parameters in the local ansatz, it is clear that the nested commutator ansatz can capture most of the relevant local contributions to the gauge potential.

An additional interpretation can be given to the minimization of the coefficients in $\mathcal{A}_\lambda^{(\ell)}$. Taking $\chi = \mathcal{A}_\lambda^{(\ell)}$, we can write $G_\ell \equiv G(\mathcal{A}_\lambda^{(\ell)})$ as

$$G_\ell = \partial_\lambda \mathcal{H} + \sum_{k=1}^{\ell} \alpha_k \underbrace{[\mathcal{H}, [\mathcal{H}, \dots [\mathcal{H}, \partial_\lambda \mathcal{H}]]}_{2k}, \tag{C.8}$$

where the action can again be expanded in the eigenbasis of $\mathcal{H}$ as

$$S(\chi) = \sum_{m,n} |\langle m|\partial_\lambda \mathcal{H}|n\rangle|^2 \left[1 + \sum_{k=1}^{\ell} \alpha_k \omega_{mn}^{2k}\right]^2. \tag{C.9}$$

The resulting minimization leads to a linear set of equations

$$\sum_{k=1}^{\ell} \alpha_k \sum_{m,n} \omega_{mn}^{2(k+l)} |\langle m|\partial_\lambda \mathcal{H}|n\rangle|^2$$

$$= \alpha_l \sum_{m,n} \omega_{mn}^{2l} |\langle m|\partial_\lambda \mathcal{H}|n\rangle|^2, \quad l=1\ldots\ell. \tag{C.10}$$

Defining the response function

$$\Gamma_\lambda(\omega) \equiv \Gamma(\omega, \partial_\lambda \mathcal{H}) = \sum_{m,n} \langle m|\partial_\lambda \mathcal{H}|n\rangle^2 \delta(\omega - \omega_{mn}), \tag{C.11}$$

its moments follow as

$$\Gamma_\lambda^{(k)} = \int d\omega \, \Gamma_\lambda(\omega) \omega^{2k}, \tag{C.12}$$

such that the linear set of equations can be rewritten as

$$\sum_{k=1}^{\ell} \alpha_k \Gamma_\lambda^{(k+l)} = \Gamma_\lambda^{(l)}, \qquad l=1\ldots\ell. \tag{C.13}$$

The left-hand side can be seen as the $(2l+1)$-th moment of $\sum_{k=1}^{\ell} \alpha_k \omega^{2k-1} \Gamma_\lambda(\omega)$, the response function of the approximate gauge potential, where the right-hand side can be seen as the $(2l+1)$-th moment of $\Gamma_\lambda(\omega)/\omega$, the response function for the exact gauge potential, such that the approximate gauge potential reproduces the first ℓ moments of the response function

$$\Gamma(\omega, \mathcal{A}_\lambda)^{(k)} = \Gamma(\omega, \mathcal{A}_\lambda^\ell)^{(k)}, k=1\ldots\ell. \tag{C.14}$$

C.3 Floquet Hamiltonian

Here, we will calculate the matrix elements of the Floquet Hamiltonian defined in the main text. Consider the infinite-frequency limit of

$$\mathcal{H}_{FE}(t) = \left[1 + \frac{\omega}{\omega_0}\cos(\omega t)\right]\mathcal{H}(\lambda) + \dot{\lambda}\beta(t)\partial_\lambda \mathcal{H}(\lambda), \tag{C.15}$$

with

$$\beta(t) = \sum_{k=1}^{\infty} \beta_k \sin((2k-1)\omega t). \tag{C.16}$$

The leading-order contribution to the Floquet Hamiltonian can be obtained by first going to the rotating frame w.r.t. $\frac{\omega}{\omega_0}\cos(\omega t)\mathcal{H}(\lambda)$ as

$$\tilde{\mathcal{H}}_{FE}(t) = e^{i\frac{\sin(\omega t)}{\omega_0}\mathcal{H}(\lambda)} \mathcal{H}_{FE}(t) e^{-i\frac{\sin(\omega t)}{\omega_0}\mathcal{H}(\lambda)} \tag{C.17}$$

from

$$\frac{\sin(\omega t)}{\omega_0}\mathcal{H}(\lambda) = \frac{\omega}{\omega_0} \int_0^t ds \cos(\omega s)\mathcal{H}(\lambda), \tag{C.18}$$

where we have assumed that $\mathcal{H}(\lambda)$ can be taken to be constant during a driving cycle. In this way, the rotating frame coincides with the lab frame at $t = 0$ and $t = T$. The dominant contribution to the Magnus expansion is given by the time-averaged Hamiltonian in the moving frame as

$$\tilde{\mathcal{H}}_F^{(0)} = \frac{1}{T}\int_0^T dt\ e^{i\frac{\sin(\omega t)}{\omega_0}\mathcal{H}(\lambda)} \mathcal{H}_{FE}(t) e^{-i\frac{\sin(\omega t)}{\omega_0}\mathcal{H}(\lambda)}. \tag{C.19}$$

In order to continue, it will prove to be convenient to express the matrix elements in the eigenbasis of $\mathcal{H}(\lambda)$, where the off-diagonal elements are given by

$$\begin{aligned}
\langle m|\tilde{\mathcal{H}}_F^{(0)}|n\rangle &= \frac{\dot{\lambda}}{T}\int_0^T dt\ e^{i\sin(\omega t)\frac{(\varepsilon_m - \varepsilon_n)}{\omega_0}} \beta(t)\langle m|\partial_\lambda \mathcal{H}|n\rangle \\
&= \dot{\lambda}\sum_{k=-\infty}^{\infty} \mathcal{J}_k\left(\frac{\varepsilon_m - \varepsilon_n}{\omega_0}\right)\langle m|\partial_\lambda \mathcal{H}|n\rangle \\
&\quad \times \frac{1}{T}\int_0^T dt\ e^{i\omega k t}\beta(t), \tag{C.20}
\end{aligned}$$

where the Jacobi-Anger formula has been used in order to recast the exponential as a sum of Bessel functions of the first kind. The integral then returns the Fourier coefficients of

$\beta(t)$, leading to

$$\langle m|\tilde{\mathcal{H}}_F^{(0)}|n\rangle = i\dot{\lambda} \sum_{k=1}^{\infty} \beta_k \mathcal{I}_{2k-1}\left(\frac{\varepsilon_m - \varepsilon_n}{\omega_0}\right) \langle m|\partial_\lambda \mathcal{H}|n\rangle. \qquad (C.21)$$

Since the rotating frame coincides with the lab frame at initial and final times, the resulting Floquet Hamiltonian satisfies

$$\langle m|\mathcal{H}_F^{(0)}|n\rangle = i\dot{\lambda} \sum_{k=1}^{\infty} \beta_k \mathcal{I}_{2k-1}\left(\frac{\varepsilon_m - \varepsilon_n}{\omega_0}\right) \langle m|\partial_\lambda \mathcal{H}|n\rangle. \qquad (C.22)$$

The contribution to the diagonal elements is simply given by the time-averaged $\mathcal{H}(\lambda)$, which can be assumed constant within a single driving cycle, leading to the proposed expression in the main text. The Bessel functions can be Taylor expanded around zero, leading to

$$\mathcal{H}_F = \mathcal{H} + i\dot{\lambda} \sum_{k=1}^{\infty} \beta_k \sum_{m=0}^{\infty} \frac{(-1)^m (2\omega_0)^{-2k-2m+1}}{m!(m+2k-1)!}$$
$$\times \underbrace{[\mathcal{H},[\mathcal{H},\ldots[\mathcal{H},\partial_\lambda\mathcal{H}]]}_{2m+2k-1}. \qquad (C.23)$$

Note that, since the matrix elements again reproduce the structure of the exact gauge potential and the expansion for the gauge potential ($\langle m|\partial_\lambda\mathcal{H}|n\rangle$ multiplied by an excitation-frequency-dependent term), Floquet engineering provides a general way to realize the counterdiabatic term. From the expression for the Floquet Hamiltonian, if the number of harmonics equals the number of relevant excitation frequencies, there are enough degrees of freedom to make the frequency-dependent prefactor reproduce the exact prefactor at all excitation frequencies, such that exact counterdiabatic driving can in principle always be exactly obtained using Floquet engineering in the infinite-frequency limit, even if the resulting expressions might be rather unwieldy.

The first-order correction on this Hamiltonian can also be calculated in the moving

frame as

$$\mathcal{H}_F^{(1)} = \frac{1}{2iT^2} \int\limits_0^T dt_1 \int\limits_0^{t_1} dt_2 \, [\tilde{\mathcal{H}}_{FE}(t_1), \tilde{\mathcal{H}}_{FE}(t_2)], \tag{C.24}$$

which can be expanded as

$$\langle m|\mathcal{H}_F^{(1)}|n\rangle = \frac{\dot{\lambda}}{2iT^2}(\varepsilon_m - \varepsilon_n)\langle m|\partial_\lambda\mathcal{H}|n\rangle$$

$$\times \int\limits_0^T dt_1 \int\limits_0^{t_1} dt_2 \left[(1 + \frac{\omega}{\omega_0}\cos(\omega t_1))\beta(t_2)e^{i\frac{\varepsilon_m - \varepsilon_n}{\omega_0}\sin(\omega t_2)} \right.$$

$$\left. - (1 \leftrightarrow 2) \right]$$

$$+ \frac{\dot{\lambda}^2}{2iT^2}\sum_l \int\limits_0^T dt_1 \int\limits_0^{t_1} dt_2 \beta(t_1)\beta(t_2)e^{i\sin(\omega t_1)\frac{\varepsilon_m - \varepsilon_l}{\omega_0}}$$

$$\times e^{i\sin(\omega t_2)\frac{\varepsilon_l - \varepsilon_n}{\omega_0}}\langle m|\partial_\lambda\mathcal{H}|l\rangle\langle l|\partial_\lambda\mathcal{H}|n\rangle. \tag{C.25}$$

This can no longer be exactly evaluated because of the sum over the full Hilbert space, but it should be clear that the $O(T)$ correction has two contributions determined by $\dot{\lambda}\langle m|[\mathcal{H},\partial_\lambda\mathcal{H}]|n\rangle$ and $\dot{\lambda}^2\langle m|\partial_\lambda\mathcal{H}|l\rangle\langle l|\partial_\lambda\mathcal{H}|n\rangle$. This first term results in a correction on the coefficients in the dominant contribution, whereas the second term introduces new interactions in the Floquet Hamiltonian scaling as $\dot{\lambda}^2$.

It is worth remarking that one possible issue relevant for Floquet dynamics is that of heating – at sufficiently long time scales, any many-body system subjected to periodic driving is expected to heat up to a featureless infinite-temperature state (D'Alessio and Rigol, 2014). However, this is not expected to be relevant for the current protocol: in the high-frequency regime where our Magnus expansion holds heating is exponentially suppressed in the driving frequency (Abanin et al., 2015; Kuwahara et al., 2016; Mori et al., 2016), and the aim of the counterdiabatic driving is precisely to reduce the length of the protocol such that the time scales necessary for substantial heating are generally not reached, as also apparent from the calculations presented in the main text.

C.4 Examples

In this Appendix, we explicitly calculate the single-commutator expansion for the two-qubit systems in the main text. First consider the two-level system

$$\mathcal{H} = J\left(\sigma_1^x\sigma_2^x + \sigma_1^z\sigma_2^z\right) + h_z(\lambda-1)\left(\sigma_1^z + \sigma_2^z\right), \tag{C.26}$$

$$\partial_\lambda\mathcal{H} = h_z\left(\sigma_1^z + \sigma_2^z\right). \tag{C.27}$$

The first-order commutator is given by

$$[\mathcal{H},\partial_\lambda\mathcal{H}] = -2iJh_z\left(\sigma_1^y\sigma_2^x + \sigma_1^x\sigma_2^y\right), \tag{C.28}$$

and keeping only this term in the commutator expansion leads to

$$\mathcal{A}_\lambda^{(1)} = 2\alpha_1 Jh_z\left(\sigma_1^y\sigma_2^x + \sigma_1^x\sigma_2^y\right). \tag{C.29}$$

The single coefficient α_1 follows from the operator $G_1 = \partial_\lambda\mathcal{H} - i[\mathcal{H},\mathcal{A}_\lambda^{(1)}]$, given by

$$\begin{aligned} G_1 &= h_z\left(1+\alpha_1 4J^2\right)\left(\sigma_1^z + \sigma_2^z\right) \\ &\quad - \alpha_1(\lambda-1)8Jh_z^2\left(\sigma_1^x\sigma_2^x - \sigma_1^y\sigma_2^y\right), \end{aligned} \tag{C.30}$$

leading to the action $S_1 = \mathrm{Tr}\left[G_1^2\right]$ as

$$S_1 = 2h_z^2\left(1+\alpha_1 4J^2\right)^2 + 2\alpha_1^2(\lambda-1)^2\left(8Jh_z^2\right)^2. \tag{C.31}$$

Minimizing S_1 leads to a linear equation for α_1 and

$$\alpha_1 = -\frac{1}{4J^2 + 16(\lambda-1)^2 h_z^2}, \tag{C.32}$$

resulting in the proposed gauge potential

$$\mathcal{A}_\lambda^{(1)} = -\frac{Jh_z}{2} \frac{\left(\sigma_1^y \sigma_2^x + \sigma_1^x \sigma_2^y\right)}{J^2 + 4(\lambda - 1)^2 h_z^2}. \tag{C.33}$$

For the three-level system, $\mathcal{A}_\lambda^{(1)} = i\alpha_1 [\mathcal{H}, \partial_\lambda \mathcal{H}]$ can also be exactly calculated. Starting from

$$\mathcal{H} = -2J\sigma_1^z \sigma_2^z - h\left(\sigma_1^z + \sigma_2^z\right) + 2h\lambda\left(\sigma_1^x + \sigma_2^x\right), \tag{C.34}$$

$$\partial_\lambda \mathcal{H} = 2h\left(\sigma_1^x + \sigma_2^x\right), \tag{C.35}$$

the relevant operators follow as

$$[\mathcal{H}, \partial_\lambda \mathcal{H}] = -8iJh\left(\sigma_1^y \sigma_2^z + \sigma_1^z \sigma_2^y\right) - 4ih^2(\sigma_1^y + \sigma_2^y),$$

$$G_1 = \left(2h + \alpha_1\left(32J^2 h + 8h^3\right)\right)\left(\sigma_1^x + \sigma_2^x\right)$$

$$+ 32\alpha_1 Jh^2 \left(\sigma_1^x \sigma_2^z + \sigma_1^z \sigma_2^x\right) + 16\alpha_1 \lambda h^3 \left(\sigma_1^z + \sigma_2^z\right)$$

$$+ 64\alpha_1 J\lambda h^2 \left(\sigma_1^z \sigma_2^z - \sigma_1^y \sigma_2^y\right). \tag{C.36}$$

Minimizing the resulting action then returns

$$\alpha_1 = -\frac{J^2 + h^2/4}{(4J^2 + h^2)^2 + (2\lambda h^2)^2 + (4Jh)^2 + (8J\lambda h)^2}. \tag{C.37}$$

Appendix D

Appendix for Adiabatic Eigenstate Deformations as a Sensitive Probe for Quantum Chaos

D.1   Cutoff scaling with system size

Unless stated otherwise, in all calculations we have chosen a cutoff $\mu = L\mathcal{D}^{-1}$, where $\mathcal{D}$ is the dimension of the Hilbert space. The prefactor L has been chosen to remove the logarithmic correction coming from the zero-frequency contribution of $|f(\omega = 0)|^2 = L$ in chaotic models (see Appendix D.3). This can also be motivated by plotting the AGP norm and comparing it w.r.t. different choices of cutoff. We first study this norm close to chaotic-integrable transition point and then later describe its effect deep in the chaotic regime.

When we are close to the chaotic-integrable transition point and the cutoff is too small (e.g. $\mu = L^{-1/2}\mathcal{D}^{-1}$), then we find that the AGP norm is too sensitive to the exponentially close eigenstates, showing a non-smooth exponential scaling, which makes it hard to draw any conclusions (see Fig. D·1 a)). On the other hand, if the cutoff is too large (e.g. $\mu = L^2\mathcal{D}^{-1}$), then the AGP norm, albeit smooth, is no longer sensitive to the small strength of integrability-breaking perturbation(see Fig. D·1 b)). In Fig. D·1 c) with $\mu = L\mathcal{D}^{-1}$, we find that the rescaled AGP norm shows an exponential scaling that is both appropriately smooth and exponentially sensitive to integrability-breaking perturbations.

Deep in the chaotic (ergodic) phase, we find that the numerically-obtained scaling for the norm of the AGP is almost the same for the different choices of cutoff scaling we
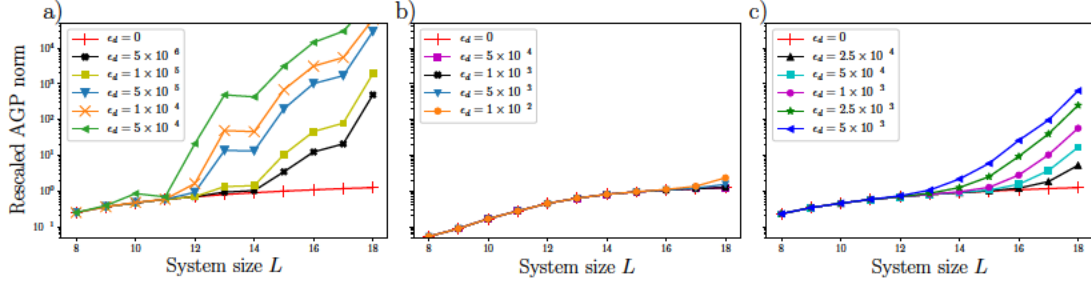
Figure D·1: Effects of regularization. Size dependence of the rescaled AGP norm $||A_\lambda||^2/L$ for different choices of scaling for the cutoff μ close to chaotic-integrable transition point: a) When $\mu = L^{-1/2}\mathcal{D}_0^{-1}$, where $\mathcal{D}_0$ is the dimension of zero magnetization sector, the variation of the norm with system size is noisy. b) When $\mu = L^2\mathcal{D}_0^{-1}$, the norm, albeit smooth, is no longer very sensitive to small integrability-breaking perturbations and c) When $\mu = L\mathcal{D}_0^{-1}$, the norm is both appropriately smooth and exponentially sensitive to integrability-breaking perturbation *Model:* XXZ chain with defect in the middle (Eq. (5.16)). *Parameters:* $\Delta = 1.1, \lambda = \Delta$

studied.

D.2   Derivation of AGP for the free model

As shown in Refs. (del Campo et al., 2012; Kolodrubetz et al., 2017), the AGP for changing the transverse field h_x in a free Ising model with periodic boundary conditions is given by

$$\mathcal{A}_h = \sum_{l=1}^{L} \alpha_l O_l, \tag{D.1}$$

where the operators O_l are given by the following Pauli string operators

$$O_l = \sum_{j=1}^{L} (\sigma_j^x \sigma_{j+1}^z \dots \sigma_{j+l-1}^z \sigma_{j+l}^y + \sigma_j^y \sigma_{j+1}^z \dots \sigma_{j+l-1}^z \sigma_{j+l}^x), \tag{D.2}$$

and the coefficients α_l are given by

$$\alpha_l = -\frac{1}{4L} \sum_{k=0}^{\pi(L-1)/L} \frac{\sin(k)\sin(lk)}{(\cos k - h_x)^2 + \sin^2 k}. \tag{D.3}$$

The norm of the AGP follows as

$$||\mathcal{A}_h||^2 = \frac{1}{2^L} \text{Tr}\left[\mathcal{A}_h^2\right] = 2L \sum_{l=1}^{L} \alpha_l^2, \tag{D.4}$$

where $\text{Tr}\left[O_l O_p\right] = 2^{L+1}L$ was used since all strings of Pauli matrices are trace-orthogonal. The above expression was used to compute the AGP norm for the free model in Fig. 5·2 in the main text.

To obtain the scaling with system size, we can use the analytical expressions of α_l for large enough system sizes (Kolodrubetz et al., 2017), i.e. $\alpha_l = h_x^{-l-1}$ in the paramagnetic phase where $h_x^2 > 1$. Using this, we find that

$$||\mathcal{A}_h||^2 \sim \frac{1}{h_x^2(h_x^2-1)}L(1-e^{-2L\log h_x}). \tag{D.5}$$

Recall that the correlation length in the transverse field Ising model $\sim 1/\log h_x$.

D.3   AGP bound

Recall that the norm of the AGP can be expressed as

$$||\mathcal{A}_\lambda||^2 = \int d\omega \frac{\omega^2}{(\omega^2+\mu^2)^2} \overline{|f_\lambda(\omega)|^2}, \tag{D.6}$$

with

$$\overline{|f_\lambda(\omega)|^2} = \frac{1}{\mathcal{D}} \sum_n \sum_{m\neq n} |\langle n|\partial_\lambda H|m\rangle|^2 \delta(\omega_{nm}-\omega), \tag{D.7}$$

and $\omega_{nm} = E_n - E_m$. It follows directly from eq. (D.6), and $x^2/(x^2+1)^2 \leq 1/4$, that

$$||\mathcal{A}_\lambda||^2 \leq \frac{1}{4\mu^2} \int d\omega |f_\lambda(\omega)|^2 = \frac{||\partial_\lambda H||^2}{4\mu^2} \tag{D.8}$$

Consequently, for any local perturbation the norm of the regularized AGP – where we set $\mu \sim L2^{-L}$ – can't grow faster than 4^L. Not only does it appear that this bound is saturated when probing integrable direction $\partial_\lambda H$ in models in which the integrability is weakly bro-

ken, it further implies that those observables $\partial_\lambda H$ take exponentially long to relax. Indeed, the above scaling can only be achieved by effectively having $|f_\lambda(\mu)|^2 \sim 2^L$. Yet, the total spectral weight, $\int d\omega |f_\lambda(\omega)|^2$, is only polynomially large in the system size, implying that the corresponding spectral weight must be localized in a region $\Delta\omega \sim 2^{-L}$. Combined with expression (5.8), the latter implies $\partial_\lambda H(t)$ takes exponentially long to relax to equilibrium.

For interacting integrable models we found $||\mathcal{A}||^2 \sim L^\beta$, where the exponent β is non-universal. Since the norm is not exponential in system size, the function $|f_\lambda(\mu)|^2 \sim 2^{-L}$. This means that the function should vanish in the zero frequency limit, which implies oscillatory dynamics of the observable $\partial_\lambda H(t)$.

D.4 Effects of the anisotropy in the XXZ model.

In this Appendix, we will again consider the XXZ Hamiltonian (Eq. (5.13)):

$$H_{\text{XXZ}} = \sum_{i=1}^{L-1}(\sigma_{i+1}^x \sigma_i^x + \sigma_{i+1}^y \sigma_i^y) + \Delta \sum_{i=1}^{L-1} \sigma_{i+1}^z \sigma_i^z, \tag{D.9}$$

where Δ is the anisotropy, and we take $\Delta = \lambda$ as the adiabatic deformation, but now at different values of Δ. We find that the slope of the AGP norm depends non-trivially on Δ (Fig. D·2).

D.5 NNN interactions in the XXZ chain

In the main text, we studied the effect of strictly local integrability-breaking operator (whose support is a single site). Looking into the effects of the locality, we here study an extensive integrability-breaking operator. We add a next-nearest-neighbor (NNN) interaction to the XXZ chain, with Hamiltonian given as:

$$H_{\text{NNN}} = H_{\text{XXZ}} + \Delta_2 \sum_{i=1}^{L-2} \sigma_{i+2}^z \sigma_i^z, \tag{D.10}$$
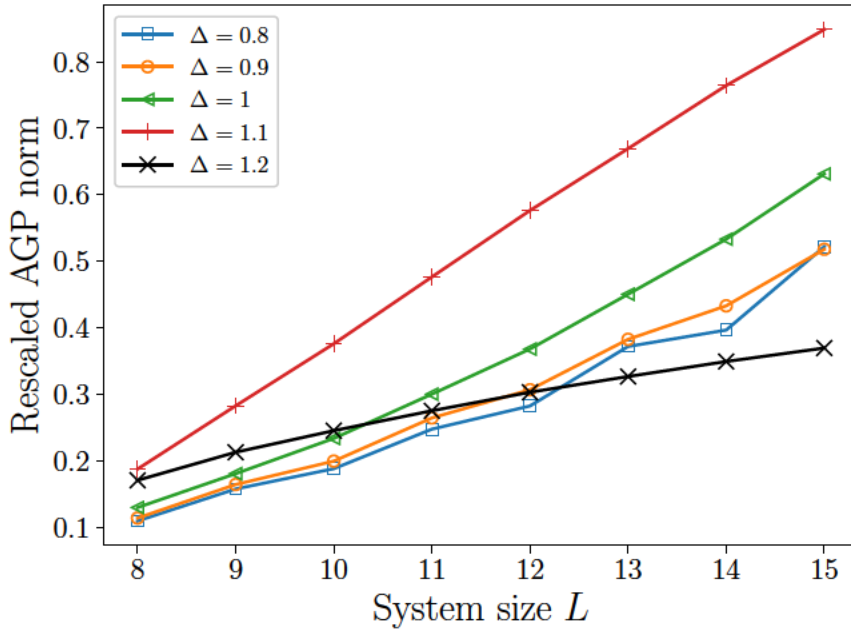
Figure D·2: Anisotropy. Rescaled AGP norm $||\mathcal{A}_\Delta||^2/L$ for the XXZ chain at different values of the anisotropy Δ.

The above model is chaotic for large enough Δ_2 (Gubin and F. Santos, 2012). We choose $\lambda = \Delta$ (Fig. D·3) and $\lambda = \Delta_2$ (Fig. D·4). In the limit $\Delta_2 \rightarrow 0$, when the above Hamiltonian (eqn. D.10) is integrable, the former (latter) is the integrability-preserving (breaking) direction. As shown in Figs. D·3 and D·4, results are similar as for the strictly local perturbation studied in the main text. This implies our results are robust to the nature of the adiabatic deformation.

D.6   Universal slope of the AGP norm

Here we study the AGP norm in the XXZ chain in the limit when the magnitude of the integrability-breaking perturbation (either the local defect energy ε_d or the NNN interaction strength Δ_2) is of the same magnitude as the Δ/J energy scale. In this limit, we find that the AGP has an exponential scaling with system size characterized by an almost universal slope $\beta \approx \log 2$, which is close to the one predicted by ETH. Details about the model and
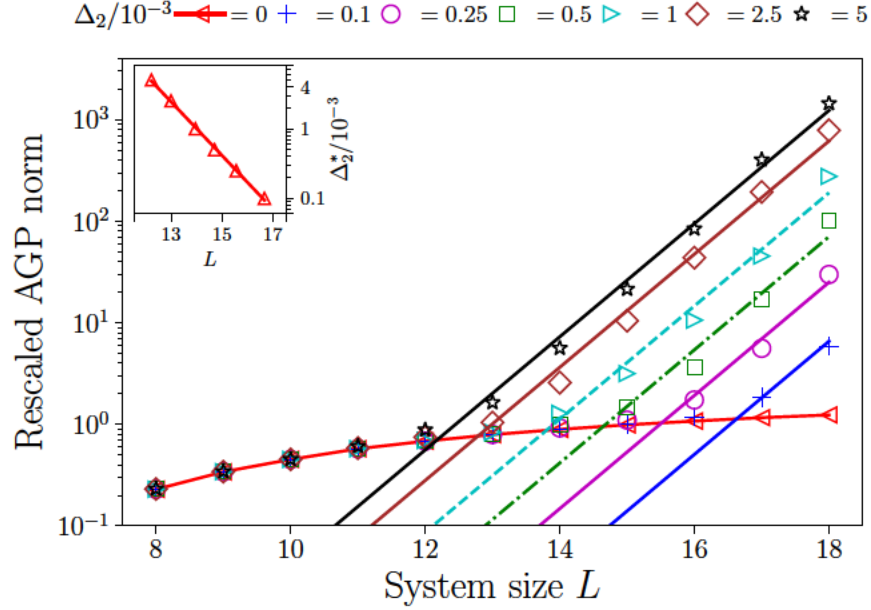
Figure D·3: Integrability breaking through NNN interaction: Rescaled AGP norm $||\mathcal{A}_\lambda||^2/L$ with $\lambda = \Delta$ of the XXZ chain at $\Delta = 1.1$ shows a sharp crossover from polynomial to exponential scaling with system size, even for very small perturbation strengths Δ_2. As Δ_2 decreases, the system size where this crossover happens increases. Straight lines are the exponential fits with $|A_\lambda||^2/L \sim e^{1.28L}$. *Inset:* The integrability-breaking defect energy scales exponentially with system size, i.e. $\Delta_2^* \sim e^{-0.9L}$. This is calculated for the symmetry sector with zero magnetization.

its parameters are given in the caption of Fig. D·5.

D.7   Comparison to many-body "Thouless conductance"

For the sake of completeness, we explicitly compare the current results for a single impurity in an XXZ chain to what would have been obtained using previous related measures (Serbyn et al., 2015; Crowley and Chandran, 2019). The authors of Ref. (Serbyn et al., 2015) define a many-body Thouless conductance

$$G_{\text{NN}} = \frac{1}{\mathcal{D}-1}\sum_n \log \frac{|\langle n|\partial_\lambda H|n+1\rangle|}{E_{n+1}-E_n}, \tag{D.11}$$
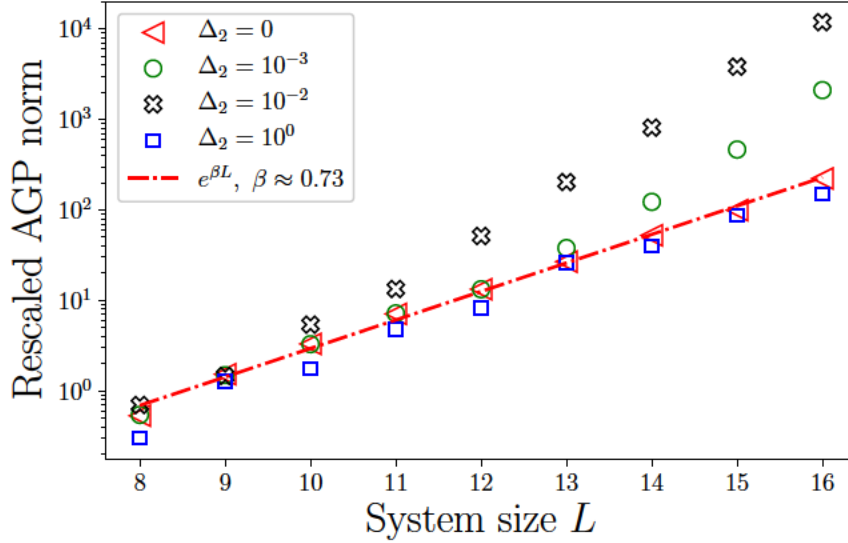
Figure D·4: Integrability-breaking deformation. Rescaled AGP norm $||\mathcal{A}_\lambda||^2/L$ for the XXZ chain at $\Delta = 1.1$ with $\lambda = \Delta_2$. This is calculated for the full Hilbert space, not in any specific symmetry sector.

denoted as $\mathcal{G}$ in (Serbyn et al., 2015). The link to the present $\log ||\mathcal{A}_\lambda||$ is directly apparent. Apart from looking at the typical instead of the mean, the main difference is that G_{NN} only takes into account transitions to neighboring levels. Numerical results are shown in Fig. D·6. In the parameter regime that is studied in work the measure behaves as

$$G_{NN} = \kappa L + c(\varepsilon_d), \tag{D.12}$$

where $\kappa \approx 0.87$ is independent of the perturbation ε_d and the constant c decreases with ε_d. A slightly different measures was introduced in Ref. (Crowley and Chandran, 2019), namely

$$G_{max} = \frac{1}{\mathcal{D}} \sum_n \max_m \log \frac{|\langle n|\partial_\lambda H|m\rangle|}{|E_m - E_n|}, \tag{D.13}$$

denoted as $[\nu]$ in the original work. The latter removes the bias towards neighboring levels and instead takes the maximum possible ratio of the matrix element to the energy difference. As discussed in the main text, at the onset of chaos we see a large amount of spectral
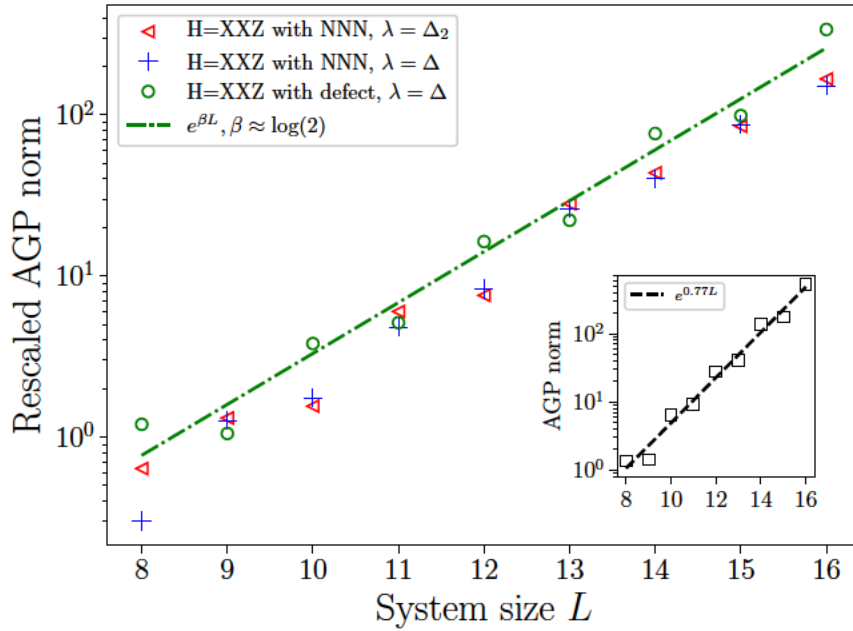
Figure D·5: Universal slope at large integrability-breaking strengths.
Rescaled AGP norm $||A_\lambda||^2/L$ for different models: A) Model: XXZ chain
with NNN interaction (eqn. D.10). a) $\lambda = \Delta$ and b) $\lambda = \Delta_2$. *Parameters:*
$\Delta = 1.1, \Delta_2 = 1$. B) Model: XXZ with defect in the middle (eqn. 5.16).
a) λ is chosen as Δ. *Inset:* AGP norm $||A_\lambda||^2$ for XXZ with defect in the
middle model where λ is chosen as ε_d. *Parameters:* $\varepsilon_d = 1, \Delta = 1.1$. This is
calculated for the full Hilbert space, not in any specific symmetry sector.

weight appear at low frequency and the latter dominates the scaling of the AGP. As a conse-

quence we expect G_{max} to be more sensitive to this phenomenon and more closely resemble

$\log ||\mathcal{A}_\lambda||$. Numerical results are shown in Fig. D·7 and indeed confirm this is the case albeit

features being much less pronounced.
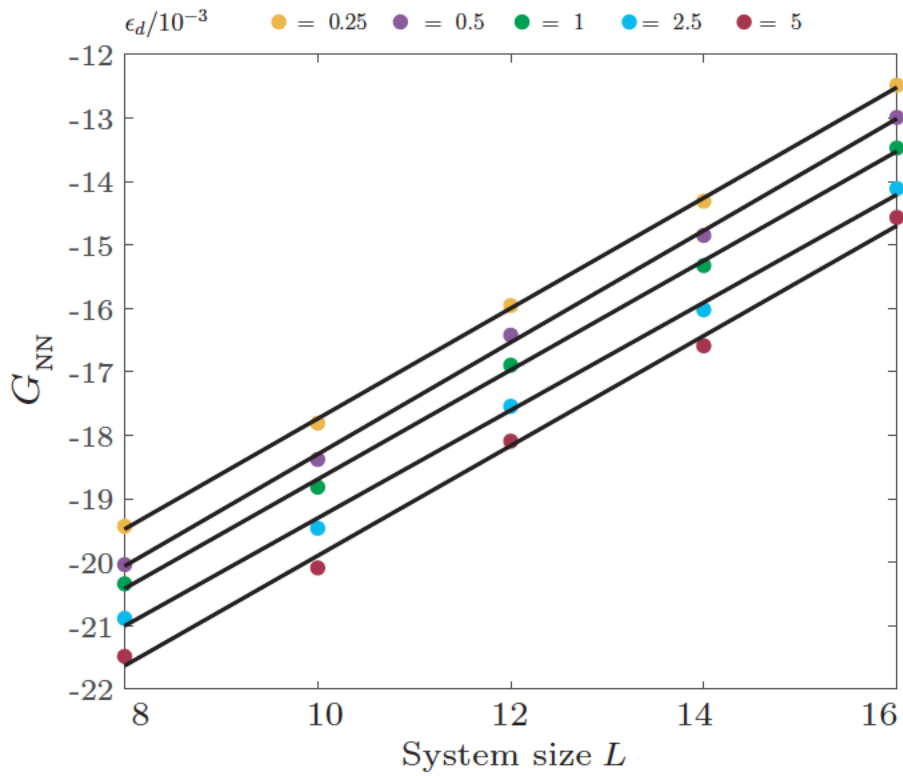
Figure D·6: Probing neighbouring levels. G_{NN} is shown as a function of system size for various strengths of the integrability breaking perturbation. All parameters are the same as those discussed in Fig. 5·3 A. The black lines are linear least square fits to the data.
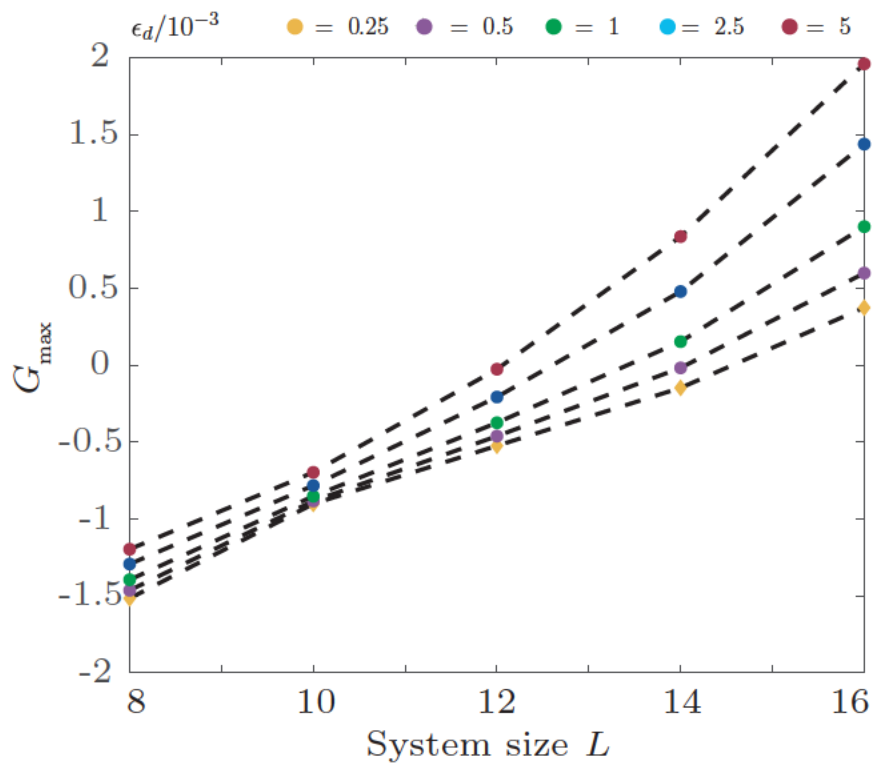
Figure D·7: Probing strongest coupling. G_{max} is shown as a function of system size for various strengths of the integrability breaking perturbation. All parameters are the same as those discussed in Fig. 5·3 A.

List of Abbreviated Titles

Am. J. Phys	. . . .	American Journal of Physics
Ann. Math.	. . . .	Annals of Mathematics
Ann. Phys.	. . . .	Annals of Physics
Annu. Rev. Condens. Matter Phys.	. . . .	Annual Review of Condensed Matter Physics
Commun. Math. Phys.	. . . .	Communications in Mathematical Physics
Contemp. Phys.	. . . .	Contemporary Physics
Dokl. Akad. Nauk SSSR	. . . .	Doklady Akademii Nauk SSSR
Eur. Phys. J. Spec. Top.	. . . .	The European Physical Journal Special Topics
J. Chem. Phys.	. . . .	Journal of chemical physics
J. High Energy Phys.	. . . .	Journal of High Energy Physics
J. Phys. A: Math. Theor.	. . . .	Journal of Physics A: Mathematical and Theoretical
J. Phys.: Condens. Matter	. . . .	Journal of Physics: Condensed Matter
J. Stat. Mech: Theory Exp.	. . . .	Journal of Statistical Mechanics: Theory and Experiment
J. Stat. Phys.	. . . .	Journal of Statistical Physics
Nat. Commun.	. . . .	Nature Communications
Nat. Phys.	. . . .	Nature Physics
New J. Phys.	. . . .	New Journal of Physics
Phys. Lett. A	. . . .	Physics Letter A
Phys. Rep.	. . . .	Physics Reports
Phys. Rev. Appl.	. . . .	Physical Review Applied
Phys. Rev.	. . . .	Physical Review
Phys. Rev. A	. . . .	Physical Review A
Phys. Rev. B	. . . .	Physical Review B
Phys. Rev. E	. . . .	Physical Review E
Phys. Rev. Lett.	. . . .	Physical Review Letters
Phys. Rev. X	. . . .	Physical Review X
Quantum Sci. Technol.	. . . .	Quantum Science and Technology
Rev. Mod. Phys.	. . . .	Reviews of Modern Physics
Russian Math. Surv.	. . . .	Russian Mathematical Surveys
Sci. Adv.,	. . . .	Science advances
SciPost Phys.	. . . .	SciPost Physics

References

Abanin, D. A., Altman, E., Bloch, I., and Serbyn, M. (2019). Colloquium: Many-body localization, thermalization, and entanglement. *Reviews of Modern Physics*, 91(2):21001.

Abanin, D. A., De Roeck, W., and Huveneers, F. (2015). Exponentially Slow Heating in Periodically Driven Many-Body Systems. *Physical Review Letters*, 115(25):256803.

Abanin, D. A. and Papić, Z. (2017). Recent progress in many-body localization. *Annalen der Physik*, 529(7):1–13.

Alba, V., Dubail, J., and Medenjak, M. (2019). Operator entanglement in interacting integrable quantum systems: The case of the rule 54 chain. *Physical Review Letters*, 122:250603.

Albash, T. and Lidar, D. A. (2018). Adiabatic quantum computation. *Rev. Mod. Phys.*, 90:015002.

An, S., Lv, D., Del Campo, A., and Kim, K. (2016). Shortcuts to adiabaticity by counterdiabatic driving for trapped-ion displacement in phase space. *Nat. Commun.*, 7:12999.

Arnold, V. I. (1963). Proof of AN Kolmogorov's theorem on the conservation of conditionally periodic motions with a small variation in the Hamiltonian. *Russian Math. Surv*, 18(9).

Atas, Y., Bogomolny, E., Giraud, O., and Roux, G. (2013). Distribution of the ratio of consecutive level spacings in random matrix ensembles. *Phys. Rev. Lett.*, 110(8):084101.

Avdoshkin, A. and Dymarsky, A. (2019). Euclidean operator growth and quantum chaos. *arXiv preprint arXiv:1911.09672*.

Bachmann, S., De Roeck, W., and Fraas, M. (2017). Adiabatic Theorem for Quantum Spin Systems. *Phys. Rev. Lett.*, 119(6):060201.

Bachmann, S., Michalakis, S., Nachtergaele, B., and Sims, R. (2012). Automorphic equivalence within gapped phases of quantum lattice systems. *Communications in Mathematical Physics*, 309(3):835–871.

Bason, M. G., Viteau, M., Malossi, N., Huillery, P., Arimondo, E., Ciampini, D., Fazio, R., Giovannetti, V., Mannella, R., and Morsch, O. (2012). High-fidelity quantum driving. *Nature Physics*, 8(2):147–152.

Bernien, H., Schwartz, S., Keesling, A., Levine, H., Omran, A., Pichler, H., Choi, S., Zibrov, A. S., Endres, M., Greiner, M., Vuletić, V., and Lukin, M. D. (2017). Probing many-body dynamics on a 51-atom quantum simulator. *Nature*, 551(7682):579–584.

Berry, M. (1989). Quantum chaology, not quantum chaos. *Physica Scripta*, 40(3):335.

Berry, M. (2009). Transitionless quantum driving. *Journal of Physics A: Mathematical and Theoretical*, 42(36):365303.

Berry, M. V. and Tabor, M. (1977). Level clustering in the regular spectrum. *Proceedings of the Royal Society of London. A. Mathematical and Physical Sciences*, 356(1686):375–394.

Bertini, B., Kos, P., and Prosen, T. (2018). Exact Spectral Form Factor in a Minimal Model of Many-body Quantum Chaos. *Phys. Rev. Lett.*, 121(26):264101.

Bertini, B., Kos, P., and Prosen, T. (2020). Operator Entanglement in Local Quantum Circuits I: Chaotic Dual-Unitary Circuits. *SciPost Phys.*, 8:67.

Blatt, R. and Roos, C. F. (2012). Quantum simulations with trapped ions. *Nature Physics*, 8(4):277–284.

Bloch, I., Dalibard, J., and Zwerger, W. (2008). Many-body physics with ultracold gases. *Rev. Mod. Phys.*, 80:885–964.

Bohigas, O., Giannoni, M.-J., and Schmit, C. (1984). Characterization of chaotic quantum spectra and universality of level fluctuation laws. *Phys. Rev. Lett.*, 52(1):1.

Bohn, J. L., Rey, A. M., and Ye, J. (2017). Cold molecules: Progress in quantum engineering of chemistry and quantum matter. *Science*, 357(6355):1002–1010.

Borgonovi, F., Izrailev, F. M., Santos, L. F., and Zelevinsky, V. G. (2016). Quantum chaos and thermalization in isolated systems of interacting particles. *Phys. Rep.*, 626:1–58.

Bowler, R., Gaebler, J., Lin, Y., Tan, T. R., Hanneke, D., Jost, J. D., Home, J. P., Leibfried, D., and Wineland, D. J. (2012). Coherent Diabatic Ion Transport and Separation in a Multizone Trap Array. *Phys. Rev. Lett.*, 109(8):080502.

Boyers, E., Pandey, M., Campbell, D. K., Polkovnikov, A., Sels, D., and Sushkov, A. O. (2019). Floquet-engineered quantum state manipulation in a noisy qubit. *Physical Review A*, 100(1):012341.

Braun, P. and Haake, F. (2015). Self-averaging characteristics of spectral fluctuations. *J. Phys. A: Math. Theor.*, 48(13):135101.

Brenes, M., Goold, J., and Rigol, M. (2020a). Ballistic vs diffusive low-frequency scaling in the xxz and a locally perturbed xxz chain. *arXiv:2005.12309*.

Brenes, M., LeBlond, T., Goold, J., and Rigol, M. (2020b). Eigenstate thermalization in a locally perturbed integrable system. *arXiv:2004.04755*.

Brody, T. A., Flores, J., French, J. B., Mello, P., Pandey, A., and Wong, S. S. (1981). Random-matrix physics: spectrum and strength fluctuations. *Rev. Mod. Phys.*, 53(3):385.

Bukov, M., D'Alessio, L., and Polkovnikov, A. (2015). Universal high-frequency behavior of periodically driven systems: from dynamical stabilization to floquet engineering. *Advances in Physics*, 64(2):139–226.

Bukov, M., Sels, D., and Polkovnikov, A. (2019). The Geometric Speed Limit of Accessible Quantum State Preparation. *Phys. Rev. X*, 9:011034.

Caneva, T., Calarco, T., and Montangero, S. (2011). Chopped random-basis quantum optimization. *Physical Review A*, 84(2):022326.

Caux, J.-S. and Mossel, J. (2011). Remarks on the notion of quantum integrability. *J. Stat. Mech: Theory Exp.*, 2011(02):P02023.

Cencini, M., Cecconi, F., and Vulpiani, A. (2010). *Chaos: from simple models to complex systems*, volume 17. World Scientific.

Chandra, A. K., Das, A., and Chakrabarti, B. K. (2010). *Quantum quenching, annealing and computation*, volume 802. Springer Science & Business Media.

Chavda, N., Deota, H., and Kota, V. (2014). Poisson to goe transition in the distribution of the ratio of consecutive level spacings. *Phys. Lett. A*, 378(41):3012–3017.

Chen, X., Ruschhaupt, A., Schmidt, S., del Campo, A., Guéry-Odelin, D., and Muga, J. G. (2010). Fast Optimal Frictionless Atom Cooling in Harmonic Traps: Shortcut to Adiabaticity. *Phys. Rev. Lett.*, 104(6):063002.

Childress, L., Walsworth, R., and Lukin, M. (2014). Atom-like crystal defects: From quantum computers to biological sensors. *Physics Today*, 67(10):38–43.

Claassen, M., Jiang, H.-C., Moritz, B., and Devereaux, T. P. (2017). Dynamical time-reversal symmetry breaking and photo-induced chiral spin liquids in frustrated Mott insulators. *Nat. Comm.*, 8(1):1192.

Claeys, P. W., Pandey, M., Sels, D., and Polkovnikov, A. (2019). Floquet-Engineering Counterdiabatic Protocols in Quantum Many-Body Systems. *Physical Review Letters*, 123(9):090602.

Couvert, A., Kawalec, T., Reinaudi, G., and Guéry-Odelin, D. (2008). Optimal transport of ultracold atoms in the non-adiabatic regime. *Europhysics Letters*, 83(1):13001.

Crowley, P. J. and Chandran, A. (2019). Avalanche induced co-existing localised and thermal regions in disordered chains. *arXiv preprint arXiv:1910.10812*.

D'Alessio, L., Kafri, Y., Polkovnikov, A., and Rigol, M. (2016). From quantum chaos and eigenstate thermalization to statistical mechanics and thermodynamics. *Advances in Physics*, 65(3):239–362.

Danieli, C., Campbell, D., and Flach, S. (2017). Intermittent many-body dynamics at equilibrium. *Phys. Rev. E*, 95(6):060202.

Day, A. G., Bukov, M., Weinberg, P., Mehta, P., and Sels, D. (2019). Glassy phase of optimal quantum control. *Physical Review Letters*, 122(2):020601.

de Lange, G., Wang, Z. H., Ristè, D., Dobrovitski, V. V., and Hanson, R. (2010). Universal dynamical decoupling of a single solid-state spin from a spin bath. *Science*, 330(6000):60–3.

Deffner, S., Jarzynski, C., and del Campo, A. (2014). Classical and Quantum Shortcuts to Adiabaticity for Scale-Invariant Driving. *Phys. Rev. X*, 4(2):021013.

del Campo, A. (2013). Shortcuts to Adiabaticity by Counterdiabatic Driving. *Phys. Rev. Lett.*, 111(10):100502.

del Campo, A. and Kim, K. (2019). Focus on Shortcuts to Adiabaticity. *arXiv:1902.06283*.

del Campo, A., Rams, M. M., and Zurek, W. H. (2012). Assisted finite-rate adiabatic passage across a quantum critical point: exact solution for the quantum ising model. *Physical review letters*, 109(11):115703.

del Campo, A. and Sengupta, K. (2015). Controlling quantum critical dynamics of isolated systems. *Eur. Phys. J. Spec. Top.*, 224(1):189–203.

Demirplak, M. and Rice, S. A. (2003). Adiabatic population transfer with control fields. *The Journal of Physical Chemistry A*, 107(46):9937–9945.

Demirplak, M. and Rice, S. A. (2005). Assisted adiabatic passage revisited. *The Journal of Physical Chemistry B*, 109(14):6838–6844.

Demirplak, M. and Rice, S. A. (2008). On the consistency, extremal, and global properties of counterdiabatic fields. *J. Chem. Phys.*, 129(15):154111.

Deutsch, J. M. (1991). Quantum statistical mechanics in a closed system. *Phys. Rev. A*, 43(4):2046.

Deutsch, J. M. (2018). Eigenstate thermalization hypothesis. *Reports on Progress in Physics*, 81(8):082001.

Diao, P., Deng, S., Li, F., Yu, S., Chenu, A., del Campo, A., and Wu, H. (2018). Shortcuts to adiabaticity in Fermi gases. *New J. Phys.*, 20(10):105004.

Du, Y.-X., Liang, Z.-T., Li, Y.-C., Yue, X.-X., Lv, Q.-X., Huang, W., Chen, X., Yan, H., and Zhu, S.-L. (2016). Experimental realization of stimulated raman shortcut-to-adiabatic passage with cold atoms. *Nat. Commun.*, 7:12479.

Duncan, C. W. and del Campo, A. (2018). Shortcuts to Adiabaticity Assisted by Counterdiabatic Born-Oppenheimer Dynamics. *New J. Phys.*, 20(8):085003. arXiv: 1804.00434.

Dymarsky, A. and Liu, H. (2019). New characteristic of quantum many-body chaotic systems. *Physical Review E*, 99(1):010102.

D'Alessio, L. and Rigol, M. (2014). Long-time Behavior of Isolated Periodically Driven Interacting Lattice Systems. *Phys. Rev. X*, 4(4):041048.

Eckardt, A. (2017). Colloquium: Atomic quantum gases in periodically driven optical lattices. *Reviews of Modern Physics*, 89(1):011004.

Eisert, J., Friesdorf, M., and Gogolin, C. (2015). Quantum many-body systems out of equilibrium. *Nat. Phys.*, 11(2):124–130.

Farhi, E., Goldstone, J., and Gutmann, S. (2014). A quantum approximate optimization algorithm. Technical Report MIT-CTP/4610, Center for Theoretical Physics, Massachusetts Institute of Technology. `https://arxiv.org/abs/1411.4028`.

Farhi, E., Goldstone, J., Gutmann, S., and Sipser, M. (2000). Quantum computation by adiabatic evolution. *arXiv preprint quant-ph/0001106*.

Franchini, F. (2017). *An introduction to integrable techniques for one-dimensional quantum systems*, volume 940. Springer.

Funo, K., Zhang, J.-N., Chatou, C., Kim, K., Ueda, M., and del Campo, A. (2017). Universal Work Fluctuations During Shortcuts to Adiabaticity by Counterdiabatic Driving. *Phys. Rev. Lett.*, 118(10):100602.

Gallavotti, G. (2007). *The Fermi-Pasta-Ulam problem: a status report*, volume 728. Springer.

Gaudin, M. (2014). *The Bethe Wavefunction*. Cambridge University Press, Cambridge. Translated by Jean-Sébastien Caux.

Glaser, S. J., Schulte-Herbrüggen, T., Sieveking, M., Schedletzky, O., Nielsen, N. C., Sørensen, O. W., and Griesinger, C. (1998). Unitary control in quantum ensembles: Maximizing signal intensity in coherent spectroscopy. *Science*, 280(5362):421–424.

Goldman, N. and Dalibard, J. (2014). Periodically Driven Quantum Systems: Effective Hamiltonians and Engineered Gauge Fields. *Phys. Rev. X*, 4(3):031027.

Goldman, N., Dalibard, J., Aidelsburger, M., and Cooper, N. R. (2015). Periodically driven quantum matter: The case of resonant modulations. *Phys. Rev. A*, 91(3):033632.

Gómez, J., Molina, R., Relano, A., and Retamosa, J. (2002). Misleading signatures of quantum chaos. *Phys. Rev. E*, 66(3):036209.

Griffiths, D. J. and Schroeter, D. F. (2018). *Introduction to quantum mechanics*. Cambridge University Press.

Gritsev, V. and Polkovnikov, A. (2017). Integrable Floquet dynamics. *SciPost Phys.*, 2(3):021.

Gubin, A. and F. Santos, L. (2012). Quantum chaos: An introduction via chains of interacting spins 1/2. *Am. J. Phys*, 80(3):246–251.

Guéry-Odelin, D., Ruschhaupt, A., Kiely, A., Torrontegui, E., Martínez-Garaot, S., and Muga, J. G. (2019). Shortcuts to adiabaticity: Concepts, methods, and applications. *Reviews of Modern Physics*, 91(4).

Guhr, T., Müller-Groeling, A., and Weidenmüller, H. A. (1998). Random-matrix theories in quantum physics: common concepts. *Phys. Rep.*, 299(4-6):189–425.

Haake, F., Gnutzmann, S., and Kuś, M. (2013). *Quantum Signatures of Chaos*. Springer.

Hartmann, A. and Lechner, W. (2019). Rapid counter-diabatic sweeps in lattice gauge adiabatic quantum computing. *New Journal of Physics*, 21(4):043025.

Hastings, M. (2010). Quasi-adiabatic continuation for disordered systems: Applications to correlations, lieb-schultz-mattis, and hall conductance. *arXiv preprint arXiv:1001.5280*.

Hatomura, T. and Mori, T. (2018). Shortcuts to adiabatic classical spin dynamics mimicking quantum annealing. *Phys. Rev. E*, 98(3):032136.

Hegerfeldt, G. C. (2013). Driving at the quantum speed limit: Optimal control of a two-level system. *Phys. Rev. Lett.*, 111:260501.

Huang, P., Zhou, J., Fang, F., Kong, X., Xu, X., Ju, C., and Du, J. (2011). Landau-Zener-Stückelberg Interferometry of a Single Electronic Spin in a Noisy Environment. *Physical Review X*, 1(1):011003.

Ilievski, E., Medenjak, M., Prosen, T., and Zadnik, L. (2016). Quasilocal charges in integrable lattice systems. *J. Stat. Mech: Theory Exp.*, 2016(6):064008.

Jacques, V., Neumann, P., Beck, J., Markham, M., Twitchen, D., Meijer, J., Kaiser, F., Balasubramanian, G., Jelezko, F., and Wrachtrup, J. (2009). Dynamic polarization of single nuclear spins by optical pumping of nitrogen-vacancy color centers in diamond at room temperature. *Phys. Rev. Lett.*, 102:057403.

Jarzynski, C. (1995). Geometric Phases and Anholonomy for a Class of Chaotic Classical Systems. *Physical Review Letters*, 75(19):3430–3433.

Jarzynski, C. (2013). Generating shortcuts to adiabaticity in quantum and classical dynamics. *Physical Review A*, 88(4):040101.

Jones, J. A., Karlen, S. D., Fitzsimons, J., Ardavan, A., Benjamin, S. C., Briggs, G. A. D., and Morton, J. J. L. (2009). Magnetic field sensing beyond the standard quantum limit using 10-spin NOON states. *Science*, 324(5931):1166–8.

Judson, R. S. and Rabitz, H. (1992). Teaching lasers to control molecules. *Physical Review Letters*, 68(10):1500–1503.

Khemani, V., Vishwanath, A., and Huse, D. A. (2018). Operator Spreading and the Emergence of Dissipative Hydrodynamics under Unitary Evolution with Conservation Laws. *Phys. Rev. X*, 8(3):031057.

Kim, H. and Huse, D. A. (2013). Ballistic spreading of entanglement in a diffusive nonintegrable system. *Physical review letters*, 111(12):127205.

Kobayashi, S. and Nomizu, K. (1963). *Foundations of differential geometry*, volume 1 No. 2. New York, London.

Kölbl, J., Barfuss, A., Kasperczyk, M. S., Thiel, L., Clerk, A. A., Ribeiro, H., and Maletinsky, P. (2019). Initialization of single spin dressed states using shortcuts to adiabaticity. *Phys. Rev. Lett.*, 122:090502.

Kolmogorov, A. N. (1954). On conservation of conditionally periodic motions for a small change in Hamilton's function. *Dokl. Akad. Nauk SSSR*.

Kolodrubetz, M., Sels, D., Mehta, P., and Polkovnikov, A. (2017). Geometry and non-adiabatic response in quantum and classical systems. *Physics Reports*, 697:1–87.

Krinner, S., Stadler, D., Husmann, D., Brantut, J.-P., and Esslinger, T. (2014). Observation of quantized conductance in neutral matter. *Nature*, 517:64 EP –.

Kudler-Flam, J., Nie, L., and Ryu, S. (2020). Conformal field theory and the web of quantum chaos diagnostics. *J. High Energy Phys.*, 2020(1):175.

Kudo, K. and Deguchi, T. (2003). Unexpected non-wigner behavior in level-spacing distributions of next-nearest-neighbor coupled xxz spin chains. *Phys. Rev. B*, 68(5):052510.

Kuwahara, T., Mori, T., and Saito, K. (2016). Floquet–Magnus theory and generic transient dynamics in periodically driven many-body quantum systems. *Ann. Phys.*, 367:96–124.

Langen, T., Geiger, R., and Schmiedmayer, J. (2015). Ultracold atoms out of equilibrium. *Annu. Rev. Condens. Matter Phys.*, 6(1):201–217.

LeBlond, T., Mallayya, K., Vidmar, L., and Rigol, M. (2019). Entanglement and matrix elements of observables in interacting integrable systems. *Phys. Rev. E*, 100(6):062134.

Lewis-Swan, R. J., Safavi-Naini, A., Kaufman, A. M., and Rey, A. M. (2019). Dynamics of quantum information. *Nature Reviews Physics*, 1(10):627–634.

Maldacena, J., Shenker, S. H., and Stanford, D. (2016). A bound on chaos. *J. High Energ. Phys.*, 2016(8):106.

Martínez-Garaot, S., Torrontegui, E., Chen, X., and Muga, J. G. (2014). Shortcuts to adiabaticity in three-level systems using Lie transforms. *Phys. Rev. A*, 89(5):053408.

Marzlin, K.-P. and Sanders, B. C. (2004). Inconsistency in the application of the adiabatic theorem. *Physical review letters*, 93(16):160408.

Masuda, S. and Nakamura, K. (2009). Fast-forward of adiabatic dynamics in quantum mechanics. In *Proceedings of the Royal Society of London A: Mathematical, Physical and Engineering Sciences*, page rspa20090446. The Royal Society.

Mehta, M. L. (2004). *Random matrices*. Elsevier, 3 edition.

Mentink, J. H. (2017). Manipulating magnetism by ultrafast control of the exchange interaction. *J. Phys.: Condens. Matter*, 29(45):453001.

Modak, R. and Mukerjee, S. (2014). Finite size scaling in crossover among different random matrix ensembles in microscopic lattice models. *New J. Phys.*, 16(9):093016.

Modak, R., Mukerjee, S., and Ramaswamy, S. (2014). Universal power law in crossover from integrability to quantum chaos. *Physical Review B - Condensed Matter and Materials Physics*, 90(7):1–5.

Mondaini, R. and Rigol, M. (2017). Eigenstate thermalization in the two-dimensional transverse field ising model. ii. off-diagonal matrix elements of observables. *Phys. Rev. E*, 96:012157.

Mori, T., Kuwahara, T., and Saito, K. (2016). Rigorous Bound on Energy Absorption and Generic Relaxation in Periodically Driven Quantum Systems. *Phys. Rev. Lett.*, 116(12):120401.

Moser, J. K. (1962). On invariant curves of area-preserving mapping of an annulus. *Matematika*, 6(5):51–68.

Müller, S., Heusler, S., Braun, P., Haake, F., and Altland, A. (2004). Semiclassical Foundation of Universality in Quantum Chaos. *Phys. Rev. Lett.*, 93(1):014103.

Nahum, A., Vijay, S., and Haah, J. (2018). Operator Spreading in Random Unitary Circuits. *Phys. Rev. X*, 8(2):021014.

Nandkishore, R. and Huse, D. A. (2015). Many-body localization and thermalization in quantum statistical mechanics. *Annu. Rev. Condens. Matter Phys.*, 6(1):15–38.

Nielsen, M. A. and Chuang, I. L. (2000). *Quantum computation and quantum information*. Cambridge University Press, Cambridge.

Oganesyan, V. and Huse, D. A. (2007). Localization of interacting fermions at high temperature. *Phys. Rev. B*, 75(15):155111.

Okuyama, M. and Takahashi, K. (2016). From Classical Nonlinear Integrable Systems to Quantum Shortcuts to Adiabaticity. *Phys. Rev. Lett.*, 117(7):070401.

Orbach, R. (1958). Linear Antiferromagnetic Chain with Anisotropic Coupling. *Phys. Rev.*, 112(2):309–316.

Pace, S. D. and Campbell, D. K. (2019). Behavior and breakdown of higher-order fermi-pasta-ulam-tsingou recurrences. *Chaos*, 29(2):023132.

Page, D. N. (1987). Geometrical description of berry's phase. *Phys. Rev. A*, 36(7):3479.

Pandey, M., Claeys, P. W., Campbell, D. K., Polkovnikov, A., and Sels, D. (2020). Adiabatic eigenstate deformations as a sensitive probe for quantum chaos. *Physical Review X*, 10(4):041017.

Parker, D. E., Cao, X., Avdoshkin, A., Scaffidi, T., and Altman, E. (2019). A universal operator growth hypothesis. *Physics Review X*, 9(4):041017.

Patra, A. and Jarzynski, C. (2017). Shortcuts to adiabaticity using flow fields. *New J. Phys.*, 19(12):125009.

Petiziol, F., Dive, B., Carretta, S., Mannella, R., Mintert, F., and Wimberger, S. (2019). Accelerating adiabatic protocols for entangling two qubits in circuit qed. *Phys. Rev. A*, 99(4):042315.

Petiziol, F., Dive, B., Mintert, F., and Wimberger, S. (2018). Fast adiabatic evolution by oscillating initial Hamiltonians. *Phys. Rev. A*, 98(4):043436.

Pichler, H., Wang, S.-T., Zhou, L., Choi, S., and Lukin, M. D. (2018). Quantum optimization for maximum independent set using rydberg atom arrays. *arXiv preprint arXiv:1808.10816 [quant-ph]*.

Polkovnikov, A., Sengupta, K., Silva, A., and Vengalattore, M. (2010). Nonequilibrium dynamics of closed interacting quantum systems. *Reviews of Modern Physics*, 83(3):863–883.

Prange, R. (1997). The spectral form factor is not self-averaging. *Phys. Rev. Lett.*, 78(12):2280.

Provost, J. and Vallee, G. (1980). Riemannian structure on manifolds of quantum states. *Commun. Math. Phys.*, 76(3):289–301.

Rabson, D. A., Narozhny, B. N., and Millis, A. J. (2004). Crossover from Poisson to Wigner-Dyson level statistics in spin chains with integrability breaking. *Physical Review B - Condensed Matter and Materials Physics*, 69(5):1–8.

Rakovszky, T., Pollmann, F., and von Keyserlingk, C. (2018). Diffusive hydrodynamics of out-of-time-ordered correlators with charge conservation. *Phys. Rev. X*, 8(3):031058.

Rezek, Y., Salamon, P., Hoffmann, K. H., and Kosloff, R. (2009). The quantum refrigerator: The quest for absolute zero. *Europhysics Letters*, 85(3):30008.

Ribeiro, H., Baksic, A., and Clerk, A. A. (2017). Systematic Magnus-Based Approach for Suppressing Leakage and Nonadiabatic Errors in Quantum Dynamics. *Phys. Rev. X*, 7(1):011021.

Rigol, M., Dunjko, V., and Olshanii, M. (2008). Thermalization and its mechanism for generic isolated quantum systems. *Nature*, 452(7189):854–858.

Saberi, H., Opatrný, T., Mølmer, K., and del Campo, A. (2014). Adiabatic tracking of quantum many-body dynamics. *Phys. Rev. A*, 90(6):060301(R).

Sachdev, S. (2007). *Quantum phase transitions*. Wiley Online Library.

Salamon, P., Hoffmann, K. H., Rezek, Y., and Kosloff, R. (2009). Maximum work in minimum time from a conservative quantum system. *Physical Chemistry Chemical Physics*, 11(7):1027–1032.

Santoro, G. E. and Tosatti, E. (2006). Optimization using quantum mechanics: quantum annealing through adiabatic evolution. *Journal of Physics A: Mathematical and General*, 39(36):R393.

Santoro, G. E. and Tosatti, E. (2008). Optimization using quantum mechanics: quantum annealing through adiabatic evolution. *Journal of Physics A: Mathematical and Theoretical*, 41(20):209801.

Santos, L. F. (2004). Integrability of a disordered Heisenberg spin-1/2 chain. *Journal of Physics A: Mathematical and General*, 37(17):4723–4729.

Santos, L. F. and Rigol, M. (2010). Onset of quantum chaos in one-dimensional bosonic and fermionic systems and its relation to thermalization. *Physical Review E - Statistical, Nonlinear, and Soft Matter Physics*, 81(3):1–10.

Schäfer, F., Fukuhara, T., Sugawa, S., Takasu, Y., and Takahashi, Y. (2020). Tools for quantum simulation with ultracold atoms in optical lattices. *Nature Reviews Physics*, 2(8):411–425.

Schiulaz, M., Torres-Herrera, E. J., and Santos, L. F. (2019). Thouless and relaxation time scales in many-body quantum systems. *Physical Review B*, 99(17):174313.

Sels, D. (2018). Stochastic gradient ascent outperforms gamers in the Quantum Moves game. *Phys. Rev. A*, 97(4):040302(R).

Sels, D. and Polkovnikov, A. (2017). Minimizing irreversible losses in quantum systems by local counterdiabatic driving. *Proceedings of the National Academy of Sciences*, 114(20):E3909–E3916.

Serbyn, M., Papić, Z., and Abanin, D. A. (2015). Criterion for many-body localization-delocalization phase transition. *Phys. Rev. X*, 5(4):041047.

Shenker, S. H. and Stanford, D. (2014). Black holes and the butterfly effect. *J. High Energ. Phys.*, 2014(3):67.

Sierant, P., Maksymov, A., Kuś, M., and Zakrzewski, J. (2019). Fidelity susceptibility in gaussian random ensembles. *Phys. Rev. E*, 99:050102.

Song, X.-K., Ai, Q., Qiu, J., and Deng, F.-G. (2016). Physically feasible three-level transitionless quantum driving with multiple Schrödinger dynamics. *Phys. Rev. A*, 93(5):052324.

Sørensen, J. J. W. H., Pedersen, M. K., Munch, M., Haikka, P., Jensen, J. H., Planke, T., Andreasen, M. G., Gajdacz, M., Mølmer, K., Lieberoth, A., and Sherson, J. F. (2016). Exploring the quantum speed limit with computer games. *Nature*, 532(7598):210–213.

Srednicki, M. (1994). Chaos and quantum thermalization. *Phys. Rev. E*, 50(2):888.

Stöckmann, H.-J. (1999). *Quantum chaos: an introduction*. Cambridge University Press.

Šuntajs, J., Bonča, J., Prosen, T., and Vidmar, L. (2019). Quantum chaos challenges many-body localization. *arXiv preprint arXiv:1905.06345*.

Sutherland, B. (2004). *Beautiful Models: 70 Years of Exactly Solved Quantum Many-body Problems*. World Scientific.

Swingle, B. (2018). Unscrambling the physics of out-of-time-order correlators. *Nature Physics*, 14(10):988–990.

Takahashi, K. (2017). Shortcuts to adiabaticity for quantum annealing. *Physical Review A*, 95(1).

Taylor, J. M., Cappellaro, P., Childress, L., Jiang, L., Budker, D., Hemmer, P. R., Yacoby, A., Walsworth, R., and Lukin, M. D. (2008). High-sensitivity diamond magnetometer with nanoscale resolution. *Nature Physics*, 4(10):810–816.

Tong, D., Singh, K., Kwek, L. C., and Oh, C. H. (2005). Quantitative conditions do not guarantee the validity of the adiabatic approximation. *Physical review letters*, 95(11):110407.

Tong, D., Singh, K., Kwek, L. C., and Oh, C. H. (2007). Sufficiency criterion for the validity of the adiabatic approximation. *Physical review letters*, 98(15):150402.

Torres-Herrera, E. and Santos, L. F. (2014). Local quenches with global effects in interacting quantum systems. *Physical Review E*, 89(6):062110.

Torres-Herrera, E. J. and Santos, L. F. (2017). Dynamical manifestations of quantum chaos: correlation hole and bulge. *Philosophical Transactions of the Royal Society A: Mathematical, Physical and Engineering Sciences*, 375(2108):20160434.

Torrontegui, E., Ibánez, S., Martínez-Garaot, S., Modugno, M., del Campo, A., Guéry-Odelin, D., Ruschhaupt, A., Chen, X., and Muga, J. G. (2013). Shortcuts to adiabaticity. In *Advances in atomic, molecular, and optical physics*, volume 62, pages 117–169. Elsevier.

Torrontegui, E., Martínez-Garaot, S., Ruschhaupt, A., and Muga, J. G. (2012). Shortcuts to adiabaticity: Fast-forward approach. *Phys. Rev. A*, 86(1):013601.

Vepsäläinen, A., Danilin, S., and Paraoanu, G. S. (2018). Optimal superadiabatic population transfer and gates by dynamical phase corrections. *Quantum Sci. Technol.*, 3(2):024006.

Vepsäläinen, A., Danilin, S., and Paraoanu, G. S. (2019). Superadiabatic population transfer in a three-level superconducting circuit. *Sci. Adv.*, 5(2):eaau5999.

Villazon, T., Claeys, P. W., Pandey, M., Polkovnikov, A., and Chandran, A. (2020). Persistent dark states in anisotropic central spin models. *Scientific reports*, 10(1):1–16.

Villazon, T., Polkovnikov, A., and Chandran, A. (2019). Swift heat transfer by fast-forward driving in open quantum systems. *Physical Review A*, 100(1):012126.

Vinjanampathy, S. and Anders, J. (2016). Quantum thermodynamics. *Contemp. Phys.*, 57(4):545–579.

Viola, L., Knill, E., and Lloyd, S. (1999). Dynamical Decoupling of Open Quantum Systems. *Physical Review Letters*, 82(12):2417–2421.

Von Keyserlingk, C., Rakovszky, T., Pollmann, F., and Sondhi, S. L. (2018). Operator hydrodynamics, otocs, and entanglement growth in systems without conservation laws. *Phys. Rev. X*, 8(2):021013.

Walther, A., Ziesel, F., Ruster, T., Dawkins, S. T., Ott, K., Hettrich, M., Singer, K., Schmidt-Kaler, F., and Poschinger, U. (2012). Controlling Fast Transport of Cold Trapped Ions. *Phys. Rev. Lett.*, 109(8):080501.

Weinberg, P. and Bukov, M. (2017). Quspin: a python package for dynamics and exact diagonalisation of quantum many body systems part i: spin chains. *SciPost Phys.*, 2(003):003.

Weinberg, P. and Bukov, M. (2019). Quspin: a python package for dynamics and exact diagonalisation of quantum many body systems. part ii: bosons, fermions and higher spins. *SciPost Phys.*, 7:020.

Wigner, E. P. (1958). On the distribution of the roots of certain symmetric matrices. *Ann. Math.*, 67(2):325–327.

Wigner, E. P. (1993). Characteristic vectors of bordered matrices with infinite dimensions ii. In *The Collected Works of Eugene Paul Wigner*, pages 541–545. Springer.

Wilf, H. S. (2005). *generatingfunctionology*. CRC press.

Wurtz, J., Claeys, P. W., and Polkovnikov, A. (2020). Variational Schrieffer-Wolff transformations for quantum many-body dynamics. *Physical Review B*, 101(1):014302.

Wurtz, J. and Polkovnikov, A. (2020). Emergent conservation laws and nonthermal states in the mixed-field Ising model. *Physical Review B*, 101(19):195138.

Yang, C. N. and Yang, C. P. (1966). One-Dimensional Chain of Anisotropic Spin-Spin Interactions. I. Proof of Bethe's Hypothesis for Ground State in a Finite System. *Phys. Rev.*, 150(1):321–327.

Yuzbashyan, E. A. and Shastry, B. S. (2013). Quantum integrability in systems with finite number of levels. *J. Stat. Phys.*, 150(4):704–721.

Yuzbashyan, E. A., Shastry, B. S., and Scaramazza, J. A. (2016). Rotationally invariant ensembles of integrable matrices. *Phys. Rev. E*, 93(5):052114.

Zhang, J., Shim, J. H., Niemeyer, I., Taniguchi, T., Teraji, T., Abe, H., Onoda, S., Yamamoto, T., Ohshima, T., Isoya, J., and Suter, D. (2013). Experimental Implementation of Assisted Quantum Adiabatic Passage in a Single Spin. *Physical Review Letters*, 110(24):240501.

Zheng, Y., Campbell, S., De Chiara, G., and Poletti, D. (2016). Cost of counterdiabatic driving and work output. *Phys. Rev. A*, 94(4):042132.

Zhou, B. B., Baksic, A., Ribeiro, H., Yale, C. G., Heremans, F. J., Jerger, P. C., Auer, A., Burkard, G., Clerk, A. A., and Awschalom, D. D. (2017). Accelerated quantum control using superadiabatic dynamics in a solid-state lambda system. *Nat. Phys.*, 13(4):330.

Zhou, T. and Luitz, D. J. (2017). Operator entanglement entropy of the time evolution operator in chaotic systems. *Phys. Rev. B*, 95(9):094206.

Zwick, A., Álvarez, G. A., Bensky, G., and Kurizki, G. (2014). Optimized dynamical control of state transfer through noisy spin chains. *New J. Phys.*, 16(6):065021.

CURRICULUM VITAE